TECH LIBRARY KAFB, NM
0099691

NASA CONTRACTOR REPORT



N.A.S.A. C.R.

NASA CR-265

THE STABILITY OF SHALLOW SPHERICAL SHELLS UNDER CONCENTRATED LOAD

by F. A. Penning and G. A. Thurston

RECEIVED
AUG 1965

Prepared under Contract No. NASw-912 *by*

MARTIN-MARIETTA CORPORATION
Denver, Colo.

for

NATIONAL AERONAUTICS AND SPACE ADMINISTRATION • WASHINGTON, D. C. • JULY 1965

NASA CR-265
TECH LIBRARY KAFB, NM
0099691

THE STABILITY OF SHALLOW SPHERICAL SHELLS UNDER CONCENTRATED LOAD

By F. A. Penning and G. A. Thurston

Distribution of this report is provided in the interest of information exchange. Responsibility for the contents resides in the author or organization that prepared it.

Prepared under Contract No. NASw-912 by
MARTIN-MARIETTA CORPORATION
Denver, Colo.

for

NATIONAL AERONAUTICS AND SPACE ADMINISTRATION

For sale by the Clearinghouse for Federal Scientific and Technical Information
Springfield, Virginia 22151 – Price $3.00

CONTENTS

	Page
Contents	iii
Acknowledgement	vii
Summary	viii
Notation - Symmetric Analysis	x
I. Introduction	1
II. Theory	2
A. Reissner's Equations	3
B. Newton's Method	4
C. Buckling Criterion	6
D. Boundary Conditions	7
III. Experiment	8
A. Shell Fabrication	9
B. Geometry Determination	9
C. Buckling Tests	10
IV. Results	13
A. Theoretical Results	13
B. Experimental Results	16
V. Concluding Remarks	19
VI. References	21
Appendix -- Asymmetric Buckling Theory	24

Table

1	Shell Properties	47
2	Experimental Upper and Lower Critical Buckling Loads and Deflections	48

Figure

1	Notations	49
2	Procedure for Forming Shells	50
3	Schematic of Geometry-Measuring Device	51
4	Schematic of Tester, Loading Device, and Deflection Measuring Device	52
5	Interior of Tester	53
6	Deflection Measuring Device	54
7	Comparison of Theory and Experiment for Load-Deflection for Typical Tests, $\lambda = 5$	55
8	Comparison of Theory and Experiment for Load-Deflection for Typical Tests, $\lambda = 8.2$	56
9	Comparison of Theory and Experiment for Load-Deflection for Typical Tests, $\lambda \tilde{=} 8.2$	57
10	Comparison of Theory and Experiment for Load-Deflection for Typical Tests, $\lambda = 16.1$	58
11	Average Stress Resultant Under Load Area Changes Sign at Transition Load	59
12	Effect of Load Area on Maximum Bending Moment for $\lambda = 8$	60
13	Theory and Experiment Exhibit Dimpled Deflection Mode Shape for a Typical Shell	61
14	Theory and Experiment Exhibit Dimpled Deflection Mode Shape for a Typical Shell . . .	62

15	Determinant from Numerical Solution Reaches Minimum at Transition Load	63
16	Load at Which Surface Stress Reaches Yield Stress	64
17	Effect of Load Area on Yield Stress	65
18	Computed Mid-Surface Stress Resultants at a Load that Provided Asymmetric Buckling in Experimental Shell	66
19	Meridional Surface Strains Compared to Experiment	67
20	Circumferential Surface Strains Compared to Experiment	68
21	Experimental Load-Center Deflection, Four Load Areas, $\lambda \cong 4.9$, a = 20.0 in	69
22	Experimental Load-Center Deflection, Four Load Areas, $\lambda \cong 5$, $a \cong 30.0$ in.	70
23	Experimental Load-Center Deflection, Four Load Areas, $\lambda \cong 8.2$, a = 20.0 in.	71
24	Experimental Deflections on a Radial Line, $\lambda \cong 8.2$, a = 20.0 in.	72
25	Experimental Load-Center Deflection, Four Load Areas, $\lambda \cong 8$, a = 31.0 in.	73
26	Experimental Deflections on a Radial Line, $\lambda \cong 8$, a = 31.0 in.	74
27	Experimental Load-Center Deflection Curves for Four Shells, λ = 11.6 to 20.0	76 and 77
28	Experimental Load-Center Deflection Four Load Areas, $\lambda \cong 12$, a = 20.0 in.	78
29	Experimental Nonaxisymmetric Deflection, λ = 12.3, a = 20.0 in.	79

30	Experimental Load-Center Deflection, Four Load Areas, λ = 11.6, a = 31.0 in.	80
31	Experimental Nonaxisymmetric Deflections, λ = 11.6, a = 31.0 in.	81
32	Experimental Load-Center Deflection, Four Load Areas, λ = 16.1, a = 20.0 in.	82
33	Experimental Nonaxisymmetric Deflections, λ = 16.1, a = 20.0 in., Part 1	83
34	Experimental Nonaxisymmetric Deflections, λ = 16.0, a = 20.0 in., Part 2	84
35	Experimental Load-Center Deflection, Four Load Areas, λ = 15.6, a = 31.0 in.	85
36	Experimental Nonaxisymmetric Deflections, λ = 15.6, a = 31.0 in.	86
37	Experimental Load-Center Deflection, Four Load Areas, λ = 20.0, a = 20.0 in.	87
38	Experimental Load-Center Deflection, Four Load Areas, λ = 21.4, a = 31.0 in.	88
39	Shell B-36 with Three-Lobed Deformation . . .	89
40	Shell B-36 with Five-Lobed Deformation	90

ACKNOWLEDGMENT

The authors wish to acknowledge the assistance of M. A. Freeland and A. A. Holston in performing the computations, and the assistance of M. A. Freeland in conducting the tests. The numerical solution of Reissner's equations was programed by H. Rowan and C. Brauch.

SUMMARY

An experimental and theoretical study was conducted on shallow spherical caps under concentrated load. Aluminum specimens were clamped on the outer edge and tested using load tips with different cross sectional areas. Results from a numerical solution of Reissner's equations gave good agreement with experimental measurements for axisymmetric deflections. The experimental data revealed nonaxisymmetric deflections, upper and lower critical buckling loads, prebuckled and postbuckled deflections, and the existence of several sets of critical loads. A numerical solution to calculate bifurcation loads where asymmetric modes intersect the axisymmetric equilibrium positions failed to predict asymmetric buckling for this problem.

NOTATION - SYMMETRIC ANALYSIS

a	Radius of curvature of spherical shell (in.)
b	Horizontal radius of cap (in.)
B	Dependent variable
$C = Eh$	Extensional stiffness term (lb/in.)
$D = Eh^3/12\left(1 - \nu^2\right)$	Flexural rigidity (lb-in.)
E	Young's modulus (psi)
H	Radial stress resultant (lb/in.)
h	Shell thickness (in.)
L	Rise of spherical cap (in.)
M_x, M_θ	Moment stress resultant (in.-lb/in.)
N_x, N_θ	Stress resultants parallel to the mid-surface (lb/in.)
P	Applied axial load in addition to hydrostatic compression (lb)
$P^* = Pa/Eh^3$	Nondimensional load
q	External pressure (psi)
Q	Transverse shear stress resultant (lb/in.)
r	Horizontal radius of deformed shell mid-surface (in.)
r_o	Horizontal radius of undeformed shell mid-surface (in.)
r_p	Radius of load area (in.)
u, w	Radial and axial components of midsurface displacements (in.)
V	Axial stress resultant (lb/in.)

w_o	Axial deflection, apex of cap (in.)
x	Independent variable in Reissner's equations
z_o	Axial distance to point on midsurface (in.)
α_o	See Eq [5]
β	Rotation of shell tangent due to deflection
Δ	Determinant of linear algebraic equations
$\lambda = 2\left[3\left(1 - \nu^2\right)\right]^{\frac{1}{4}}\left(\frac{L}{h}\right)^{\frac{1}{2}}$	Geometrical parameter for spherical caps
ν	Poisson's ratio
σ_y	Yield stress (psi)
φ, φ_o	Angles from shell centerline to normal of deflected and of undeflected shell, respectively

I. INTRODUCTION

This study examined the effect of load area on the behavior of clamped shallow spherical caps under concentrated load. Both analytical and experimental results are reported.

The clamped cap under concentrated load has not received the attention in the literature that has been devoted to the cap under external pressure. Evan-Iwanowski[1] tested clamped caps made of plastic and reported that no snap-through buckling occurred for any of his specimens. He did note a transition from axisymmetric to asymmetric deflection shapes with increasing load. No precise numerical results appear in the literature for the finite deflection equations for the clamped boundary condition.

A slight discrepancy appears in the literature between theory and experiment for caps with no horizontal edge restraint. Ashwell[2] observed that "A shell with an increasing point load acting toward its centre of curvature is found by experiment to form a circular dimple, or region of reversed curvature, which spreads concentrically from the load." Ashwell devised an approximate solution for the nonlinear problem by using two sets of linear equations, one in the dimple area and one for the outer region of the shell. Ashwell obtained some experimental results that gave fair agreement with his approximate solution. Evan-Iwanowski[1,3, and 4] also reported experimental results for buckling loads and load-deflection curves similar to Ashwell's solution.

Archer[5] solved the finite deflection equations directly, using a numerical solution. His computed buckling loads fell below those calculated and measured by Ashwell and those obtained earlier from approximate solutions by Biezeno[6] and by Chien.[7]

The present study was initiated to study the effect of load area on the deformation of the clamped cap and to study the transition from axisymmetric to asymmetric deflection shapes.

Aluminum specimens were used in the study. These were manufactured by an explosive-forming process. By chem-milling the specimens to the desired thickness, thinner shells were employed in this study than in previous investigations.

II. THEORY

The theoretical portion of the study is based on two different sets of equations. The first set is Reissner's[8] finite deflection equations for shells of revolution under axisymmetric loads. These reduce to a fourth-order system of nonlinear ordinary differential equations that are solved numerically by use of a digital computer solution.

The solution of Reissner's equations completely determines axisymmetric equilibrium states. Deflections, stress resultants, and stresses in the shell are printed out by the computer program.

Critical loads in this theory are defined in the classical manner for static buckling. At buckling, at least two solutions of the differential equations exist for the same loading, and these solutions define equilibrium positions that are infinitesimally near each other. Since the nonlinear equations are solved directly, the distinct solutions near a buckling load can be obtained individually. This allows computing energy levels, postbuckled solutions, and solutions at loads above the first buckling load. Enough information is available to establish whether a bifurcation or a snap-through type of instability exists at the buckling load and whether the postbuckled solutions are stable.

The second set of equations used in the study is based on the nonlinear strain-displacement relations listed by Sanders.[9] These general expressions include asymmetric deformations as well as axisymmetric terms similar to those in Reissner's equations. The general strain expressions lead to an eighth-order set of nonlinear partial differential equations whose solution would be long and expensive. The approach adopted here is not to solve the general equations, but to seek loads where bifurcation occurs and asymmetric deflection modes exist infinitesimally near the axisymmetric equilibrium state. The axisymmetric solutions are obtained from finite deflection theory, but the bifurcation points are determined from linearized equations. The mode shapes associated with the bifurcation loads can be computed, but the amplitude is undetermined and there is no way to tell if the asymmetric solutions are stable.

The linearized theory has been used recently by several authors[10,11, and 12] for the special cases of spherical caps under pressure and cylinders under axial compression and hydrostatic

pressure. The numerical solution in the present study was derived for general shells of revolution. Since the solution has not appeared before in the open literature, the equations and method of solution are presented in detail in the Appendix.

The computer program for Reissner's equations has been described elsewhere[13,14, and 15] and will be outlined here.

A. REISSNER'S EQUATIONS

Although the experimental program was confined to shallow shells, the theoretical solution is applicable to general shells of revolution. The only restrictive assumption in the theory, in addition to the usual Love-Kirchhoff assumptions, is that the strains are elastic and small compared to unity.

The theory reduces to two nonlinear simultaneous differential equations that must be solved for the two unknowns φ and H. They are written as

$$\left\{\left[\frac{rD\left(\varphi_o' - \varphi'\right)}{\alpha_o} - \nu rD\,\frac{\left(\sin\varphi - \sin\varphi_o\right)}{r_o}\right]' - \alpha_o D\cos\varphi\left[\frac{\nu\left(\varphi_o' - \varphi'\right)}{\alpha_o} - \frac{\left(\sin\varphi - \sin\varphi_o\right)}{r_o}\right] + r_o\alpha_o H\sin\varphi = r_o\alpha_o V\cos\varphi;\right\} \quad [1]$$

$$\left\{\frac{r_o}{C}\left[\left(\frac{rH}{\alpha_o}\right)' - r_o q\sin\varphi - \nu(H\cos\varphi + V\sin\varphi)\right]\right\}' - \frac{\alpha_o\cos\varphi}{C}\left\{H\cos\varphi + V\sin\varphi - \nu\left[\left(\frac{rH}{\alpha_o}\right)' - r_o q\sin\varphi\right]\right\} = \alpha_o(\cos\varphi - \cos\varphi_o). \quad [2]$$

where primes denote differentiation with respect to the independent variable x. Figure 1 illustrates the notation.

Stress resultants and deflections in terms of φ and H are:

$$V = -\frac{r_o q}{2} - \frac{P}{2\pi r_o}; \qquad [3a]$$

$$N_x = H \cos \varphi + V \sin \varphi; \qquad [3b]$$

$$Q = -H \sin \varphi + V \cos \varphi; \qquad [3c]$$

$$N_\theta = \frac{r_o H'}{\alpha_o} + H \cos \varphi - r_o q \sin \varphi; \qquad [3d]$$

$$M_x = D\left[\frac{\varphi_o' - \varphi'}{\alpha_o} + \nu \frac{(\sin \varphi_o - \sin \varphi)}{r_o}\right]; \qquad [3e]$$

$$M_\theta = D\left[\nu \frac{(\varphi_o' - \varphi')}{\alpha_o} + \frac{(\sin \varphi_o - \sin \varphi)}{r_o}\right]. \qquad [3f]$$

$$u = \frac{r_o}{C}\left(N_\theta - \nu N_x\right); \qquad [4a]$$

$$w = \int \alpha_o \left[\left(\sin \varphi - \sin \varphi_o\right) + \frac{1}{C}\left(N_x - \nu N_\theta\right) \sin \varphi\right] dx. \qquad [4b]$$

The middle surface of the undeformed shell is defined by the parametric equations $r_o = r_o(x)$, $z_o = z_o(x)$. The following relations hold for the undeformed shell:

$$\alpha_o^2 = \left(r_o'\right)^2 + \left(z_o'\right)^2, \quad r_o' = \alpha_o \cos \varphi_o, \quad z_o' = \alpha_o \sin \varphi_o. \qquad [5]$$

A similar set of equations without the zero subscript applies for the deformed shell.

B. NEWTON'S METHOD

The nonlinear differential equations are solved by approximating them by a sequence of linear "variational" equations. The linear equations are solved numerically.

The linearization is performed by expanding nonlinear terms in the differential equations in a Taylor's series and retaining only linear terms. Any function $F(y, y', x)$ appearing in the equations where y is a dependent variable is approximated by

$$F\left(y_m + \delta y_m,\ y_m' + \delta y_m',\ x\right) = F\left(y_m,\ y_m',\ x\right) + F_y\left(y_m,\ y_m',\ x\right)\delta y_m + \\ + F_{y'}\left(y_m,\ y_m',\ x\right)\delta y_m', \qquad [6]$$

The subscripts of F denote partial derivatives and y_m is the mth approximation for the solution y. The variable δy becomes the dependent variable in the linearized differential equation and the next approximation for y is

$$y_{m+1} = y_m + \delta y_m \qquad [7]$$

This linearization procedure is an extension of Newton's method for finding roots of polynomials. Bellman, Juncosa, and Kalaba[16] credit Chaplygin[17] with first applying Newton's method to the integration of nonlinear differential equations in 1905. This method has largely been ignored in the United States, in spite of its generality. The lack of interest in applying Newton's method to nonlinear differential equations may be due to the fact that the sequence of linear differential equations to be solved contains variable coefficients. The difficulty in using Newton's method has been partially removed since digital computers have become available for calculating numerical solutions.

Reissner's equations have a singular point at the apex $r_o = 0$. A new variable B is introduced in the computer solution to avoid division by zero and to improve numerical accuracy.

$$B = \frac{\beta}{r_o} = \frac{\varphi_o - \varphi}{r_o}. \qquad [8]$$

In applying Newton's method to Reissner's equations, nonlinear terms appearing in the equations are expanded in terms of B and H. For example, where cos φ appears in the nonlinear equations, it is replaced by

$$\cos\varphi = \cos\varphi_m + \left(\sin\varphi_m\right) r_o\, \delta\, B_m \qquad [9]$$

where $\varphi_m = \varphi_o - \beta_m = \varphi_o - r_o B_m$. Terms such as H cos φ are expanded as

$$H\cos\varphi = H_m \cos\varphi_m + \delta\, H_m \cos\varphi_m + r_o\, H_m \left(\sin\varphi_m\right) \delta\, B_m. \qquad [10]$$

After solving the resulting linear differential equations for the corrections δH_m and δB_m, the next approximation for the solution is calculated from:

$$H_{m+1} = H_m + \delta H_m; \qquad [11a]$$

$$B_{m+1} = B_m + \delta B_m; \qquad [11b]$$

$$\beta_{m+1} = r_o B_{m+1}; \qquad [11c]$$

and the process is repeated until the corrections become small.

The linear variational differential equations for δH_m and δB_m are not derived explicitly here, because the nonlinear differential Eq [1] and [2] were integrated by parts twice to obtain equivalent nonlinear integral equations. The linearization was actually performed on the integral equations.

The solution of the linear integral equations is obtained numerically by a subroutine written to solve linear systems of integral equations by replacing the integrals by mechanical quadrature formulas. This reduces the integral equations to a set of algebraic equations. The subroutine is described in the Appendix in connection with the computer program for bifurcation buckling.

C. BUCKLING CRITERION

If the error in the current solution (B_m, H_m) is small, the correction $(\delta B_m, \delta H_m)$ is normally small and the solution converges. However, the error can be small while the computed correction is large. This occurs when the determinant Δ of the algebraic equations is near zero. The instability in the numerical solution at $\Delta = E_1 = E_2 = 0$ serves to define a point of neutral equilibrium since a non-zero solution for δB and δH in this case implies the existence of another equilibrium position in the neighborhood of the position defined by the given solution (B, H).

D. BOUNDARY CONDITIONS

Only one difficulty appeared in trying to apply Reissner's equations to the experimental shells. The proper boundary conditions at the edge of the finite load area are not known. The axial shear resultant V is statically determinant, but the two boundary conditions for Reissner's equations are continuity equations that require matching the rotational and radial displacements of the unloaded portion of the shell at the juncture with the small loaded area of the cap near the apex. The total load applied through the load tip can be measured but the distribution of pressure over the load area is not known and also varies in a nonlinear fashion with the deflection of the shell.

The boundary conditions at the apex of the shell can be determined from symmetry. The device employed in the computations was to use the boundary conditions at the apex of the shell and apply them at the edge of the load area a short distance away. For the small loading tips, the error in this is negligible. For the larger tips, this boundary condition introduces some discrepancy between the experimental deflections measured at the apex of the shell and the computed deflections that actually are calculated at the edge of the load area.

From the axial symmetry of the shell and the loading, it can be seen that the rotation β is an odd function of the radius r_o and the horizontal stress resultant H is even. Therefore, at the apex,

$$H' = 0 \qquad \text{at } r_o = 0,$$

$$B' = \left(\frac{\beta}{r_o}\right)' = 0 \qquad \text{at } r_o = 0.$$

The above boundary conditions were used in the computations at $r_o = r_p$.

At the clamped edge

$$\beta = 0, \qquad r_o = b,$$

$$u = 0, \qquad r_o = b.$$

III. EXPERIMENT

Shallow spherical shells with clamped boundaries and made of aluminum were loaded at the apex. Half of the shells were made with a 20-in. spherical radius and the other half with a 31-in. spherical radius. Shell thicknesses were controlled to provide nearly the same five values of λ for each of the spherical radii. For the five values of λ and for both of the spherical radii, concentrated loads were applied through four different size loading tips. A summary of the several parameters follows:

Material	6061 - T6 Aluminum
Spherical Radius	20 and 31 in.
Thickness Range	0.0066 to 0.1090 in. for 20-in. spherical radius 0.0037 to 0.0690 in. for 31-in. spherical radius
Base Diameter	8-in.
Load Tip Diameter	1/8, 1/4, 1/2, and 1-in.
Nominal Geometry, $\lambda \cong$	5, 8, 12, 16, and 20
Radius to Thickness Ratio	180 minimum, 8400 maximum
Total Number of Tests	40

The experimental part of the program required three separate and distinct areas of effort. These were making the shells, determining the finished shell geometry and thickness, and observing and measuring shell response during testing. Shells were formed explosively from aluminum sheet stock and reduced in thickness by chem-milling. Geometry plots along radial lines were made by using linear displacement transducers and were recorded on an X-Y plotter. Thickness was measured with a micrometer. Data taken during the tests provided a record of force-displacement for the several critical buckling loads and for plastic behavior. For the higher values of λ where shells remained elastic, the same shell was tested with more than one load tip. Where shells deformed plastically, a different shell was used for each load area.

A. SHELL FABRICATION

Aluminum shells were fabricated by explosive-forming 6061 aluminum into a female fiberglas epoxy laminated die. The material was received in sheet form, cut into squares, and into circular blanks of 10¼-in. diameter. While in the O-temper, explosive-forming set the soft material into the die cavity (Fig. 2). The formed shell was brought to solution heat treat temperature for 15 minutes and water quenched. Immediately after quenching the shells were kept cold to retain the T4 condition, until they were resized explosively into the same die cavity.

After resizing, the shells were artifically aged to the T6 temper by precipitation heat treating for several hours and then chem-milled to the required thickness. Chem-milling rate was about 0.00075 in. of surface removal per minute (with both sides of the shell exposed to the chem-mill bath, total removal was about 0.0015 in. per minute). Reasonably close control in thickness was accomplished by establishing the chem-milling rate and determining the immersion time. It was necessary to rotate the shells while in the bath to produce uniform removal over the entire surface.

B. GEOMETRY DETERMINATION

Shell cross sections were measured along radial lines starting at the apex and at 60-deg intervals. Two linear displacement transducers were mounted to measure z_o at r_o (Fig. 1). Transducers were kept fixed in space and the shell was translated while being held in contoured steel clamping rings. The schematic shown in Fig. 3 identifies all the instrumentation used in measuring and recording shell geometry.

The system was checked before each survey by measuring an accurately machined wedge and observing the resulting line for linearity, slope, and length. Calibrations in the radial direction were accurate to $\pm$0.002 in. over a 10-in. pen travel and corresponded to a half chord length of 4 in. Calibrations in the z-direction were accurate to $\pm$0.0005 in. over a 15-in. carriage travel, corresponding to ½ in. of mid-chord offset distance. These scales resulted in magnifying the actual radial distance by 2½ times and the z-distance by 30 times.

Surveys were spaced ¼-in. apart, thus providing a quick visual check for symmetry between the lines. Deviations from the nominal geometry were found by direct comparison with a master curve drawn for the appropriate spherical radius.

Thicknesses were measured, using a deep-throat micrometer with ball ends, and recorded to the nearest 0.0001 in. The same six radial lines used for geometry cross sections were measured at 1-in. intervals for a radial distance of 4 in. This gave a total of 25 measured points on each shell.

C. BUCKLING TESTS

Loading and measuring shell response was accomplished by integrating a loading device and a deflection measuring device into the basic tester. Clamped boundaries of appropriate spherical radius were provided by contoured steel rings having an 8-in. inside diameter and 9½-in. outside diameter giving a 3/4-in. clamping annulus. A schematic of the assembly is shown in Fig. 4.

All shells were loaded by dead weights acting through a lever system supported on knife edges. The loading beam inside the tester supported one of the four load tips. A load tip (1/4-in. dia), the loading beam, and a lower clamping ring are shown in Fig. 5.

Hollow steel cylinders with 0.05-in. walls were used as the loading tips, except for the 1/8-in. diameter tip that was solid steel. This type of load tip was selected because of the large departure the shells made from a flat area in the vicinity of the load tip and because of the great range in maximum load, several hundred pounds to several tenths of a pound. The only consistent contact area under these conditions was felt to be the hollowed steel tips. Ordinarily the loading system was damped with the dash pot shown in Fig. 4, however, for the larger loads, using a 10 to 1 load magnification, it was necessary to modify the system by using a load pan without damping. Overall accuracy of the loading system, using weights accurate to $\pm$0.00001 lb, was within 0.001 lb up to 10 lb total load and within 0.5% for all higher ranges. As the loading beam followed the deforming shell, the load arm was kept horizontal by raising the knife edge with the vertical adjustment shown in Fig. 4.

Measuring shell response was done with the deflection measuring device that measured in a cylindrical coordinate system. Figure 6 is a detail picture of the device, showing the dial gages mounted on a holder that is free to move on a radial line and able to rotate to any position. Angular position was measured by the indexed top of the tester, divided every 10 deg. The signal light on this device was used to determine when the shell had been contacted. Initially, the scheme for measuring to the shell surface was accomplished by completing an electrical circuit with a a needle coming in contact with the shell. It was found that the force required to overcome electrical contact resistance was sufficiently great that the very thin shells were noticeably deformed before the light would signal. An improvement over this system was a break-circuit device whereby a switch was opened when the shell was contacted and always with the same force, which measured less than 0.05 grams. A detail of the working mechanism of this switch is shown in Fig. 4. Repeatability of measurements in the vertical z-direction was observed to be ± 0.0002 in.

The shell was placed in the tester, observing the same angular orientation established during the explosive forming process and maintained during all operations. Preselected radial distances were chosen as those points at which all deflection measurements were made. With no load on the shell, a vertical reference dimension was established at the shell apex and vertical distances from a horizontal plane were measured along the zero-degree line at the preselected radial points. During load, vertical distance measurements taken at these points measured the vertical deflection. In addition, deflection measurements were made along a circle at a fixed radial distance from the apex. Generally, these measurements were taken at 30-deg intervals and provided sufficient information to identify the number of waves in nonaxisymmetric deflections and to determine the uniformity of the wave lengths. Where shells deformed plastically, the amount of permanent deformation at the apex was noted after the load had been removed.

This loading scheme made buckling of the shells very apparent. The two stable configurations for the shell were made obvious by the action of the loading arm shown in Fig. 4. As the upper critical buckling load was reached by increasing loads, the loading arm dropped noticeably. When decreasing the load, the lower critical buckling load was apparent when the loading arm moved upward an appreciable amount. By maintaining a constant load on the shell between the upper and lower critical loads, the two branches one prebuckled, the other postbuckled, could be determined merely by snapping the shell off of one branch onto the other. It was necessary, before making deflection measurements, to maintain a level loading arm for accurate application of load. Most of the buckles occurred with audible snaps.

Shells that deformed plastically were resurveyed at the end of testing to note the amount and kind of permanent deformation left in the shell without load but still in the clamping rings. In the cases where shells retained a permanent dimple each new test required a new shell. Shells that remained elastic were re-tested by using the same shell with another load tip.

Comprehensive definition of shell behavior is virtually impossible when using point by point determination of behavior and when using discrete values of load. As much information as possible, consistent with conducting forty separate tests was obtained from the specimens.

IV. RESULTS

Theoretical calculations did not reveal buckling loads for the clamped spherical cap under concentrated load. The experimental investigation, however, defined upper and lower critical buckling loads, prebuckled and postbuckled deflections, measured nonaxisymmetric deflections, and showed the effect of load area on buckling behavior. For small values of λ shells did not buckle but exhibited plastic deformation.

A. THEORETICAL RESULTS

The solution of Reissner's equations for the clamped cap did not determine any buckling loads, but did show a marked transition in the behavior of the shells at loads near $P^* = 2.2$. The load deflection curve changed slope rapidly. Archer's[5] predictions for theoretical buckling loads for caps without horizontal edge restraint were within 5% of $P^* = 2.2$ for λ greater than 8. At P^* near 2.2, the midsurface stresses under the load change from compression to tension. The bending moment under the load reaches a maximum value as a function of load. The determinant Δ in the numerical solution has a minimum at these transition loads but does not reach zero, which would serve to define snap-through buckling.

The load-deflection curves† are shown in Fig. 7 to 10. The curves are linear at low loads, change slope rapidly around $P^* = 2$, and are nearly linear again. As might be expected, a given load produces more deflection when applied over a small load area. There is relatively good agreement between theory and experiment for deflection. Some of the experimental curves have horizontal tangents (axisymmetric buckling) near the transition loads where the theoretical curves merely show flattening.

The transition loads are better defined by the midsurface stresses. As the dimple under the load gets larger, it reaches a point where the region around the load actually goes into tension. This is illustrated for a concentrated load with zero load area in Fig. 11.

†Properties and dimensions of all test specimens are listed in Table 1.

Once the load has formed a dimple of completely reversed curvature under the load area, the bending moment under the load does not increase with increasing load because the dimple tends to spread over a larger area rather than remaining confined to a small area. A typical plot of bending moment as a function of load is shown in Fig. 12 for shells with a nominal value of λ = 8. As the load area decreases, the maximum moment increases and is infinite at zero load area.

The growth of the dimple area under load is shown in plots of the deflection as a function of radius for given loads. Figures 13 and 14 show that most of the deflection is in the area of the load and the boundary of this dimpled shape moves outward with increasing load. These plots also show the slight difference between the deflection at the edge of the load area and the deflection at the center. The load-deflection curves in Fig. 7 thru 10 are plotted using the measured deflection at the apex of the shell while the theoretical curves use the deflection at the edge of the load area. If the measured deflections were started at the edge of the load area, instead of the apex the curves would show even better agreement than they do now. Figure 15 shows that the determinant of the algebraic equations in the computer solution dips toward zero at the transition load for a typical shell. As long as it does not change sign, the load-deflection curve is monotonic.

Some of the specimens yielded under the load. The theoretical point load produces infinite bending stresses. As the finite load area increases, these bending stresses tend to decrease. Figure 16 gives the load for which the shell first starts to yield at a shell surface. The load to produce yielding is plotted against load area for a shell with λ = 8.25 for different values of the yield stress. In Fig. 17, the radius of the load area is held constant at $r_p/b = 1/64$ to give the yield load as a function of λ.

All the preceding theoretical results have been obtained from the computer program to solve Reissner's equations. The test specimens exhibited asymmetric deflection modes at higher loads. An attempt was made to predict the bifurcation loads where the asymmetric solutions of the finite deflection equations intersect the axisymmetric solutions. The calculations used in the computer program are described in the appendix.

The axisymmetric stress resultants in a typical shell (B-43) are shown in Fig. 18. As a dimple forms under the load, the shell goes into tension near the apex. Near the edge of the dimple, a portion of the shell is pushed outward radially to produce a band of hoop compression around the shell. These circumferential stresses appear to be strong enough to produce the asymmetric mode shapes observed experimentally.

A further check on the computed axisymmetric stress state was attempted by putting strain gage rosettes on shell (B-43). The theoretical surface strains are compared with strain gage readings in Fig. 19 and 20. The two sets of data give fair agreement considering the rapid variation of the bending strain with radius. The large bending strains make it difficult to determine from strain gage data what the average strains are at the shell midsurface.

The computer program to check the axisymmetric stress state for bifurcation into asymmetric modes did not converge. It uses an iterative technique based on successive approximations to calculate eigenvalue λ_1. The eigenvalue λ_1 is defined as the multiplier that must multiply the axisymmetric stress state, such as the stress resultants in Fig. 18, in order to produce bifurcation into an asymmetric stress state.

As many as 15 iterations were run on a given shell. The value of λ_1 tended to oscillate slowly between positive and negative values without showing signs of converging. A convergent negative value of λ_1 would imply that a change in sign of the tensile stresses would produce buckling. The tensile and compressive stresses seemed to balance out so that the program gave no conclusive answer about the stability of the stress state.

The program prints out as the iteration proceeds, the current guess at the mode shape and additional stress resultants produced by buckling. A check of the terms in the differential equations multiplied by λ_1 revealed that terms in the axisymmetric rotation, β_x^o, were dominant. For example, where terms such as $N_x\beta_x$ appear in the finite deflection equilibrium equation, they are replaced by the expansion,

$$N_x\beta_x = N_x^o\beta_x^o + N_x^o\beta_{nx} + N_{nx}\beta_x^o.$$

The first term drops out of the "variational" equations and the last term is often dropped under the assumption that β_x^o is small. The terms in β_x^o are retained in the present analysis and these terms appear to be large in the iteration. It should be pointed out that the asymmetric buckles observed experimentally only occur at loads higher than those predicted by Archer for symmetrical buckling of caps free of horizontal restraint. At the time the experimental buckles form, β_x^o can be on the order of 0.1 so that the axisymmetric rotations are large. The effect this has on the iterative solution is not clear.

It is possible that the effect of asymmetric imperfections in shape must be included in the analysis before it will predict the transition to asymmetric modes observed experimentally.

B. EXPERIMENTAL RESULTS

By providing an extended range of shell geometry ($5 < \lambda < 22$), the data recorded from forty tests showed several types of shell behavior; such as, some of the shells suffered permanent set and did not buckle; some shells underwent progressively more complex nonaxisymmetric deflection with increasing load; some shells buckled with a single set of upper and lower critical buckling loads and other shells exhibited more than one set of such critical loads. These behaviors were identified from load-deflection curves at the apex, on a radial line, and along a circular line. In trying to determine consistency of shell response for the same value of λ from two different spherical radii, the data (in nondimensional form) do not fully support the use of λ as a common geometry parameter.

Inelastic behavior is shown on Fig. 21 and 22 for λ approximately five. Permanent deflection left at the apex is measured by the broken line, the length of which corresponds to the amount of set after that particular value of load was reduced to zero. Data of this kind were obtainable only with a program of increasing load because of the significant permanent change in shell geometry. The knee of the curve varied between $P^* = 1$ to $1\frac{1}{2}$ for $a = 20$ in. and between $P^* = 1\ 1/2$ to 2 for $a = 30$ in. Permanent set for the same load decreased with increasing load tip diameter and deflections were correspondingly less for larger load tip diameter.

Shells with nominal value of $\lambda = 8$ exhibited the same general behavior as shown for $\lambda = 5$. Permanent set occurred in all four shells in Fig. 23 for a = 20 in. Sections through the shells along a radial line are shown in Fig. 24 for all four loading tips and at several values of load. The knee varied from $P^* = 1\frac{1}{2}$ to $2\frac{1}{4}$. Figure 25, for a = 31 in., shows the same orderly progression of load-deflection curves for varying load area, however only the two smallest loading tips left permanent deflections in the shells. Deflections along a radial line are shown in Fig. 26. From Fig. 24 and 26, which show deflections on a radial line, the large departure between the shell and the loading tip illustrates the problem of attempting to provide a uniform pressure-like loading over a finite area. With this type of behavior, occurring over three orders of magnitude of maximum load, the only repeatable load application device was the hollow steel cylinder, as described earlier.

Buckling, as found from load-center deflection curves, is shown in Fig. 27 for λ nominally equal to 12, 16, and 20. The parallel dotted lines connecting two values of deflection for the same value of load are the upper and lower critical buckling loads. When the shell is on the left branch of the curve it is called prebuckled, and when it is on the right branch of the curve it is called postbuckled. This terminology is repeated at each of the separate sets of critical buckling loads and in addition each set identifies a mode of buckling with first mode occurring at the lowest pair of P^*_{cr} and so on. For shells with λ around 12, buckling occurred in one mode whereas higher values of λ produced two and three modes of buckling. A steady progression of three-lobed, four-lobed, and five-lobed deflection patterns originated in orderly fashion as shown in Fig. 27. No two-lobed deflection pattern was measured. The values of P^* at which nonaxisymmetric patterns were observed were as follows: three-lobed, $P^* = 6.2$ to 9.3; four-lobed, $P^* = 7.3$ to 11.0; five-lobed, $P^* = 8.5$ to 11.0. These values are not to be construed as limits or typical, merely as those at which such measurements were taken. In general, the four load-deflection curves in Fig. 27 have a similar appearance. Transitions from axisymmetric to three-lobed deflections, three-lobed to four-lobed and so on, appear to be related to changes in slope of these curves. Also, buckling into any of the modes is generally preceded by a flattening of the curve with increasing load as the upper critical buckling load is approached.

For $\lambda = 12$, buckling for a 20-in. spherical radius shell occurred only with the 1-in. diameter tip (Fig. 28). Nonaxisymmetric deflections, however, were apparent without buckling (Fig. 29). All loading tips caused buckling for the 31-in. spherical radius shell shown in Fig. 30, and three, four, and five-lobed deflections are shown by Fig. 31.

With $\lambda = 16$, nonaxisymmetric deflections were measured for 20-in. spherical radius and the four different load tips showed one, two, or three buckling modes per shell. These are shown in Fig. 32. A series of deflection measurements made on circles near the apex and near the boundary revealed the behavior shown in Fig. 33 and 34. The nonaxisymmetric deflections changed phase across the point of zero deflections (Fig. 24 and 26). Shells with 31-in. spherical radius showed behavior similar to those with 20-in. spherical radius, however they went on to higher values of both P^* and w_o/h, which are shown in Fig. 35. Figure 36 revealed a change in the deflection pattern where the number of lobes, having reached five, changed to four with increasing load. Both spherical radii exhibited first mode of buckling at $2 < P^* < 3$ for the 1-in. diameter load tip (the largest), whereas, the smallest load tips turned the corner of the knee without buckling.

Load-deflection curves for the highest value of λ tested are shown in Fig. 37 and 38. Again, the largest diameter load tip showed the occurrence of buckling at small values of P^* while the smaller load tips moved across the knee and did not buckle. For the 31-in. radius a single value of load produced a large number of stable postbuckled positions over many thicknesses of deflection.

A tabulation of upper and lower critical buckling loads and prebuckled and postbuckled deflections are given in Table 2. Photographs of three-lobed and five-lobed deflections, with the shell in the tester, are shown in Fig. 39 and 40.

Except for λ around 5 and 8 a predominantly nonaxisymmetric behavior pattern was observed to progress through multi-lobed deflections and through several modes of buckling with increasing load as λ became larger.

V. CONCLUDING REMARKS

From a practical standpoint, the most important result was that a clamped spherical cap carried a concentrated load at deflections many times the shell thickness and appeared to become stronger with larger deformations. The postbuckled equilibrium configurations did not lead to high stress levels. The largest deflections and stresses were confined to an area around the load, the size of which increased with increasing load. Until the dimple approached the clamped boundary, the portion of the shell near the boundary had low bending and low transverse shear stresses. It appeared that a complete sphere or hemisphere would provide the same type of support as the clamped boundary. Most of the results of the present investigation should be usable in the design of deeper spherical shells.

The agreement between the solutions of Reissner's equations and experiment was good. The calculated deflections and measured deflections agreed over a range of deflections many times the shell thickness. Some of the thicker shells yielded under the load so that Reissner's equations that are based on elastic theory did not apply for these shells. The shells yielded due to large bending moments. It seems feasible that practical results could be computed for these shells by replacing the boundary condition on rotation at the edge of the load area by a condition of the bending stress resultant, M_x, set equal to the plastic moment that the material can support. With the aid of this "plastic hinge", it is possible that useful results could be computed for the remainder of the shell until yielding starts at some other location.

Reissner's equations are based on axisymmetric theory so that they do not predict the asymmetric behavior observed experimentally. It was noted that the deflections calculated from Reissner's equations gave fair agreement with the average deflection around the circumference for the shells with asymmetric buckles.

The agreement between theory and experiment for the concentrated load is in marked contrast to the behavior of the same type of shell under external pressure. The authors recently completed a study[15] of pressure buckling of caps formed by the same method as those tested here. Good agreement between theory and experiment was obtained for shells under pressure by accounting for, in the analysis, deliberately formed initial imperfections of shape. The current results were calculated assuming a

spherical shape, using shells that were formed as perfectly as possible. The clamped cap under air pressure buckled suddenly and assumed an inverted shape that may have yielded the material near the clamped boundary.

An explanation for the difference in behavior under the two kinds of load has been advanced by Evan-Iwanowski[1]. The concentrated load produces bending under the load from the beginning of loading. The deflections in this area rapidly build up to more than the shell thickness. The dimple spreads with increasing load, but much of the shell is not highly stressed. Buckling pressures, on the other hand, are associated with deflections from one-half to one shell thickness. Initial imperfections of this same magnitude can be present in shells and, therefore, be a factor in determining buckling behavior.

The computer programs to calculate bifurcation loads associated with asymmetric deformation modes do no produce any convergent solutions. The tentative conclusion is that the theory does not reveal any asymmetric buckling modes for a perfect shell. The conclusion is tentative, because it is dangerous to base conclusions on lack of convergence of numerical solutions.

The analytical results predict high circumferential stresses in a narrow band at the edge of the dimple produced by the load. These stresses seem to cause the buckles observed in the experiments. It is not apparent whether the effect of initial imperfections must be included in the theory to account for the asymmetric buckles or not.

The computations using Reissner's equations do not define symmetric buckling. The load-deflection curves remain monotonic, but they have a flat slope at certain loads. The determinant Δ of the algebraic equations in the numerical solution must vanish in order to define buckling. At the loads where the load-deflection curves change slope, the determinant shows a minimum and convergence of the solution is slow, but the determinant does not reach zero (Fig. 15).

The stresses near the clamped boundary are not large, which raises the possibility that Archer[5] could have continued his solution for the cap free of horizontal edge restraint to higher values of load by taking smaller load increments in the calculations. The possibility seems worth investigating.

VI. REFERENCES

1. R. M. Evan-Iwanowski, H. S. Cheng, T. C. Loo: "Experimental Investigation of Deformations and Stability of Spherical Shells Subjected to Concentrated Load at the Apex." Proceedings of the Fourth U.S. National Congress of Applied Mechanics, 1962, p 563 thru 575.

2. D. G. Ashwell: "On the Large Deflection of a Spherical Shell with an Inward Point Load." Proc., I.U.T.A.M. Symp. on the Theory of Thin Elastic Shells, Delft, August 1959, North Holland Publ. Co., Amsterdam, 1960, p 43 thru 63.

3. R. M. Evan-Iwanowski, H. S. Cheng, T. C. Loo: "Deformations and Stability of Spherical Shells Under Action of Concentrated Loads." Syracuse University Research Institute Report No. TR 834-2, 1961.

4. R. M. Iwanowski: "Deformations and Stability of Spherical Shells Subjected to the Action of Asymmetrical Loadings - Experimental Study." Collected Papers on Instability of Shell Structures, NASA Technical Note D-1510, p 571 thru 585.

5. R. R. Archer: "On the Numerical Solution of the Nonlinear Equations For Shells of Revolution." Journal of Mathematics and Physics, Vol XLI, No. 3, September 1962, p 165 thru 178.

6. C. B. Biezeno: "Uber die Bestiminung der Durchlagkraft einer schwachgekrummten kreisformigen Platte." Z. angew Math. Mech., Vol 15, 1935, p 10 thru 22.

7. W. Z. Chien and H. C. Hu: "On the Snapping of a Thin Spherical Cap." Proceedings 9th International Congress of Applied Mechanics, Vol 6, University of Brussels, 1957, p 309 thru 337.

8. E. Reissner: "On Axisymmetrical Deformation of Thin Shells of Revolution." Proceedings of Symposia in Applied Mathematics, Vol 3, McGraw-Hill, New York, 1950, p 27 thru 52.

9. J. L. Sanders, Jr.: "Nonlinear Theories of Thin Shells." Technical Report No. 10, Contract Nonr. 1866 (02), Harvard University, 1961.

10. Collected Papers on Instability of Shell Structures. NASA Technical Note D-1510:

a) M. Stein: "The Effect of Buckling of Perfect Cylinders of Prebuckling Deformations and Stresses Induced by Edge Support," p 217 thru 227;

b) H. Weinitschke: "Asymmetric Buckling of Clamped Shallow Spherical Shells." p 481 thru 490;

c) R. R. Parmerter and Y. C. Fung: "On the Influence of Non-Symmetric Modes on the Buckling of Shallow Spherical Shells under Uniform Pressure." p 491 thru 499.

11. N. C. Huang: "Unsymmetrical Buckling of Shallow Spherical Shells." American Institute of Aeronautics and Astronautics Journal, Vol 1, No. 4, 1963, p 945 thru 946. Also, Harvard University Technical Report No. 15, March 1963. Also, Journal of Applied Mechanics, September 1964, p 447 thru 458.

12. G. Fischer: "Uber den Einfluss der gelenkigen Lagerung auf die Stabilitat dunnwandiger Kreiszylinderschalen Under Axiallast und Innendruck." Z. Flugwissenschaften, Vol 11, 1963, p 111 thru 119.

13. G. A. Thurston: Axisymmetric Bending and Buckling of Thin Shells of Revolution. Report SR-0530-64-2. Martin Company, Denver, Colorado, 1964.

14. G. A. Thurston: Effect of Imperfections on Nonlinear Axisymmetric Bending and Buckling of Thin Shells. General Electric Company Report R61FPD545, 1961.

15. G. A. Thurston and F. A. Penning: Effect of Initial Imperfections on the Stability of Shallow Spherical Shells. AFOSR Scientific Report No. 64-1627, 1964.

16. R. M. Bellman, M. L. Juncosa, and R. Kalaba: "Some Numerical Experiments Using Newton's Method for Nonlinear Parabolic and Elliptic Boundary-Value Problems." Communications of Association for Computing Machinery, Vol 4, No. 4, April 1961, p 187 thru 191.

17. S. A. Chaplygin: "A New Method for Approximate Integration of Differential Equations." 1905, recently printed under Classics of the Natural Sciences, Moscow, 1950.

18. G. A. Thurston: "A Numerical Solution for Thin Conical Shells Under Asymmetrical Loads." Proceedings of the Fourth Midwestern Conference on Solid Mechanics, The University of Texas Press, Austin, Texas, 1959, p 171 thru 194.

19. G. A. Thurston: Asymmetric Buckling of Shells of Revolution with Axisymmetric Initial Imperfections. General Electric Company Report R62FPD426, 1963.

20. G. A. Thurston: "Asymmetrical Buckling of Spherical Caps under Uniform Pressure." AIAA Journal, October 1964, p 1832 thru 1833.

21. G. A. Thurston: "Effect of Boundary Conditions on the Buckling of Conical Shells under Hydrostatic Pressure." Journal of Applied Mechanics, March 1965, p 208 thru 209.

APPENDIX

ASYMMETRIC BUCKLING THEORY

The theory is based on the strain expressions for small finite deflections that are listed by Sanders[9]. Bifurcation points in the load-deflection curves occur when two solutions of the differential equations intersect at the same point. The loads at these bifucation points can be determined from linearized theory once one of the two solutions is known.

For the solution considered here, the shells are shells of revolution under axisymmetric loads. The known solution is the nonlinear axisymmetric solution, and the bifucation points define loads where the shell has asymmetric equilibrium positions. The question of the stability of these asymmetric solutions is not answered by the linearized theory.

The nomenclature used in this appendix is defined as follows:

Notation - Asymmetric Analysis

C	Stretching stiffness of shell (lb/in.)
D	Bending stiffness of shell (lb-in.)
E	Young's modulus (psi)
f	Natural frequency (cps)
h	Shell thickness (in.)
$K_1 = \frac{1}{r_1}$	Curvature of meridian curve (in.^{-1})
$M_x, M_\theta, M_{x\theta}$	Moment stress resultants (in.-lb/in.)
n	Number of complete waves in circumferential direction of the buckled shell. Also used as superscript and subscript to denote buckling deflections and stress resultants that are superposed on axisymmetric stress state or the variation with x of these quantities
$N_{x\theta}$	Shear stress resultant in plane for shell surface (lb/in.)

N_x, N_θ	Normal stress resultants in meridional and circumferential directions (lb/in.)
$N_x^\circ, N_\theta^\circ, \beta_x^\circ$	Zero superscript denotes axisymmetric stress and deflections before buckling
q	External pressure $(lb/in.^2)$
Q_x, Q_θ	Shear stress resultants normal to deflected shell surface, (lb/in.)
r_1	Radius of curvature of shell meridian curve (in.)
r_o	Radius of shell perpendicular to the centerline (in.)
T	Buckling torque (in.-lb)
u, v, w	Deflections of shell middle surface in meridional, circumferential, and normal directions, respectively (in.)
x	Independent variable; r_o and z_o are functions of x
z_o	Axial dimension of any cross section of shell (in.)
β_x, β_θ	Rotation of tangents to shell middle surface in meridional and circumferential directions (radians)
$\lambda_1, \lambda_2, \lambda_3$	Eigenvalues
ν	Poisson's ratio
φ_o	Angle from centerline to normal of meridian curve of the undeformed shell
ρ	Mass density $(lb\text{-}sec^2/in.^4)$
θ	Circumferential coordinate of point on shell middle surface (radians)

Primes denote differentiation with respect to x.

The strain/displacement relations for the middle-surface strains in the finite deflection theory are:

$$\epsilon_x = \frac{1}{\alpha_o}\frac{\partial u}{\partial x} - \frac{w}{r_1} + \frac{1}{2}\beta_x^2; \qquad [A1a]$$

$$\epsilon_\theta = \frac{1}{r_o}\frac{\partial v}{\partial \theta} + \frac{u \cos \varphi_o}{r_o} - \frac{w \sin \varphi_o}{r_o} + \frac{1}{2}\beta_\theta^2; \qquad [A1b]$$

$$\epsilon_{x\theta} = \frac{1}{\alpha_o}\frac{\partial v}{\partial x} - \frac{\cos \varphi_o}{r_o} v + \frac{1}{r_o}\frac{\partial u}{\partial \theta} + \beta_x\beta_\theta. \qquad [A1c]$$

The changes in curvature are taken in the same form as in linear theory:

$$\kappa_x = \frac{1}{\alpha_o}\frac{\partial \beta_x}{\partial x}; \qquad [A2a]$$

$$\kappa_\theta = \frac{1}{r_o}\frac{\partial \beta_\theta}{\partial \theta} + \frac{\cos \varphi_o}{r_o}\beta_x; \qquad [A2b]$$

$$\kappa_{x\theta} = \frac{1}{\alpha_o}\frac{\partial \beta_\theta}{\partial x} + \frac{1}{r_o}\frac{\partial \beta_x}{\partial \theta} - \frac{\cos \varphi_o}{r_o}\beta_\theta. \qquad [A2c]$$

Neglecting transverse shear strain, the rotations of the shell normal are equal to the rotations of the tangents to the middle surface.

$$\beta_x = -\left(\frac{1}{\alpha_o}\frac{\partial w}{\partial x} + \frac{u}{r_1}\right); \qquad [A3a]$$

$$\beta_\theta = -\left(\frac{1}{r_o}\frac{\partial w}{\partial \theta} + \frac{v \sin \varphi_o}{r_o}\right). \qquad [A3b]$$

The constitutive relations are:

$$N_x = C\left(\epsilon_x + \nu\epsilon_\theta\right); \qquad [A4a]$$

$$N_\theta = C\left(\epsilon_\theta + \nu\epsilon_x\right); \qquad [A4b]$$

$$N_{x\theta} = \frac{C(1-\nu)}{2}\,\epsilon_{x\theta}. \qquad [A4c]$$

$$M_x = D\left(\kappa_x + \nu\kappa_\theta\right); \qquad [A5a]$$

$$M_\theta = D\left(\kappa_\theta + \nu\kappa_x\right); \qquad [A5b]$$

$$M_{x\theta} = \frac{D(1-\nu)}{2}\,\kappa_{x\theta}; \qquad [A5c]$$

where

$$C = \frac{Eh}{1-\nu^2} \text{ and } D = \frac{Eh^3}{12\left(1-\nu^2\right)}.$$

The equations of motion, which can be derived from Hamilton's principle using the strain energy expression associated with the above strains, are

$$\frac{\partial\left(r_o N_x\right)}{\partial x} + \alpha_o \frac{\partial N_{x\theta}}{\partial\theta} - \left(\alpha_o \cos\varphi_c\right) N_\theta - \frac{\alpha_o r_o}{r_1}\left(Q_x - N_x\beta_x - N_{x\theta}\beta_\theta\right)$$

$$= \alpha_o r_o \rho h \frac{\partial^2 u}{\partial t^2}; \qquad [A6a]$$

$$\frac{\partial\left(r_o N_{x\theta}\right)}{\partial x} + \alpha_o \frac{\partial N_\theta}{\partial\theta} + \alpha_o \cos\varphi_o\, N_{x\theta} - \alpha_o \sin\varphi_o\left(Q_\theta - N_{x\theta}\beta_x - N_\theta\beta_\theta\right)$$

$$= \alpha_o r_o \rho h \frac{\partial^2 v}{\partial t^2}; \qquad [A6b]$$

$$\frac{\partial(r_o Q_x)}{\partial x} + \alpha_o \frac{\partial Q_\theta}{\partial \theta} + \alpha_o r_o \left(\frac{N_x}{r_1} + \frac{N_\theta \sin \varphi_o}{r_o} \right) - \frac{\partial}{\partial x} (r_o N_x \beta_x + r_o N_{x\theta} \beta_\theta)$$

$$- \alpha_o \frac{\partial}{\partial \theta} (N_{x\theta} \beta_x + N_\theta \beta_\theta) + \alpha_o r_o q = \alpha_o r_o \rho h \frac{\partial^2 w}{\partial t^2}; \qquad [A6c]$$

$$\frac{\partial(r_o M_x)}{\partial x} + \alpha_o \frac{\partial M_{x\theta}}{\partial \theta} - \alpha_o M_\theta \cos \varphi_o = \alpha_o r_o Q_x; \qquad [A6d]$$

$$\frac{\partial(r_o M_{x\theta})}{\partial x} + \alpha_o \frac{\partial M_\theta}{\alpha \theta} + \alpha_o M_{x\theta} \cos \varphi_o = \alpha_o r_o Q_\theta. \qquad [A6e]$$

These nonlinear equations for the finite deflection theory do not reduce exactly to Reissner's equations for the axisymmetric static case, but the two solutions are equivalent as long as the rotation β_x of the shell normal is small enough that $\tan \beta_x$ can be approximately by β_x.

Having the axisymmetric solution, the procedure is to assume a solution to the nonlinear finite deflection equations in the form

$$u = u^o + u^n; \qquad [A7a]$$

$$v = v^o + v^n; \qquad [A7b]$$

$$w = w^o + w^n; \qquad [A7c]$$

where (u^o, v^o, w^o) represent displacements in the known axisymmetric solution. This solution also has known axisymmetric stress resultants, N_x^o, N_θ^o, and $N_{x\theta}^o$ along with the rotation β_x^o. $\beta_\theta^o = 0$ from axial symmetry.

The solution (u, v, w) is assumed near the axisymmetric one. This implies that the solution (u^n, v^n, w^n) is small and that nonlinear terms in these variables can be neglected. (The superscript n will later be associated with the number of circumferential waves in the buckled shape.) Neglecting these nonlinear terms obtains the equations of motion, Equations [A6], in the following forms:

$$\frac{\partial(r_o N_{nx})}{\partial x} + \alpha_o \frac{\partial(N_{nx\theta})}{\partial \theta} - \alpha_o N_{n\theta} \cos \varphi_o$$

$$- \frac{\alpha_o r_o}{r_1}\left(Q_{nx} - N^o_x \beta_{nx} - N_{nx}\beta^o_x - N^o_{x\theta}\beta_{n\theta}\right) = \alpha_o r_o \rho h \frac{\partial^2 u^n}{\partial t^2}; \qquad [A8a]$$

$$\frac{\partial(r_o N_{nx\theta})}{\partial x} + \alpha_o N_{nx\theta} \cos \varphi_o + \alpha_o \frac{\partial N_{n\theta}}{\partial \theta}$$

$$- \alpha_o \sin \varphi_o \left(Q_{n\theta} - N^o_{x\theta}\beta_{nx} - N_{nx\theta}\beta^o_x - N^o_\theta \beta_{n\theta}\right) = \alpha_o r_o \rho h \frac{\partial^2 v^n}{\partial t^n}; \qquad [A8b]$$

$$\frac{\partial(r_o Q_{nx})}{\partial x} + \frac{\alpha_o(\partial_o Q_{n\theta})}{\partial \theta} + \alpha_o r_o \left(\frac{N_{nx}}{r_1} + \frac{N_{n\theta} \sin \varphi_o}{r_o}\right)$$

$$- \frac{\partial}{\partial x}\left[r_o\left(N^o_x \beta_{nx} + N_{nx}\beta^o_x + N^o_{x\theta}\beta_{n\theta}\right)\right]$$

$$- \alpha_o \frac{\partial}{\partial \theta}\left(N^o_{x\theta}\beta_{nx} + N_{nx\theta}\beta^o_x + N^o_\theta \beta_{n\theta}\right) = \alpha_o r_o \rho h \frac{\partial^2 w^n}{\partial t^2}; \qquad [A8c]$$

$$\frac{\partial(r_o M_{nx})}{\partial x} + \alpha_o \frac{\partial M_{nx\theta}}{\partial \theta} - \alpha_o M_{n\theta} \cos \varphi_o = \alpha_o r_o Q_{nx}; \qquad [A8d]$$

$$\frac{\partial(r_o M_{nx\theta})}{\partial x} + \alpha_o \frac{\partial M_{n\theta}}{\partial \theta} + \alpha_o M_{nx\theta} \cos \varphi_o = \alpha_o r_o Q_{n\theta}; \qquad [A8e]$$

where the related constitutive and strain/displacement equations become

$$N_{nx} = C(\epsilon_{nx} + \nu \epsilon_{n\theta}); \qquad [A9a]$$

$$N_{n\theta} = C(\epsilon_{n\theta} + \nu \epsilon_{nx}); \qquad [A9b]$$

$$N_{nx\theta} = \frac{C(1 - \nu)}{2} \epsilon_{nx\theta}; \qquad [A9c]$$

$$M_{nx} = D(\kappa_{nx} + \nu\kappa_{n\theta}); \qquad [A10a]$$

$$M_{n\theta} = D(\kappa_{n\theta} + \nu\kappa_{nx}); \qquad [A10b]$$

$$M_{nx\theta} = \frac{D(1 - \nu)}{2} \kappa_{nx\theta}; \qquad [A10c]$$

$$\epsilon_{nx} = \frac{1}{\alpha_o} \frac{\partial u^n}{\partial x} - \frac{w^n}{r_1} + \beta_x^o \beta_{nx}; \qquad [A11a]$$

$$\epsilon_{n\theta} = \frac{1}{r_o} \frac{\partial v^n}{\partial \theta} + \frac{u^n \cos \varphi_o}{r_o} - \frac{w^n \sin \varphi_o}{r_o}; \qquad [A11b]$$

$$\epsilon_{nx\theta} = \frac{1}{\alpha_o} \frac{\partial v^n}{\partial x} - \frac{\cos \varphi_o}{r_o} v^n + \frac{1}{r_o} \frac{\partial u^n}{\partial \theta} + \beta_x^o \beta_{n\theta}; \qquad [A11c]$$

$$\kappa_{nx} = \frac{1}{\alpha_o} \frac{\partial \beta_{nx}}{\partial x}; \qquad [A12a]$$

$$\kappa_{n\theta} = \frac{1}{r_o} \frac{\partial \beta_{n\theta}}{\partial \theta} + \frac{\cos \varphi_o}{r_o} \beta_{nx}; \qquad [A12b]$$

$$\kappa_{nx\theta} = \frac{1}{\alpha_o} \frac{\partial \beta_{n\theta}}{\partial x} + \frac{1}{r_o} \frac{\partial \beta_{nx}}{\partial \theta} - \cos \varphi_o \beta_{n\theta}; \qquad [A12c]$$

$$\beta_{nx} = -\left(\frac{1}{\alpha_o} \frac{dw^n}{\partial x} + \frac{u^n}{r_1}\right); \qquad [A13a]$$

$$\beta_{n\theta} = -\left(\frac{1}{r_o} \frac{\partial w^n}{\partial \theta} + \frac{v^n \sin \varphi_o}{r_o}\right). \qquad [A13b]$$

The first three equations of motion, Equations [A8], can be reduced to a linear eighth-order set of partial differential equations in the unknown displacements u^n, v^n, and w^n. These equations are homogeneous, and buckling loads or natural frequencies are defined by non-zero solutions of these equations. The axial load and external pressure do not appear explicitly since the stress resultants N_x^o and N_θ^o are nonlinear functions of these loads.

To distinguish between different solutions of the equations, three multipliers are introduced in the computer solution. The terms from the solution of Reissner's equations $\left(N_x^o,\ N_\theta^o,\ \beta_x^o\right)$ are multiplied by λ_1, the membrane shear stress $N_{x\theta}{}^o = \dfrac{T}{2\pi r_o{}^2}$ is multiplied by λ_2, and the inertia terms multiplied by λ_3. Any of these multipliers can be specified in input to the program as an eigenvalue. For example, to determine the buckling torque for a given external pressure, λ_1 is set equal to unity, $\lambda_3 = 0$, and λ_2 becomes the eigenvalue that determines the buckling torque.

The sperical cap under concentrated load has $\lambda_2 = \lambda_3 = 0$, with λ_1 as the eigenvalue. When λ_1 is determined, it defines buckling as occurring when the axisymmetric stresses and rotation have been multiplied by λ_1. Since the relation between loads and stresses is nonlinear, the loads must be varied in the input data until $\lambda_1 = 1$ to exactly define the buckling loads.

After the substitutions are made to reduce the problem to an eighth-order set of linear partial differential equations, they are solved by successive approximations. All terms containing the eigenvalues $(\lambda_1,\ \lambda_2,\ \lambda_3)$ are put on the right side of the equations and an assumed solution is used for the unknown functions on the right side. The resulting nonhomogeneous equations are solved for the unknowns, which are normalized and substituted back into the right side as a new approximate solution. The normalization procedure involves adjusting the particular eigenvalue that is allowed to vary until the assumed solution is within a certain percentage (prescribed as input) of the new solution of the differential equations.

This type of solution converges to the lowest natural frequency for the shell for a given number of circumferential waves and will not give the higher frequencies. It also converges to the lowest buckling loads, but they are the only loads observed in practice so that this feature of the solution is not a disadvantage for buckling problems.

Before substituting in the equations in Equations [A8] to reduce them to their final form, a new dependent variable is introduced:

$$M^n = D(\kappa_{nx} + \kappa_{n\theta}). \qquad [A14]$$

The additional dependent variable is needed to fit the format of the numerical solution that is based on simultaneous second order differential equations. The choice of M^n leads to the Laplacian operating on M^n in Equation [A8c]. The Laplacian operator is simple to program in the numerical solution.

The transverse shear resultants defined by Equations [A8d] and [A8e] can then be expressed by

$$r_o Q_{nx} = \frac{r_o}{\alpha_o}\frac{\partial M^n}{\partial x} + D(1 - \nu)\left\{\frac{\sin\varphi_o}{r_1}\beta_{nx} + \frac{1}{2r_o}\frac{\partial}{\partial\theta}\left[\frac{1}{\alpha_o}\frac{\partial\left(v^n \sin\varphi_o\right)}{\partial x} - \right.\right.$$

$$\left.\left. - \frac{1}{r_1}\frac{\partial u^n}{\partial\theta}\right]\right\} - \frac{r_o}{\alpha_o}\frac{dD}{dx}(1 - \nu)\,\kappa_{n\theta}; \qquad [A15a]$$

$$r_o Q_{n\theta} = \frac{\partial M^n}{\partial\theta} + D(1 - \nu)\left\{\frac{\sin\varphi_o}{r_1}\beta_{n\theta} - \frac{r_o}{2\alpha_o}\frac{\partial}{dx}\left[\frac{1}{r_o\alpha_o}\frac{\partial}{dx}\left(v^n \sin\varphi_o\right) - \right.\right.$$

$$\left.\left. - \frac{1}{r_o r_1}\frac{\partial u^n}{\partial\theta}\right]\right\} + \frac{r_o(1 - \nu)}{2\alpha_o}\frac{dD}{dx}\kappa_{nx\theta}. \qquad [A15b]$$

Finally, the solution to the partial differential equations is assumed as

$$u^n = u_1(x)\cos n\theta + u_2(x)\sin n\theta; \qquad [A16a]$$

$$v^n = v_1(x)\sin n\theta + v_2(x)\cos n\theta; \qquad [A16b]$$

$$w^n = w_1(x)\cos n\theta + w_2(x)\sin n\theta; \qquad [A16c]$$

$$M^n = M_1(x)\cos n\theta + M_2(x)\sin n\theta. \qquad [A16d]$$

The second terms on the right of the preceding equations are only required for the torsional buckling problem. The successive approximation solution is particularly adapted to torsional buckling since the coupling between the functions of x having different subscripts 1 and 2 only occurs for terms multiplied by the eigenvalue λ_2 which appear on the right-hand side of the nonhomogeneous differential equations.

Substituting Equations [A16] into Equations [A9], [A10], [A11], [A12], [A13], and [A15], and the resulting equations into the first three equations of Equation [A8] and into Equation [A14], leads to a set of four simultaneous second-order ordinary differential equations of the form

$$L_{11}(u_1) + nL_{12}(v_1 / r_o) + L_{13}(w_1) + L_{14}(M_1) = L_1; \qquad [A17a]$$

$$nL_{21}(u_1) + L_{22}(v_1 / r_o) + nL_{23}(w_1) + nL_{24}(M_1) = L_2; \qquad [A17b]$$

$$L_{31}(u_1) + nL_{32}(v_1 / r_o) + L_{33}(w_1) + L_{34}(M_1) = L_3; \qquad [A17c]$$

$$L_{41}(u_1) + nL_{42}(v_1 / r_o) + L_{43}(w_1) + L_{44}(M_1) = 0. \qquad [A17d]$$

The number of circumferential waves, n, is factored out of the operators L_{12}, L_{21}, L_{23}, L_{32}, L_{24}, and L_{42} because these operators for u_2, v_2, w_2, and M_2 are then the same but n is changed to minus n. This allows using the same operators in the numerical solution by the device of changing the sign of Equation [A17b] and solving for $(-v_2/r_o)$ in iteration for the functions of x with subscript 2.

The operators in Equations [A17] for a shell of revolution are:

$$L_{11}(u) = \frac{d}{dx}\left(\frac{r_o C}{\alpha_o}\frac{du}{dx}\right) + \nu u \frac{d}{dx}(C \cos \varphi_o) - \frac{\alpha_o n^2 C(1 - \nu)u}{2r_o}$$

$$- \frac{\alpha_o C u}{r_o}\cos^2 \varphi_o + \frac{\alpha_o D(1 - \nu)u}{r_1^2}\left[\frac{\sin \varphi_o}{r_1} - \frac{n^2}{2r_o} - \frac{D'}{D}\cos \varphi_o\right];$$

$$L_{12}(y) = -\nu \frac{d(r_o Cy)}{dx} + \frac{r_o C(1-\nu)}{2} \frac{dy}{dx} - \alpha_o Cy \cos \varphi_o - \frac{D(1-\nu)}{2r_1 r_o}$$

$$\cdot \frac{d(r_o y \sin \varphi_o)}{dx} - \frac{\alpha_o D'(1-\nu) y \sin \varphi_o}{r_1} - \frac{D(1-\nu)}{r_1}$$

$$\cdot \left[\frac{1}{2r_o} \frac{d(r_o y \sin \varphi_o)}{dx} - \frac{D'}{D} \alpha_o y \sin \varphi_o \right];$$

$$L_{13}(w) = -\frac{d}{dx}\left(\frac{r_o Cw}{r_1}\right) - \nu \frac{d}{d_x} (Cw \sin \varphi_o) + \alpha_o Cw \left[\frac{\nu}{r_1} + \frac{\sin \varphi_o}{r_o}\right] \cos \varphi_o$$

$$+ \frac{D(1-\nu)}{r_1} \left[\frac{\sin \varphi_o}{r_1} \frac{dw}{dx} + \frac{D'}{D} \frac{n^2}{r_o} w - \frac{D'}{D} \frac{\cos \varphi_o}{\alpha_o} \frac{dw}{dx} \right];$$

$$L_{14}(M) = -\frac{r_o}{r_1} \frac{dM}{dx};$$

$$L_{21}(u) = -\frac{(1-\nu)}{2} \frac{d}{dx} (Cu) - \nu C \frac{du}{dx} - \frac{\alpha_o Cu(1+\nu) \cos \varphi_o}{2r_o}$$

$$+ \left(\frac{1-\nu}{2}\right) (\sin \varphi_o) \frac{d}{dx} \left(\frac{Du}{r_o r_1}\right);$$

$$L_{22}(y) = \frac{(1-\nu)}{2} \frac{d}{dx} \left(\frac{r_o^2 C}{\alpha_o} \frac{dy}{dx}\right) + \frac{r_o C(1-\nu)}{2} \frac{dy}{dx} \cos \varphi_o - \alpha_o Cn^2 y$$

$$+ D(1-\nu) \sin \varphi_o \left\{ \frac{1}{2} \frac{d}{dx} \left[\frac{1}{r_o \alpha_o} \frac{d}{dx} (r_o y \sin \varphi_o) \right] + \frac{\alpha_o y \sin^2 \varphi_o}{r_o r_1} \right.$$

$$\left. + \frac{D'}{D} \left[\frac{\sin \varphi_o \cos \varphi_o}{r_o} + \frac{1}{2r_o \alpha_o} \frac{d}{dx} (r_o y \sin \varphi_o) \right] \right\};$$

$$L_{23}(w) = \alpha_o Cw \left[\frac{\sin \varphi_o}{r_o} + \frac{\nu}{r_1}\right] - D(1 - \nu) \sin \varphi_o \left[\frac{w \sin \varphi_o}{r_o^2 r_1}\right.$$

$$\left. + \frac{D'}{D} \frac{1}{\alpha_o r_o} \frac{dw}{dx} - \frac{D'}{D} \frac{w \cos \varphi_o}{r_o^2}\right];$$

$$L_{24}(M) = -\alpha_o M \sin \varphi_o;$$

$$L_{31}(u) = C \left(\frac{r_o}{r_1} + \nu \sin \varphi_o\right) \frac{du}{dx} + \alpha_o Cu \cos \varphi_o \left(\frac{\nu}{r_1} + \frac{\sin \varphi_o}{r_o}\right) + (1 - \nu)$$

$$\cdot \left[-\frac{d}{dx}\left(\frac{Du \sin \varphi_o}{r_1^2}\right) + n^2 \frac{d}{dx}\left(\frac{Du}{r_o r_1}\right) + \frac{d}{dx}\left(\frac{D'u \cos \varphi_o}{\alpha_o r_1}\right)\right];$$

$$L_{32}(y) = \alpha_o r_o Cy \left(\frac{\nu}{r_1} + \frac{\sin \varphi_o}{r_o}\right) + (1 - \nu) \left\{\frac{d}{dx}\left[\frac{D}{2\alpha_o r_o} \frac{d}{dx}(y \sin \varphi_o)\right]\right.$$

$$- \frac{D}{2} \frac{d}{dx}\left[\frac{1}{\alpha_o r_o} \frac{d}{dx}(r_o y \sin \varphi_o)\right] - \alpha_o Dy \frac{\sin^2 \varphi_o}{r_o r_1} - \frac{d}{dx}$$

$$\left. \cdot \left(\frac{D'y \sin \varphi_o}{\alpha_o}\right) - \frac{D'}{2\alpha_o r_o} \frac{d}{dx}(r_o y \sin \varphi_o) + \frac{D'y}{r_o} \sin \varphi_o \cos \varphi_o\right\};$$

$$L_{33}(w) = -\alpha_o Cw \left[\frac{r_o}{r_1^2} + \frac{2\nu \sin \varphi_o}{r_1} + \frac{\sin^2 \varphi_o}{r_o}\right] + (1 - \nu) \left\{-\frac{d}{dx}\right.$$

$$\cdot \left(\frac{D \sin \varphi_o}{\alpha_o r_1} \frac{dw}{dx}\right) + \frac{d}{dx}\left(\frac{D' \cos \varphi_o}{\alpha_o^2} \frac{dw}{dx}\right) + n^2 \frac{d}{dx}\left(\frac{D'w}{\alpha_o r_o}\right)$$

$$\left. + \frac{n^2 D'}{\alpha_o r_o} \frac{dw}{dx} + \frac{n^2 Dw}{r_o^2}\left(\frac{\alpha_o \sin \varphi_o}{r_1} - \frac{D'}{D} \cos \varphi_o\right)\right\};$$

$$L_{34}(M) = \frac{d}{dx}\left(\frac{r_o}{\alpha_o}\frac{dM}{dx}\right) + \frac{\alpha_o n^2}{r_o} M;$$

$$L_{41}(u) = \frac{1}{\alpha_o}\frac{d}{dx}\left(\frac{u}{r_1}\right) + \frac{\alpha_o u \cos \varphi_o}{r_o r_1};$$

$$L_{42}(y) = \frac{\alpha_o y \sin \varphi_o}{r_o};$$

$$L_{43}(w) = \frac{d}{dx}\left(\frac{1}{\alpha_o}\frac{dw}{dx}\right) + \frac{\cos \varphi_o}{r_o}\frac{dw}{dx} - \frac{\alpha_o n^2 w}{r_o^2};$$

$$L_{44}(M) = \frac{\alpha_o}{D} M;$$

$$L_1 = \lambda_1 \left[\frac{d}{dx}\left(r_o C \beta_x^o \beta_{nx}\right) - \frac{\alpha_o Cn(1-\nu)}{2}\beta_x^o \beta_{n\theta} + \nu\alpha_o C (\cos \varphi_o) \cdot \beta_x^o \beta_{nx}\right] - \lambda_1 \frac{\alpha_o r_o}{r_1}\left(N_x^o \beta_{nx} + N_{nx}\beta_x^o\right) - \lambda_2 \frac{\alpha_o r_o}{r_1} N_{x\theta}^o \beta_{n\theta} - \lambda_3 \alpha_o r_o \rho h u;$$

$$L_2 = \lambda_1 \left[-\frac{(1-\nu)}{2}\frac{d}{dx}\left(r_o C \beta_x^o \beta_{nx}\right) - \frac{\alpha_o C(1-\nu)}{2}\beta_x^o \beta_{n\theta} \cos \varphi_o - \nu\alpha_o Cn \beta_x^o \beta_{nx}\right] - \lambda_1 \alpha_o N_\theta^o \beta_{n\theta} \sin \varphi_o - \lambda_2 \alpha_o \sin \varphi_o N_{x\theta}^o \beta_{nx} - \lambda_3 \alpha_o r_o^2 \rho h \left(\frac{v}{r_o}\right);$$

$$L_3 = \lambda_1 \left[-\alpha_o r_o C \beta_x^o \beta_{nx}\right] + \lambda_1 \left[\frac{d}{dx}\left(r_o N_x^o \beta_{nx} + r_o N_{nx}\beta_x^o\right) + n\alpha_o N_\theta^o \beta_{n\theta}\right] + \lambda_2 \left[\frac{d}{dx}\left(r_o N_{x\theta}^o \beta_{n\theta}\right) - n\alpha_o N_{x\theta}^o \beta_{nx}\right] - \lambda_3 \alpha_o r_o \rho h w.$$

The terms in the operators L_1, L_2, and L_3 are, strictly speaking, not correct. The factors sin $n\theta$ and cos $n\theta$ must be divided in the proper terms. If the buckling torque

$$T = 2\pi r_o \lambda_2 N^o_{x\theta}$$

is to be determined, signs must be checked after each iteration to obtain approximations for first functions of x with subscript 1 and then subscript 2, defined in Equations [A16]. Since $\lambda_2 = 0$ for the present study these terms will be neglected in the following discussion. The eigenvalue

$$\lambda_3 = (2\pi f)^2$$

appears if the problem is to find f, the natural frequency of harmonic motion for the shell, where u^n, v^n, and w^n serve to define the mode shape.

Numerical Solution - The set of four simultaneous second-order ordinary differential equations (Equations [A17]) have variable coefficients and must be solved numerically. The numerical solution consists of converting the differential equations to integral equations. The integrals appearing in the integral equations are replaced by mechanical quadrature formulas with the result that the integral equations are replaced by a set of linear algebraic equations.

The differential equations, Equations [A17], are of the general form

$$\sum_{j=1}^{n} R_{ij}(x)y_j''(x) + P_{ij}(x)y_j'(x) + Q_{ij}(x)y_j(x) = F_i(x), \qquad [A18]$$

$$i = 1, 2, \cdots m$$

$$m = n = 4$$

$$a \leq x \leq b$$

where

$$y_1 = u,$$

$$y_2 = v/r_o,$$

$$y_3 = w,$$

$$y_4 = M.$$

Primes denote differentiation with respect to x.

After integrating by parts twice, the equations become

$$\sum_{j=1}^{n} R_{ij}(x)y_j(x) = \sum_{j=1}^{n} \left[R_{ij}(a)y_j(a) \frac{(b - x)}{(b - a)} + R_{ij}(b)y_j(b) \frac{(x - a)}{(b - a)} \right.$$

$$- \int_a^b \frac{\partial K(x,t)}{\partial t} \left[\sum_{j=1}^{n} H_{ij}(t)y_j(t) \right] dt + \int_a^b K(x,t)$$

$$\cdot \left. \left[\sum_{j=1}^{n} G_{ij}(t)y_j(t) - F_i(t) \right] dt; \right. \qquad [A19]$$

where

$$H_{ij}(x) = P_{ij}(x) - 2R'_{ij}(x);$$

$$G_{ij}(x) = Q_{ij}(x) - P'_{ij}(x) + R''_{ij}(x);$$

$$K(x,t) = \begin{cases} (b - x)(t - a)/(b - a) & a \leq t \leq x \\ (b - t)(x - a)/(b - a) & x \leq t \leq b \end{cases}$$

$$\frac{\partial K(x,t)}{\partial t} = \begin{cases} (b - x)/(b - a) & a \leq t < x \\ -(x - a)/(b - a) & x < t \leq b. \end{cases}$$

The algebraic equations are derived from the following quadrature formulas:

$$\int_a^b \frac{\partial K(x,t)}{\partial t} H_{ij}(t)y_j(t)dt = -\sum_{r=1}^{\ell} A_r(x)H_{ij}(t_r)y_j(t_r); \qquad [A20a]$$

$$\int_a^b K(x,t)\, G_{ij}(t)y_j(t)dt = \sum_{r=1}^{\ell} B_r(x)G_{ij}(t_r)y_j(t_r). \qquad [A20b]$$

The method of computing the sets of quadrature coefficients $A_r(x)$ and $B_r(x)$ is derived in Ref 18. Since the kernels $K(x,t)$ and $\partial K(x,t)/\partial t$ are used as weight functions, their discontinuities at $x = t$ do not affect the accuracy of the quadrature formulas. However, this means that a different set of quadrature coefficients are required at each station $x_r = t_r$ in the numerical solution. These coefficients are arranged as two matrices $\underset{\sim}{A}_r(x_k)$ and $\underset{\sim}{B}_r(x_k)$.

The integral equations (Equation [A19]) become

$$\sum_{j=1}^{4} \left(\underset{\sim}{R}_{ij} + \underset{\sim}{A}_{ij} + \underset{\sim}{B}_{ij} \right) y_j(x_r) = \underset{\sim}{B}_r(x_k)F_i(x_r) \qquad [A21]$$

$$i = 1, 2, 3, 4.$$

The terms $\underset{\sim}{R}_{ij}$, $\underset{\sim}{A}_{ij}$, and $\underset{\sim}{B}_{ij}$ are matrices that multiply the column vectors $y_j(x_r)$. They are written from the quadrature formulas as the formal product of a matrix times a column vector

$$\underset{\sim}{A}_{ij} = \underset{\sim}{A}_r(x_k)H_{ij}(x_r); \qquad [A22a]$$

$$\underset{\sim}{B}_{ij} = \underset{\sim}{B}_r(x_k)G_{ij}(x_r). \qquad [A22b]$$

The matrices $\underset{\sim}{R}_{ij}$ are written from the functions $R_{ij}(x)$. The first and last columns of $\underset{\sim}{R}_{ij}$ are

$$R_{ij}(a)(b - x_k)/(b - a) \text{ and } R_{ij}(b)(x_k - a)/(b - a).$$

The trace of $\underset{\sim}{R}_{ij}$ is $-R_{ij}(x_k)$ and the remaining terms are zero.

The set of algebraic Equations [A21] contains $4(\ell - 2)$ equations in 4ℓ unknowns. The remaining eight equations follow from the boundary conditions.

The functions $R_{ij}(x)$, $H_{ij}(x)$, and $G_{ij}(x)$ associated with the differential Equations [A17] are programed in the following form[19]:

$$R_{11} = \frac{r_o C}{\alpha_o};$$

$$H_{11} = -\frac{C}{\alpha_o}\left[r_o' + r_o\left(\frac{C'}{C} - \frac{\alpha_o'}{\alpha_o}\right)\right];$$

$$G_{11} = -\frac{\alpha_o C}{r_o}\left[\cos^2\varphi_o + \frac{n^2(1-\nu)}{2}\right] + \nu C\left[\frac{C'}{C}\cos\varphi_o - \alpha_o K_1 \sin\varphi_o\right] - \alpha_o K_1^2 D(1-\nu)\left[\frac{n^2}{2r_o} - K_1 \sin\varphi_o + \frac{D'}{D}\frac{\cos\varphi_o}{\alpha_o}\right].$$

$$R_{12} = 0;$$

$$H_{12} = \frac{nr_o C(1+\nu)}{2} - \frac{nD(1-\nu)}{2} K_1 \sin\varphi_o;$$

$$G_{12} = -\frac{n\alpha_o C(3-\nu)\cos\varphi_o}{2} - \frac{nr_o(1-\nu)C'}{2} + \frac{nD(1-\nu)}{2}(\sin\varphi_o)\left[K_1' - K_1\frac{r_o'}{r_o} - \frac{D'}{D}K_1\right].$$

$$R_{13} = 0;$$

$$H_{13} = -C\left[r_o K_1 + \nu \sin \varphi_o\right] - DK_1(1 - \nu)\left[\frac{D'}{D}\frac{\cos \varphi_o}{\alpha_o} - K_1 \sin \varphi_o\right];$$

$$G_{13} = \alpha_o C \cos \varphi_o \left[\frac{\sin \varphi_o}{r_o} + \nu K_1\right] + \frac{n^2 K_1 D'(1 - \nu)}{r_o}$$

$$- DK_1(1 - \nu)\left[K_1 \frac{D'}{D} \sin \varphi_o + 2K_1' \sin \varphi_o + \alpha_o K_1^2 \cos \varphi_o\right]$$

$$+ \left[\frac{K_1 D'(1 - \nu) \cos \varphi_o}{\alpha_o}\right]'.$$

$$R_{14} = 0;$$

$$H_{14} = -r_o K_1;$$

$$G_{14} = \left[r_o K_1' + r_o' K_1\right].$$

$$R_{21} = 0;$$

$$H_{21} = -\frac{nC(1 + \nu)}{2} + \frac{nD(1 - \nu)(\sin \varphi_o)K_1}{2r_o};$$

$$G_{21} = -\frac{n\alpha_o C(3 - \nu) \cos \varphi_o}{2r_o} + \nu n C'$$

$$- \frac{nK_1 D(1 - \nu)}{r_o}\left[\frac{D'}{D} \sin \varphi_o + \frac{\alpha_o K_1 \cos \varphi_o}{2}\right].$$

$$R_{22} = \frac{(1 - \nu)}{2\alpha_o}\left[r_o^2 C + D \sin^2 \varphi_o\right];$$

$$H_{22} = -\frac{r_o C(1-\nu)}{2\alpha_o}\left[r_o' + r_o\left(\frac{C'}{C} - \frac{\alpha_o'}{\alpha_o}\right)\right]$$

$$- D(1-\nu)\left[K_1 \cos\varphi_o + \frac{\sin\varphi_o}{2\alpha_o}\left(\frac{D'}{D} - \frac{r_o'}{r_o} - \frac{\alpha_o'}{\alpha_o}\right)\right]\sin\varphi_o;$$

$$G_{22} = -n^2\alpha_o C - \frac{C(1-\nu)}{2}\left[r_o' \cos\varphi_o - \alpha_o r_o K_1 \sin\varphi_o + \frac{r_o C'}{C}\cos\varphi_o\right]$$

$$+ \frac{D(1-\nu)}{2}\left[\left(K_1 - \frac{2\sin\varphi_o}{r_o}\right)\left(\frac{D'}{D}\cos\varphi_o - \alpha_o K_1 \sin\varphi_o\right)\right.$$

$$\left. + K_1' \cos\varphi_o - \frac{\alpha_o K_1 \cos^2\varphi_o}{r_o}\right]\sin\varphi_o.$$

$$R_{23} = 0;$$

$$H_{23} = -\frac{nD'(1-\nu)\sin\varphi_o}{\alpha_o r_o};$$

$$G_{23} = n\alpha_o C\left(\frac{\sin\varphi_o}{r_o} + \nu K_1\right) - \frac{\alpha_o n D(1-\nu)K_1 \sin^2\varphi_o}{r_o^2}$$

$$+ \frac{n(1-\nu)}{r_o}\left[\frac{D'\sin\varphi_o}{\alpha_o}\right]'.$$

$$R_{24} = 0;$$

$$H_{24} = 0;$$

$$G_{24} = \frac{n\alpha_o \sin\varphi_o}{r_o}.$$

$$R_{31} = 0;$$

$$H_{31} = C\left[r_o K_1 + \nu \sin \varphi_o\right] - DK_1(1 - \nu)\left[K_1 \sin \varphi_o - \frac{D'}{D}\frac{\cos \varphi_o}{\alpha_o}\right];$$

$$G_{31} = -C\left[r_o'\left(K_1 - \frac{\sin \varphi_o}{r_o}\right) + r_o K_1'\right] - C'\left[r_o K_1 + \nu \sin \varphi_o\right]$$

$$+ n^2 K_1 D'(1 - \nu)\, r_o.$$

$$R_{32} = 0;$$

$$H_{32} = \frac{nD'(1 - \nu) \sin \varphi_o}{\alpha_o};$$

$$G_{32} = n\alpha_o C\left[\nu r_o K_1 + \sin \varphi_o\right]$$

$$- \frac{nD(1 - \nu) \sin \varphi_o}{r_o}\left[\alpha_o K_1 \sin \varphi_o - \frac{D'}{D}\cos \varphi_o\right].$$

$$R_{33} = -\frac{D(1 - \nu)}{\alpha_o}\left[K_1 \sin \varphi_o - \frac{D'}{D}\frac{\cos \varphi_o}{\alpha_o}\right];$$

$$H_{33} = \frac{D(1 - \nu)}{\alpha_o}\left[K_1\left(\frac{D'}{D} - \frac{\alpha_o'}{\alpha_o}\right)\sin \alpha_o + K_1' \sin \varphi_o + \alpha_o K_1^2 \cos \varphi_o\right]$$

$$- \left[\frac{D'(1 - \nu) \cos \varphi_o}{\alpha_o^2}\right]';$$

$$G_{33} = -\alpha_o C\left[r_o K_1^2 + 2\nu K_1 \sin \varphi_o + \frac{\sin^2 \varphi_o}{r_o}\right]$$

$$+ \frac{n^2 \alpha_o K_1 D(1 - \nu) \sin \varphi_o}{r_o^2} - \frac{n^2(1 - \nu)}{r_o}\left(\frac{D'}{\alpha_o}\right)'.$$

$$R_{34} = \frac{r_o}{\alpha_o};$$

$$H_{34} = -\cos \varphi_o + \frac{r_o}{\alpha_o}\left(\frac{\alpha_o'}{\alpha_o}\right);$$

$$G_{34} = -\frac{n^2 \alpha_o}{r_o}.$$

$$R_{41} = 0;$$

$$H_{41} = K_1;$$

$$G_{41} = \frac{\alpha_o K_1 \cos \varphi_o}{r_o}.$$

$$R_{42} = 0;$$

$$H_{42} = 0;$$

$$G_{42} = \frac{\alpha_o n \sin \varphi_o}{r_o}.$$

$$R_{43} = \frac{1}{\alpha_o};$$

$$H_{43} = \frac{1}{\alpha_o}\left(\frac{\alpha_o'}{\alpha_o}\right) + \frac{\cos \varphi_o}{r_o};$$

$$G_{43} = \frac{1}{r_o}\left[\alpha_o K_1 \sin \varphi_o + \frac{r_o'}{r_o} \cos \varphi_o - \frac{\alpha_o n^2}{r_o}\right].$$

$$R_{44} = 0;$$

$$H_{44} = 0;$$

$$G_{44} = \frac{\alpha_o}{D}.$$

The right hand sides of Equations [A21] are not programed as indicated there, the functions on the right of the differential equations, Equations [A17], contain derivatives of known terms. Rather than compute the derivatives numerically, these terms are integrated by parts, twice, along with the left sides of the differential equation. The right sides of the algebraic equations, Equations [A21], are written in the program as a vector defined by

$$\underset{\sim}{A}_r(x_k)F_{jy}(x_r) + \underset{\sim}{B}_r(x_k)F_j(x_r) \qquad j = 1,2,3,4$$

where the functions appearing in the present problem are

$$F_{1y}(x) = -\lambda_1 r_o C\beta_x^\circ \beta_{nx}. \qquad [A23a]$$

$$F_1(x) = \lambda_1 C\alpha_o \beta_x^\circ \left[\nu\beta_{nx} \cos\varphi_o - \frac{(1-\nu)}{2} n\beta_{n\theta}\right] - \lambda_1 \alpha_o r_o K_1 \left[N_x^\circ \beta_{nx} + N_{nx}\beta_x^\circ\right]. \qquad [A23b]$$

$$F_{2y}(x) = -\lambda_1 \frac{(1-\nu)}{2} r_o C\beta_x^\circ \beta_{n\theta}. \qquad [A23c]$$

$$F_2(x) = -\lambda_1 \alpha_o C\beta_x^\circ \left[\frac{(1-\nu)}{2} \beta_{n\theta} \cos\varphi_o + \nu n\beta_{nx}\right] - \lambda_1 \alpha_o N_\theta^\circ \beta_{n\theta} \sin\varphi_o. \qquad [A23d]$$

$$F_{3y}(x) = \lambda_1 r_o \left(\beta_x^\circ N_{nx} + N_x^\circ \beta_{nx}\right). \qquad [A23e]$$

$$F_3(x) = -\lambda_1 \alpha_o C\beta_x^\circ \beta_{nx} \left[r_o K_1 + \nu \sin\varphi_o\right] + \lambda_1 n\alpha_o N_\theta^\circ \beta_{n\theta}. \qquad [A23f]$$

The problem now is to find λ_1 by iteration since β_{nx}, $\beta_{n\theta}$, and N_{nx} are expressed as functions of $u_1(x)$, (v_1/r_o), $w_1(x)$, and $M_1(x)$, the dependent variables. The iteration starts by assuming

$$u_1 = 0,\ v_1/r_o = 0,\ w_1(x) = 0.1 + \sin\frac{\pi(x-a)}{(b-a)},\ \text{and}\ \lambda_1 = 1.$$

The terms in Equations [A23] are computed from the formulas

$$\beta_{nx} = -\frac{1}{\alpha_o}\frac{dw_1}{dx} - \frac{u_1}{r_1};$$

$$\beta_{n\theta} = \frac{nw_1}{r_o} - \left(\frac{v_1}{r_o}\right)\sin\varphi_o;$$

$$N_{nx} = C\left[\frac{1}{\alpha_o}\frac{du_1}{dx} - \frac{w_1}{r_1} + \beta^{\circ}{}_x\beta_{nx}\right] + \nu C\left[n\left(\frac{v_1}{r_o}\right) + \frac{u_1\cos\varphi_o - w\sin\varphi_o}{r_o}\right].$$

The terms with zero superscript are known solutions of Reissner's equations.

After each iteration, the solution is normalized by making λ_1 times the maximum value of the $w_1(x_r)$ vector equal to the same product from the previous iteration. This prevented underflow or overflow in the computer. The iterations proceed until successive values of λ_1 fall within a prescribed tolerance that is entered as input.

The value of λ_1 then defines the factor that must be multiplied times the axisymmetric solution to produce bifurcation. The axisymmetric load must be varied until $\lambda_1 = 1$ to obtain an exact answer.

The algebraic equations, Equations [A21], are solved by a Gaussian elimination subroutine that was written by L. Moore. It has the feature that the operations used to reduce the matrix on the left side of the equations to triangular form are stored in the computer. The back substitution is written as a separate subroutine so that the iteration process only consists of calling the back substitution subroutine. This results in a great saving of machine time compared to inverting a matrix for each iteration.

As part of the checkout procedure for the computer program, data were calculated for comparison with solutions of problems that have appeared in the literature. All results were satisfactory. Two special cases are discussed in Ref 20 and 21.

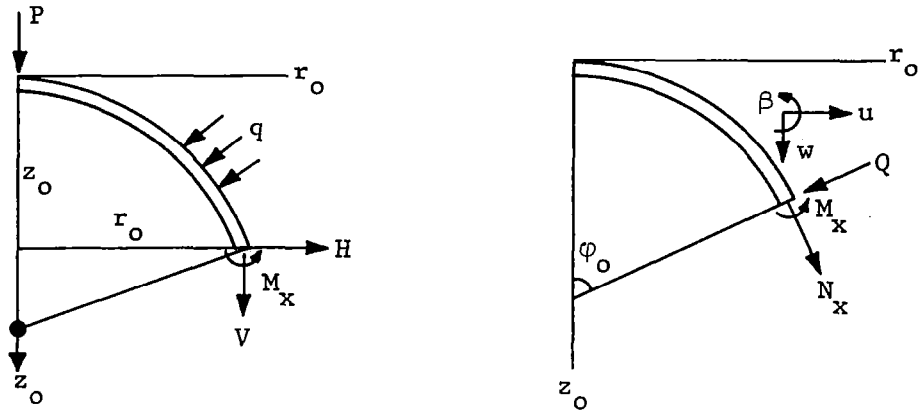
Table 1 Shell Properties

Shell Number	Load Tip Diameter, 2 r_p (in.)	Radius of Curvature, a (in.)	Thickness, h (in.)	λ
B-30	0.125	20.0	0.1090	4.92
B-49	0.25	20.0	0.1065	4.97
B-31	0.5	20.0	0.1090	4.92
B-32	1.0	20.0	0.1080	4.95
B-33	0.125	20.0	0.0385	8.27
B-50	0.25	20.0	0.0391	8.24
B-34	0.5	20.0	0.0390	8.22
B-35	1.0	20.0	0.0390	8.22
B-37	0.125	20.0	0.0182	12.0
B-41	0.25	20.0	0.0169	12.5
B-44	0.5	20.0	0.0175	12.3
B-38	1.0	20.0	0.0165	12.6
B-43	0.125	20.0	0.0102	16.1
B-43	0.25	20.0	0.0102	16.1
B-43	0.5	20.0	0.0102	16.1
B-43	1.0	20.0	0.0102	16.1
B-36	0.125	20.0	0.0066	20.0
B-36	0.25	20.0	0.0066	20.0
B-36	0.5	20.0	0.0066	20.0
B-36	1.0	20.0	0.0066	20.0
B-45	0.125	30.0	0.0687	5.05
B-46	0.25	30.0	0.0687	5.05
B-47	0.5	30.5	0.0690	4.98
B-48	1.0	31.0	0.0687	4.95
B-55	0.125	31.0	0.0270	7.29
B-52	0.25	31.0	0.0266	7.97
B-27	0.5	31.0	0.0271	7.90
B-27	1.0	31.0	0.0271	7.90
B-24	0.125	31.0	0.0125	11.6
B-24	0.25	31.0	0.0125	11.6
B-24	0.5	31.0	0.0125	11.6
B-24	1.0	31.0	0.0125	11.6
B-26	0.125	31.0	0.0069	15.6
B-26	0.25	31.0	0.0069	15.6
B-26	0.5	31.0	0.0069	15.6
B-26	1.0	31.0	0.0069	15.6
B-53	0.125	31.0	0.0037	21.4
B-53	0.25	31.0	0.0037	21.4
B-53	0.5	31.0	0.0037	21.4
B-53	1.0	31.0	0.0037	21.4

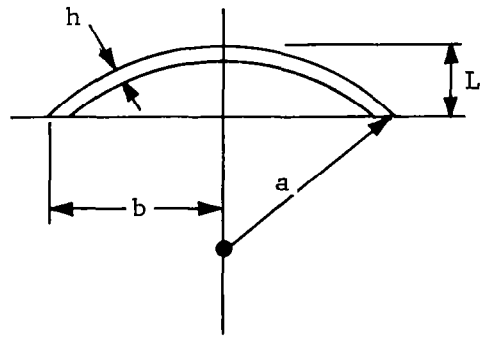
Mat'l Properties $E = 10^7$ psi, $\nu = 1/3$.

Table 2 Experimental Upper and Lower Critical Buckling Loads and Deflections

Shell	λ	a (in.)	Load Diameter, $2r_p$ (in.)	Upper			Lower		
				P^*_{cr}	w_o/h		P^*_{cr}	w_o/h	
					Pre	Post		Pre	Post
B-24	11.6	31.0	1/8	12.31	28.4	28.9	10.79	26.6	26.8
			1/4	12.11	28.2	28.8			
			1/2	11.92	27.6	28.4	10.79	26.1	26.4
			1	11.45	26.8	27.2	9.73	24.6	24.7
B-38	12.6	20.0	1	7.35	22.2	23.0	7.32	22.2	23.0
B-26	15.6	31.0	1/8	7.92	33.5	36.7	7.35	30.6	35.8
				14.15	55.2	55.9	13.61	54.7	55.3
				15.85	58.0	61.0	15.57	57.8	59.1
			1/4	8.21	35.1	37.3	8.01	34.2	37.1
				14.15	55.2	56.5	13.61	54.6	55.5
				18.12	61.1	62.7	16.99	59.5	61.3
			1/2	8.06	35.7	37.3	7.97	34.3	36.3
				14.12	54.6	55.9	13.56	54.2	54.6
			1	2.83	1.5	5.4	2.41	2.8	5.1
				8.49	34.8	38.2	8.21	34.5	36.4
				16.42	57.6	58.8	14.44	55.0	56.0
B-43	16.1	20.0	1/8	8.08	25.4	26.0	7.51	22.8	23.4
				10.26	42.5	45.1	9.94	40.9	43.8
			1/4	7.91	24.3	24.9	7.29	21.8	22.2
			1/2	2.72	1.2	3.6	2.27	0.7	1.8
				7.50	22.3	22.8	7.10	19.6	21.0
				9.20	32.8	33.4	8.17	25.9	27.0
			1	2.87	3.9	4.8	2.83	2.1	3.8
				9.32	33.2	34.3	8.48	26.6	28.8
				10.46	42.2	45.0	9.77	37.3	40.3
B-36	20.0	20.0	1/8	10.45	56.7	62.5	10.05	46.2	46.4
			1/4	7.80	28.3	29.9	7.62	27.0	28.0
				10.85	67.2	69.2	10.00	46.2	50.1
			1/2	2.48	1.6	3.1	2.43	1.3	1.4
				11.17	68.4	75.9	10.77	52.6	63.6
			1	2.92	2.4	3.5	2.51	1.4	1.6
				10.87	53.0	66.5	10.05	45.8	53.7
B-53	21.4	31.0	1/8	5.70	13.3	18.3	4.96	9.1	10.0
			1/4	8.27	36.1	115.0			
			1/2	9.20	34.0	40.0	8.07	30.3	36.3
			1	3.67	5.9	14.9	2.57	3.4	10.5



a. Notation for Reissner's Equations



b. Notation for Spherical Cap

Fig. 1 Notations

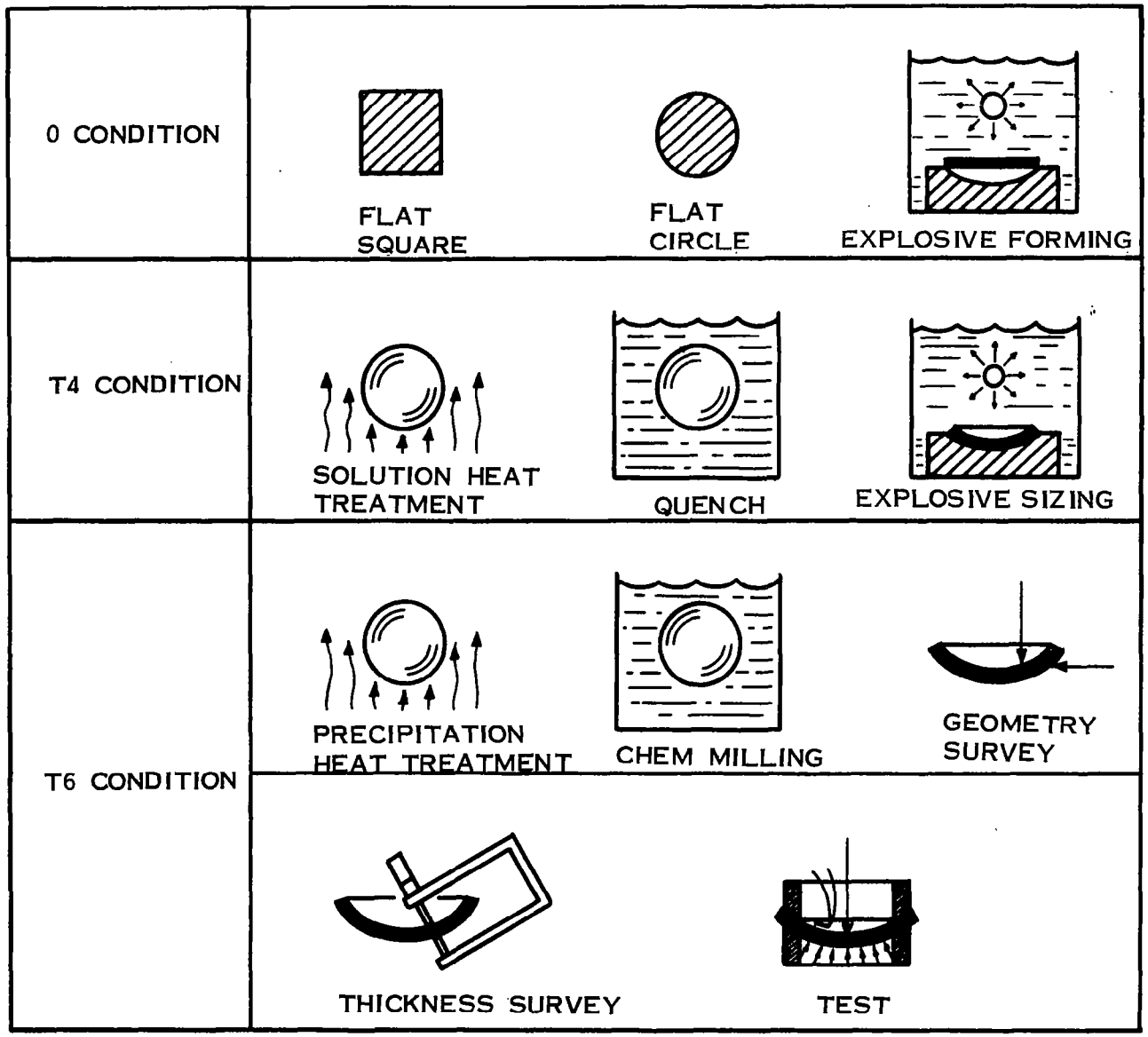


Fig. 2 Procedure for Forming Shells

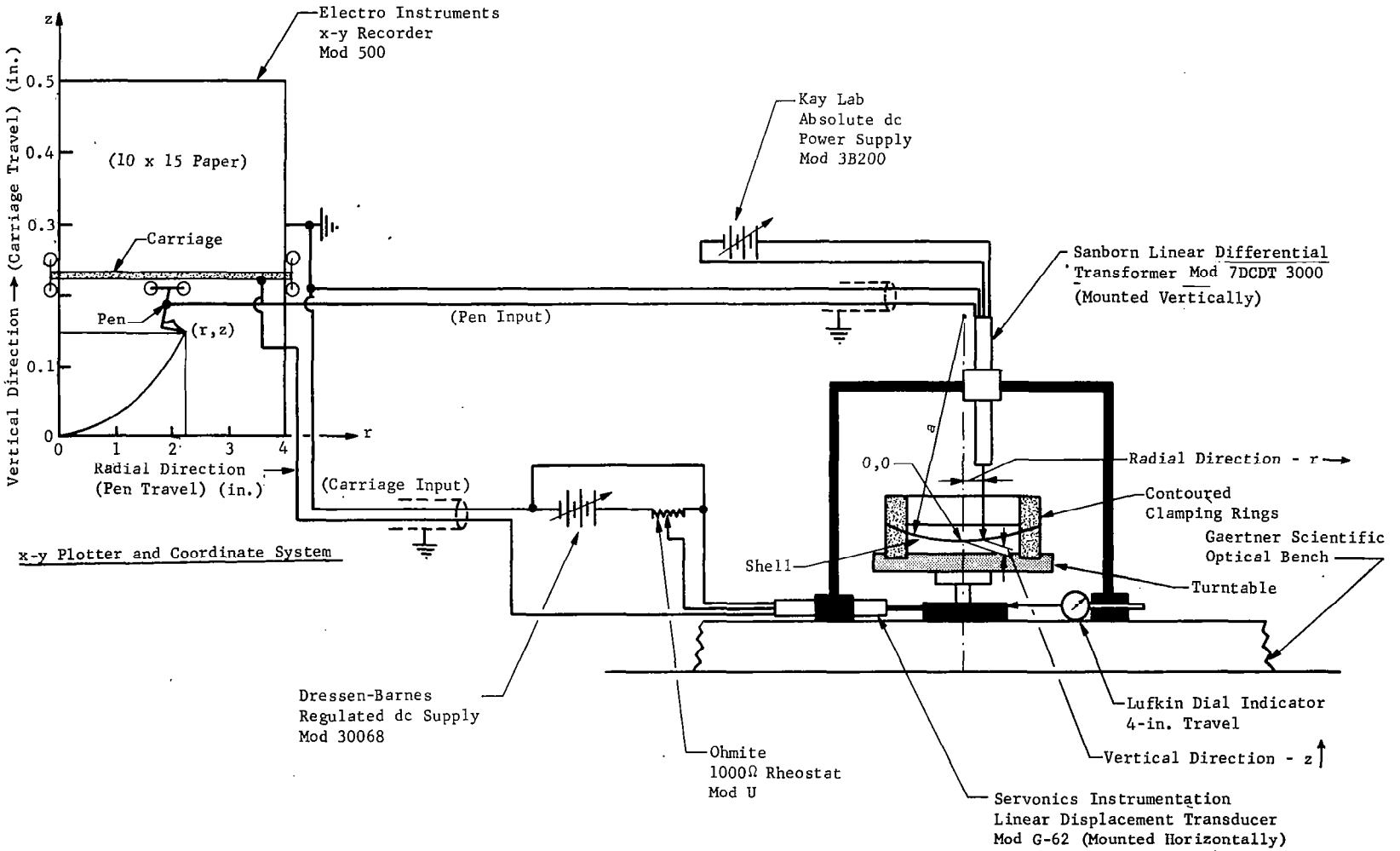


Fig. 3 Schematic of Geometry-Measuring Device

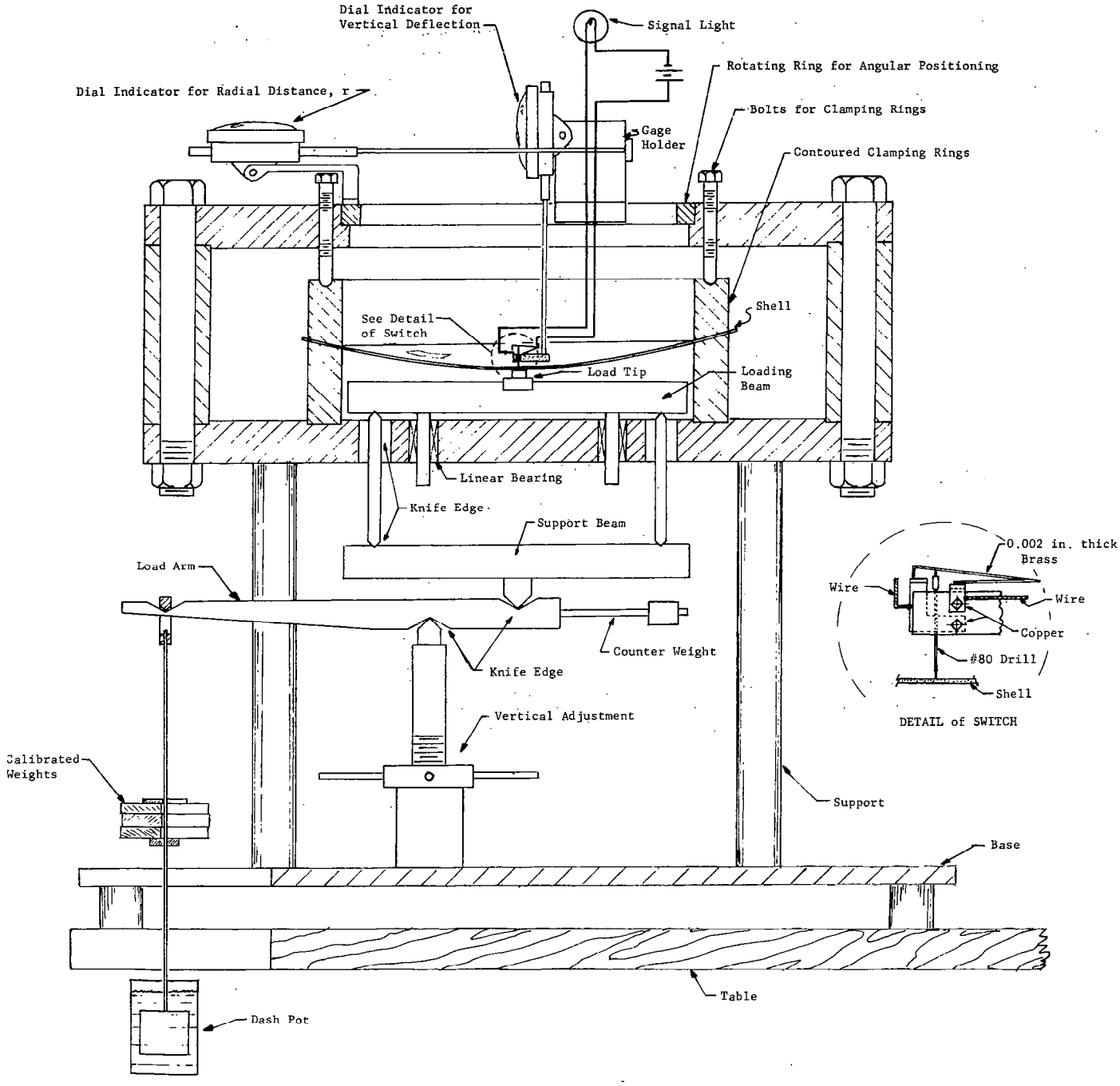


Fig. 4 Schematic of Tester, Loading Device, and Deflection Measuring Device

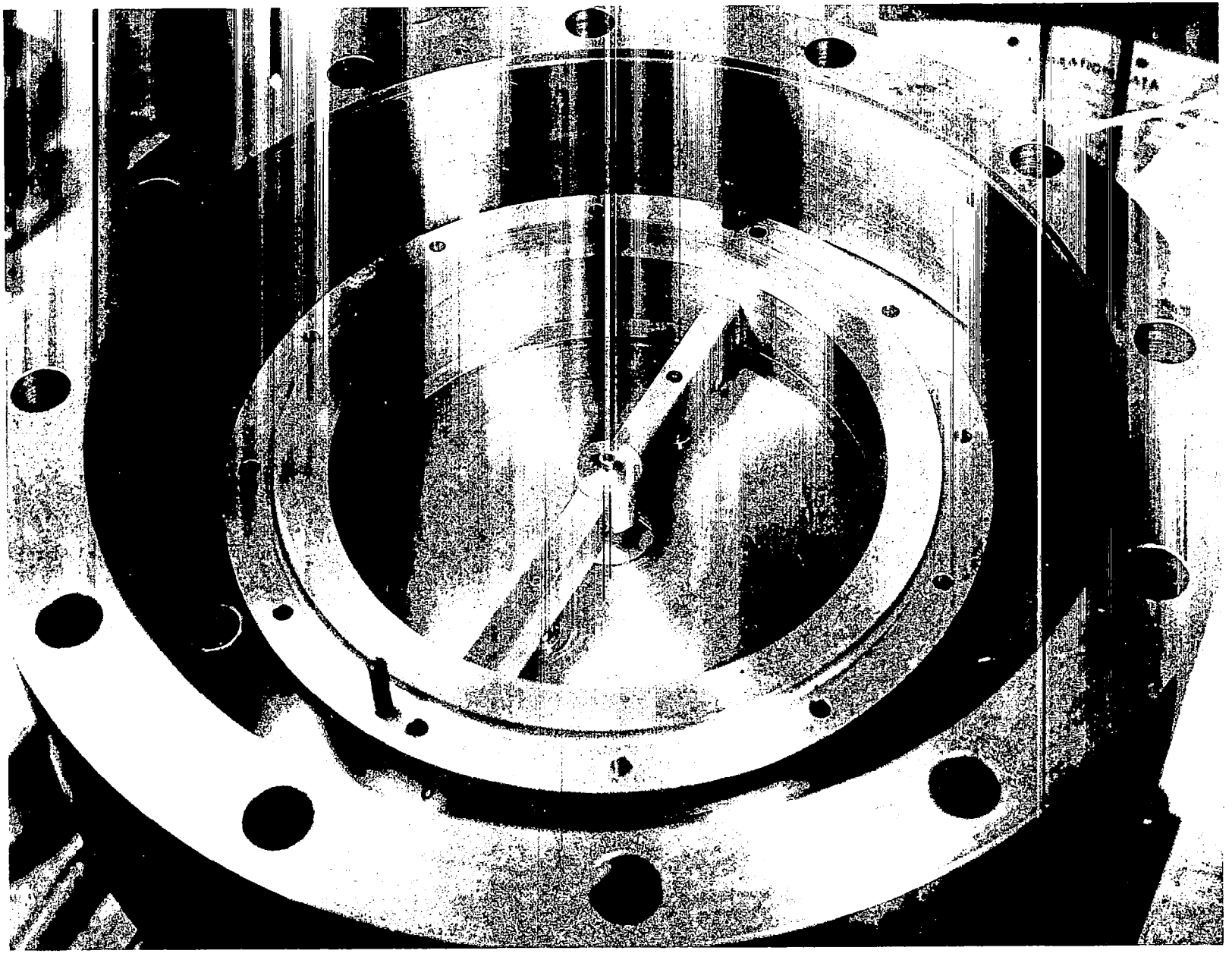


Fig. 5 Interior of Tester

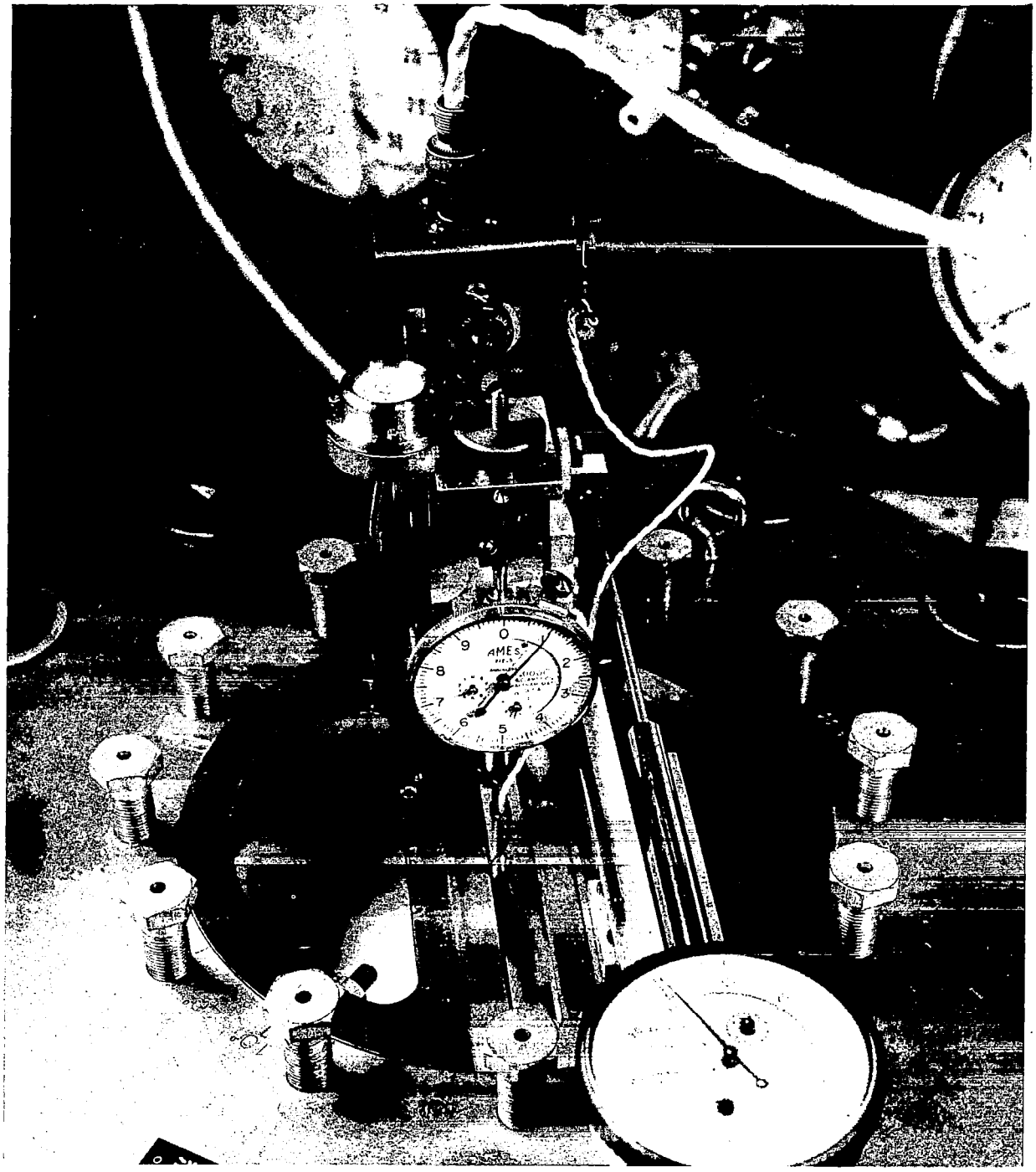


Fig. 6 Deflection Measuring Device

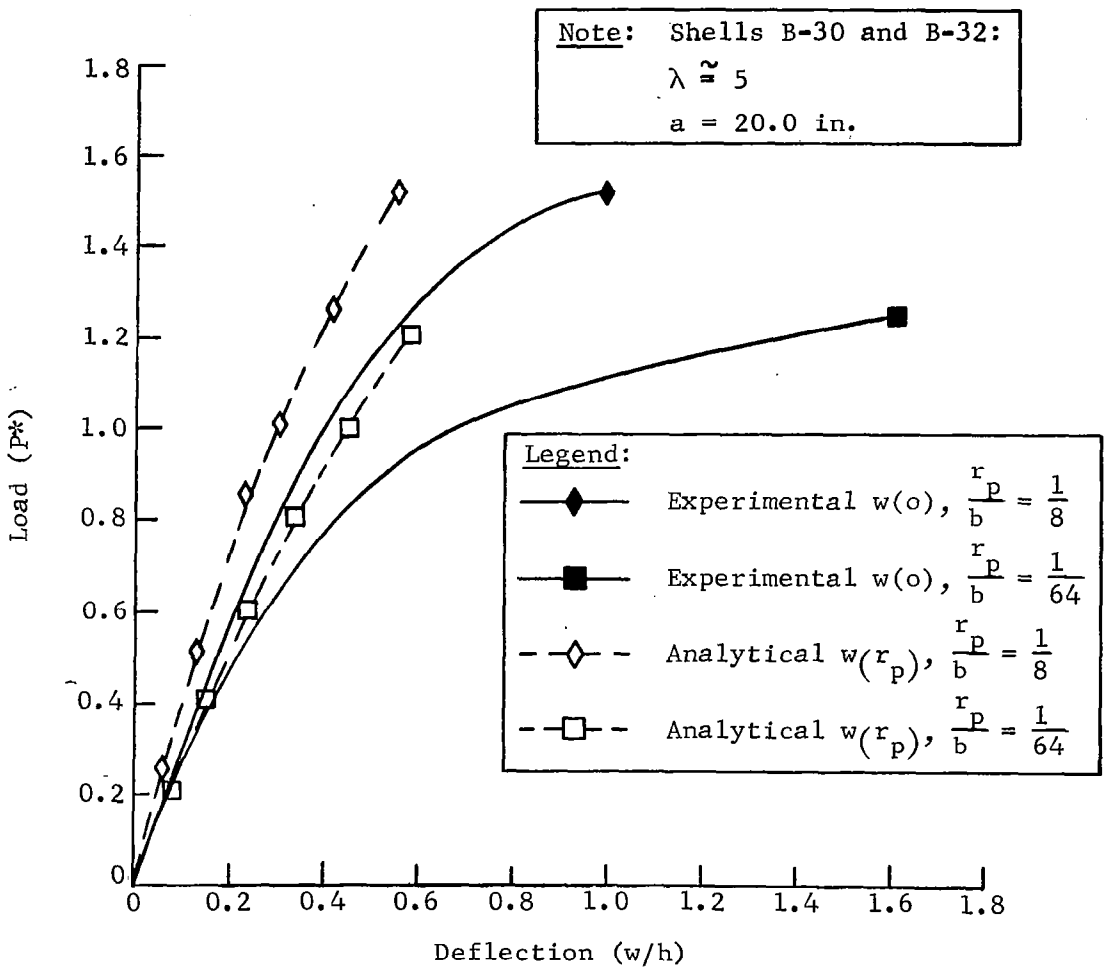


Fig. 7 Comparison of Theory and Experiment for Load-Deflection for Typical Tests, $\lambda \cong 5$

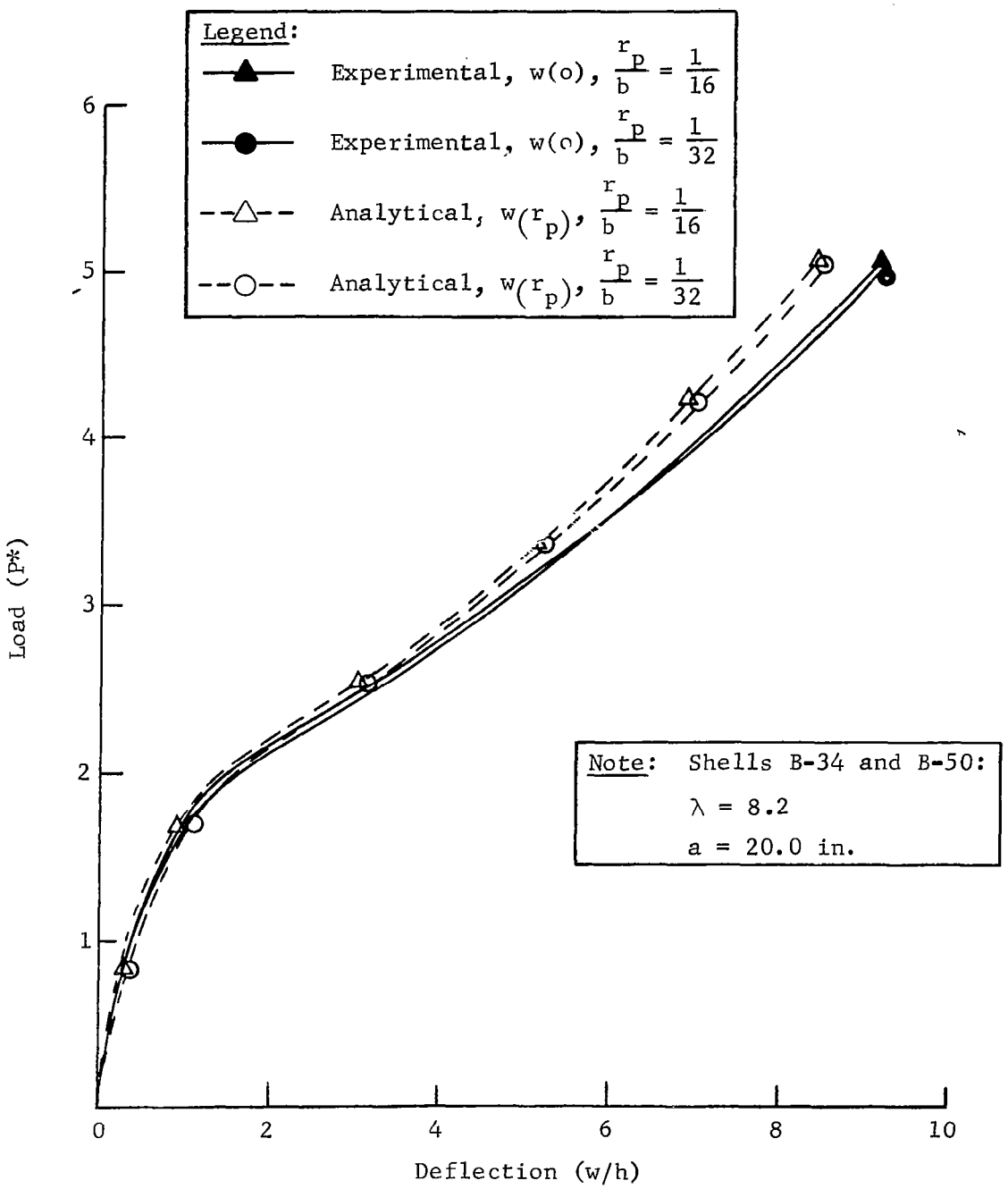


Fig. 8 Comparison of Theory and Experiment for Load-Deflection for Typical Tests, $\lambda = 8.2$

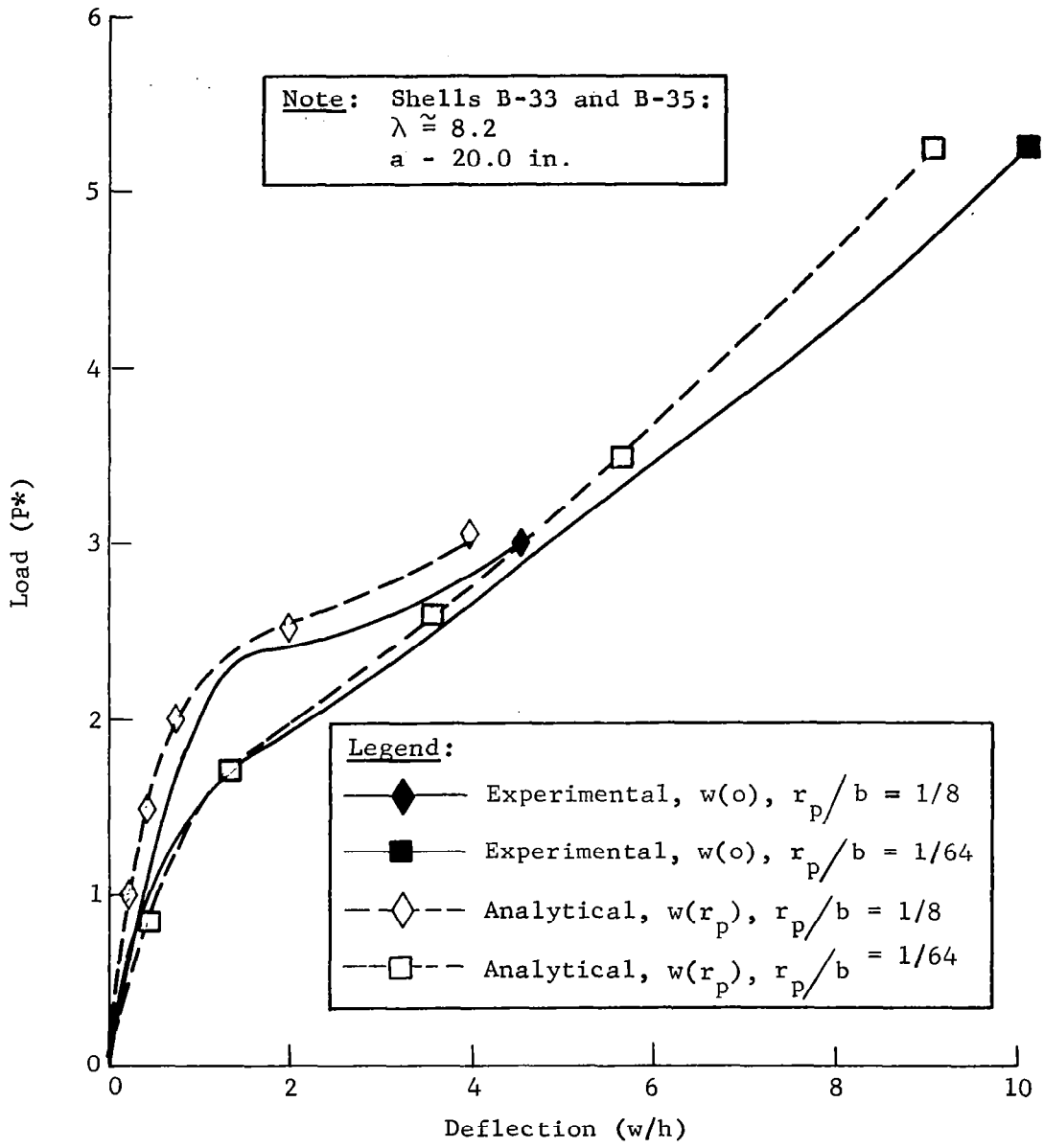


Fig. 9 Comparison of Theory and Experiment for Load-Deflection for Typical Tests, $\lambda \cong 8.2$

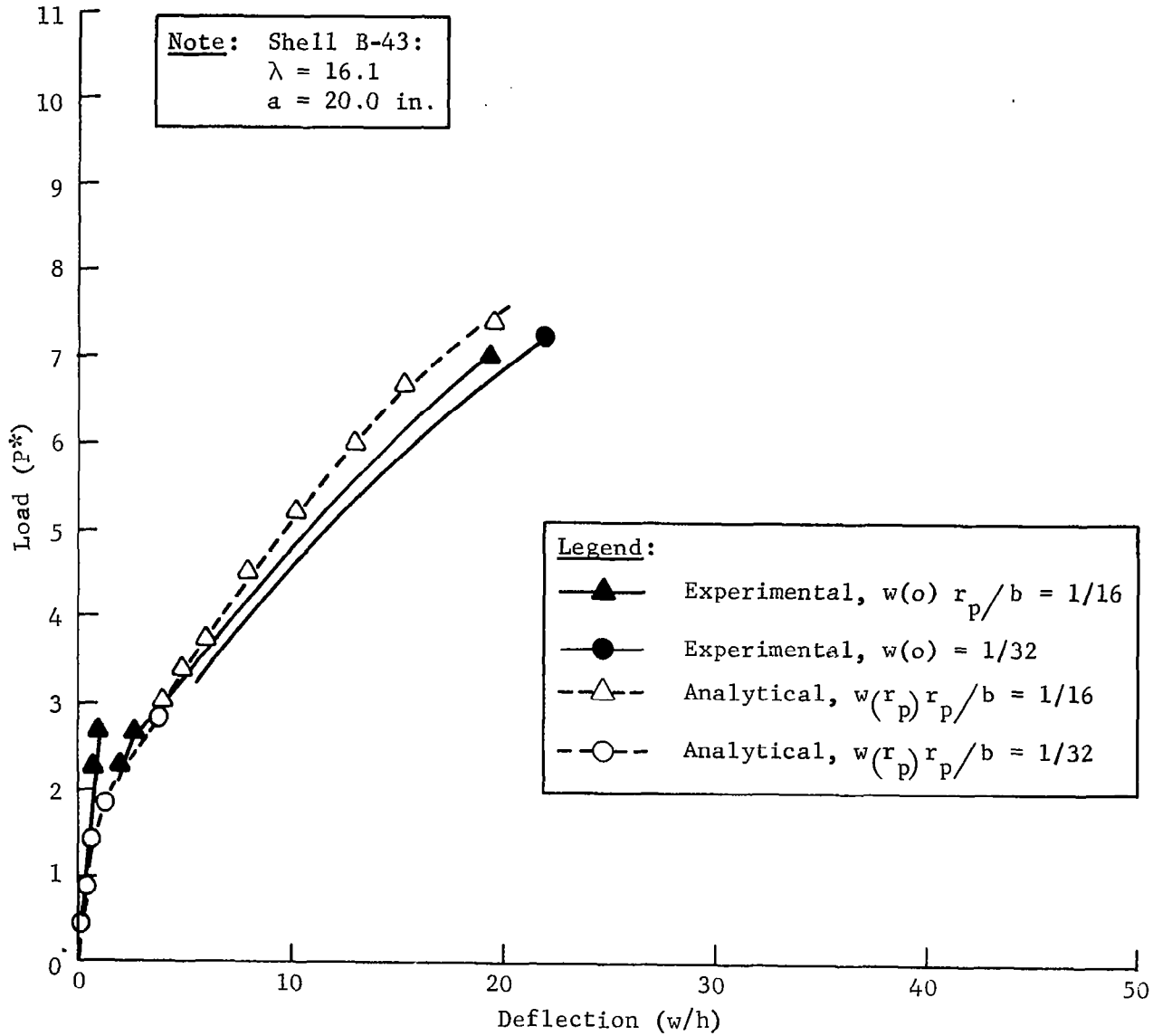


Fig. 10 Comparison of Theory and Experiment for Load-Deflection for Typical Tests, λ = 16.1

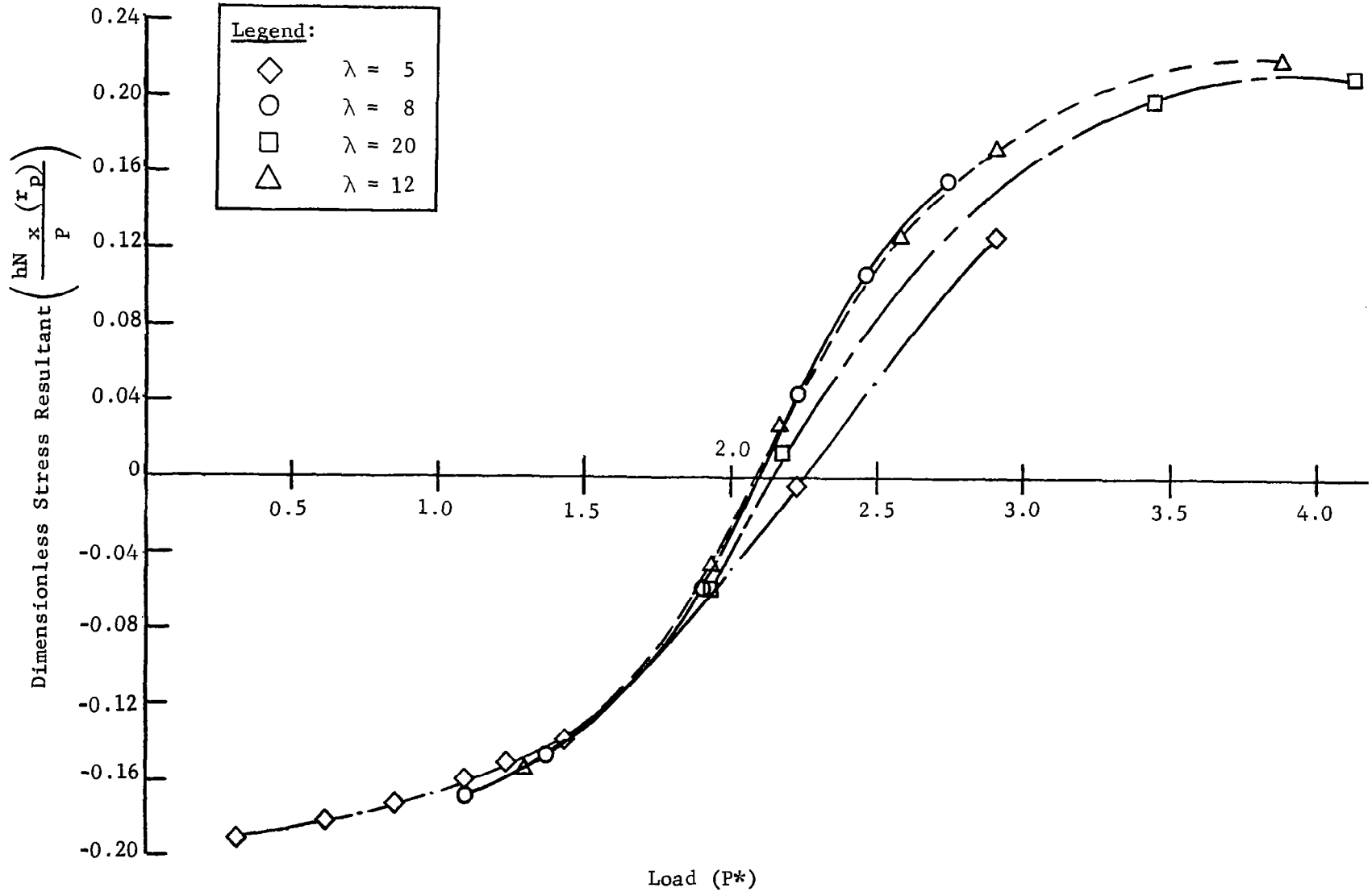


Fig. 11 Average Stress Resultant Under Load Area Changes Sign at Transition Load

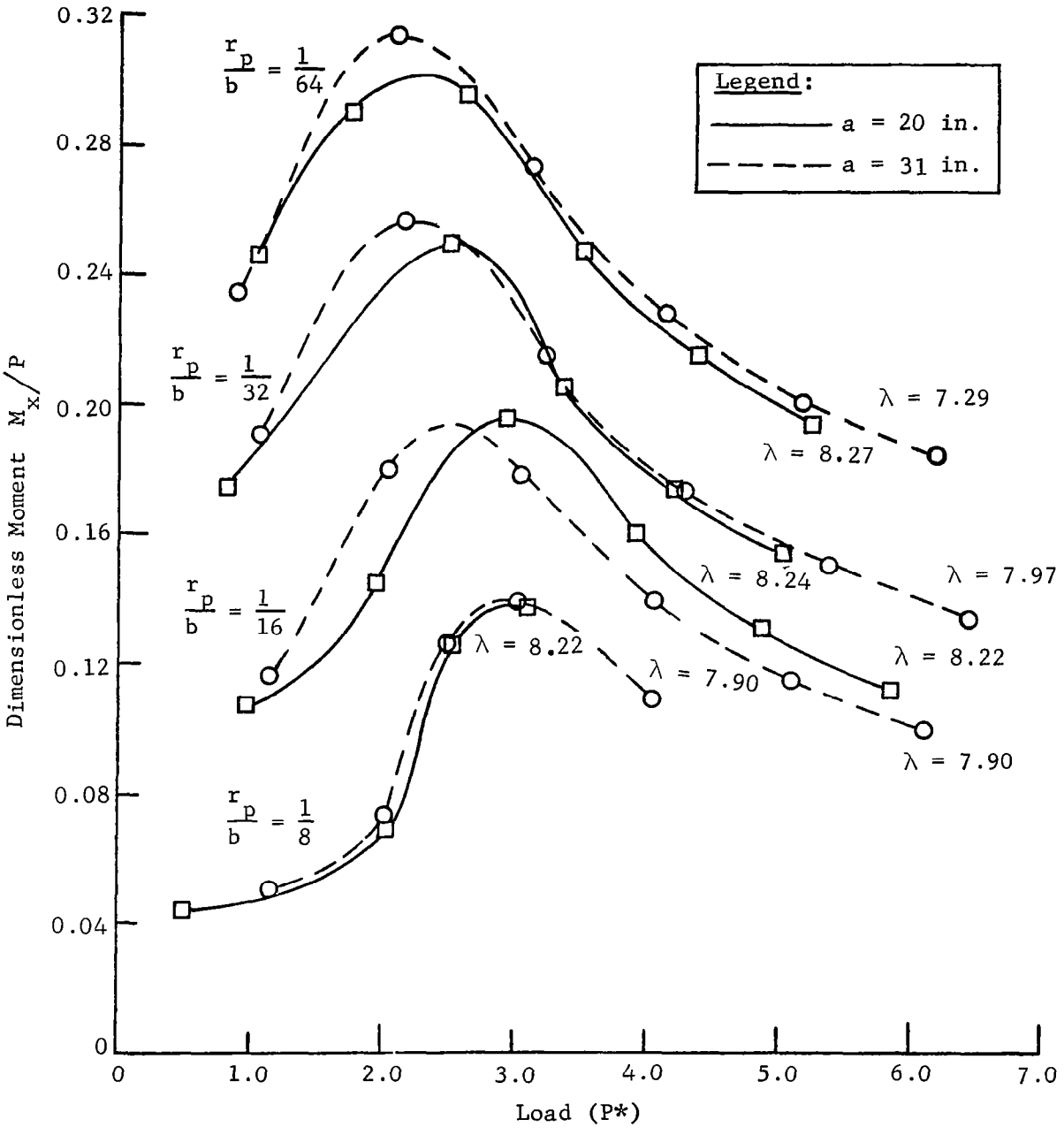


Fig. 12 Effect of Load Area on Maximum Bending Moment for λ = 8

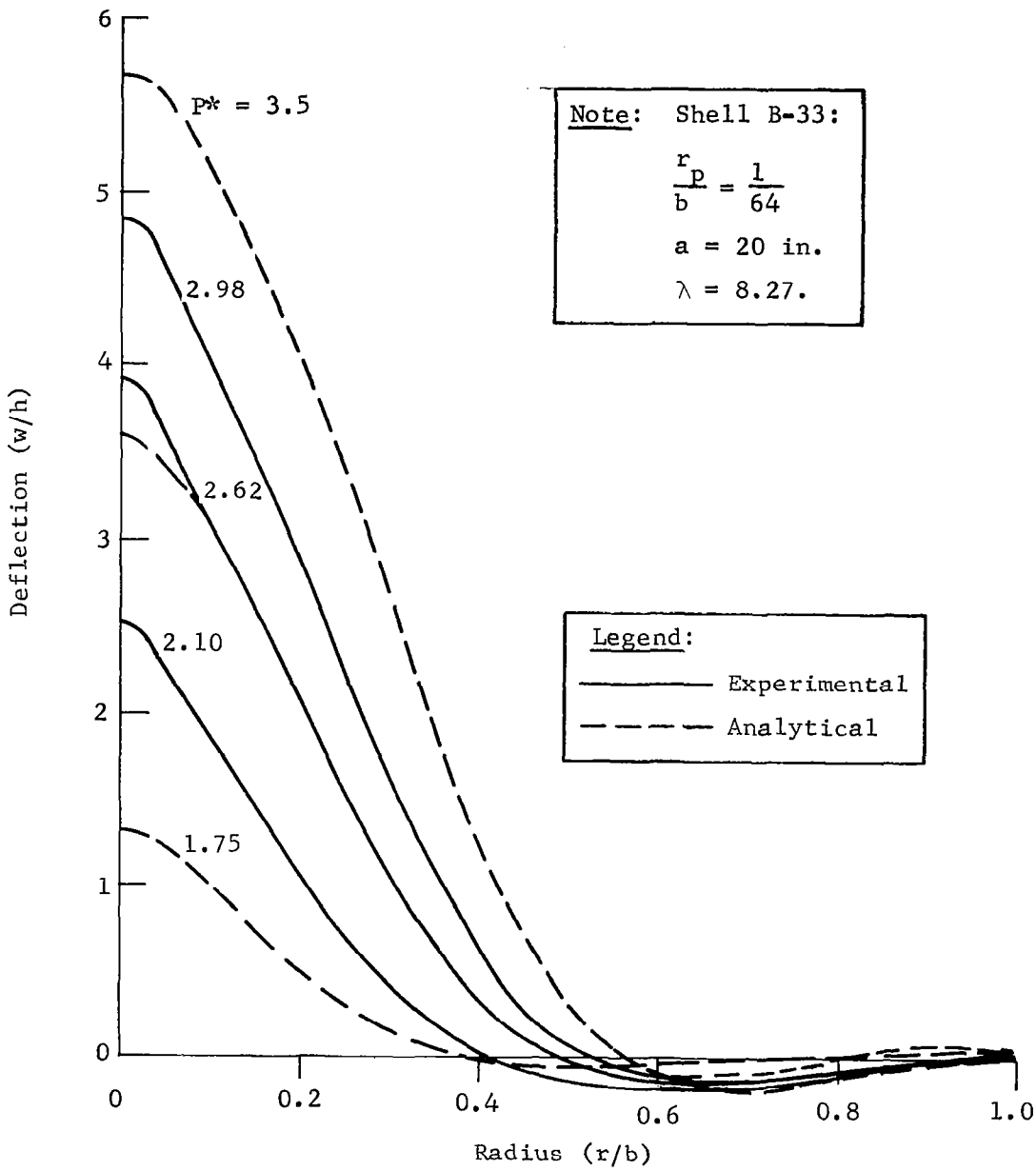


Fig. 13 Theory and Experiment Exhibit Dimpled Deflection Mode Shape for a Typical Shell

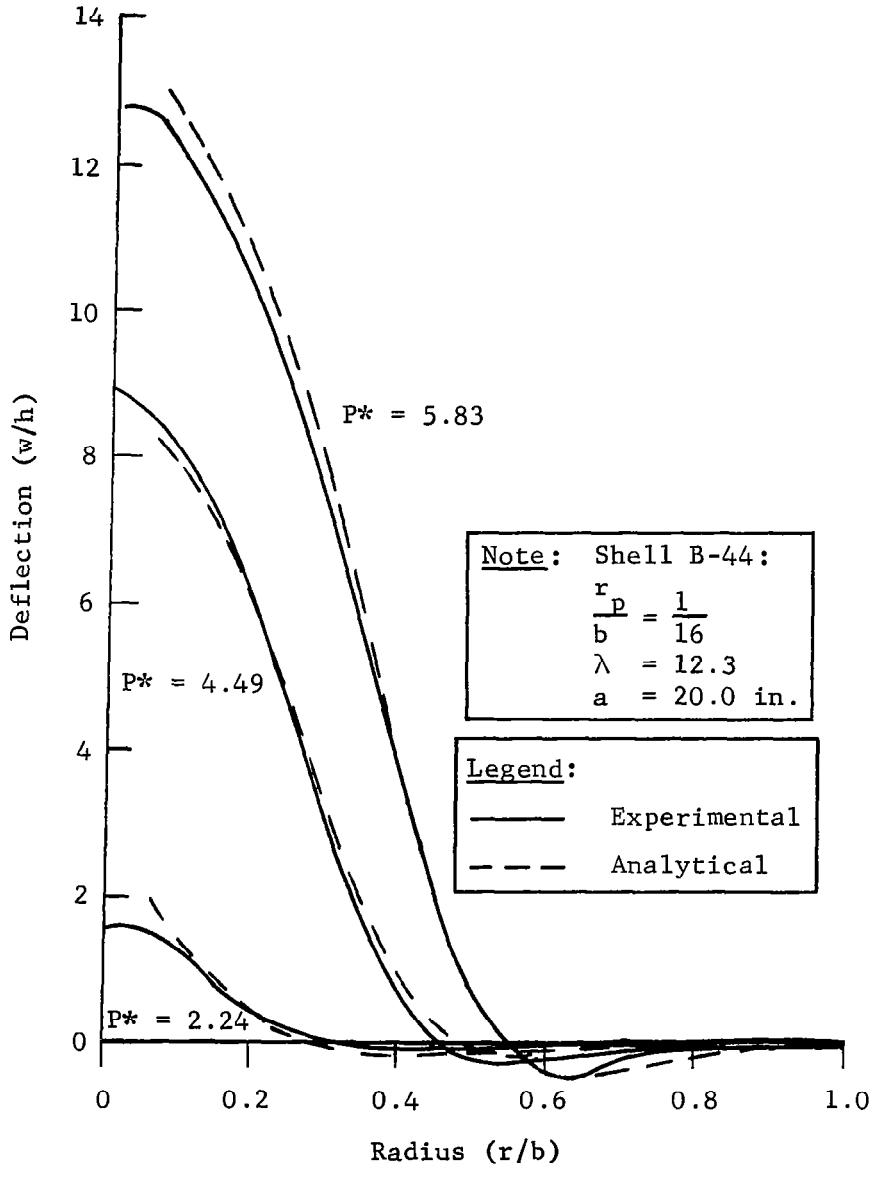


Fig. 14 Theory and Experiment Exhibit Dimpled Deflection Mode Shape for a Typical Shell

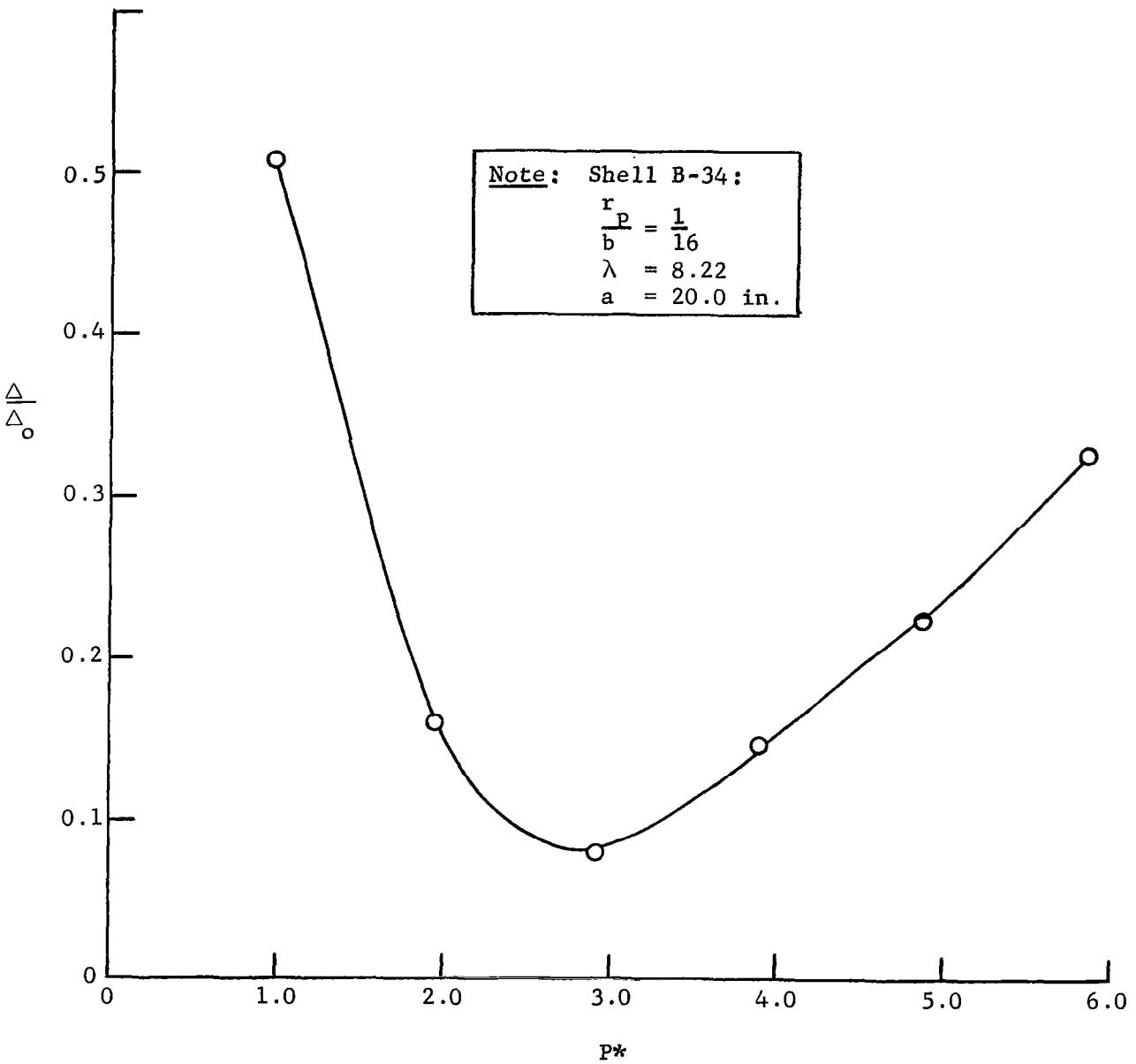


Fig. 15 Determinant from Numerical Solution Reaches Minimum at Transition Load

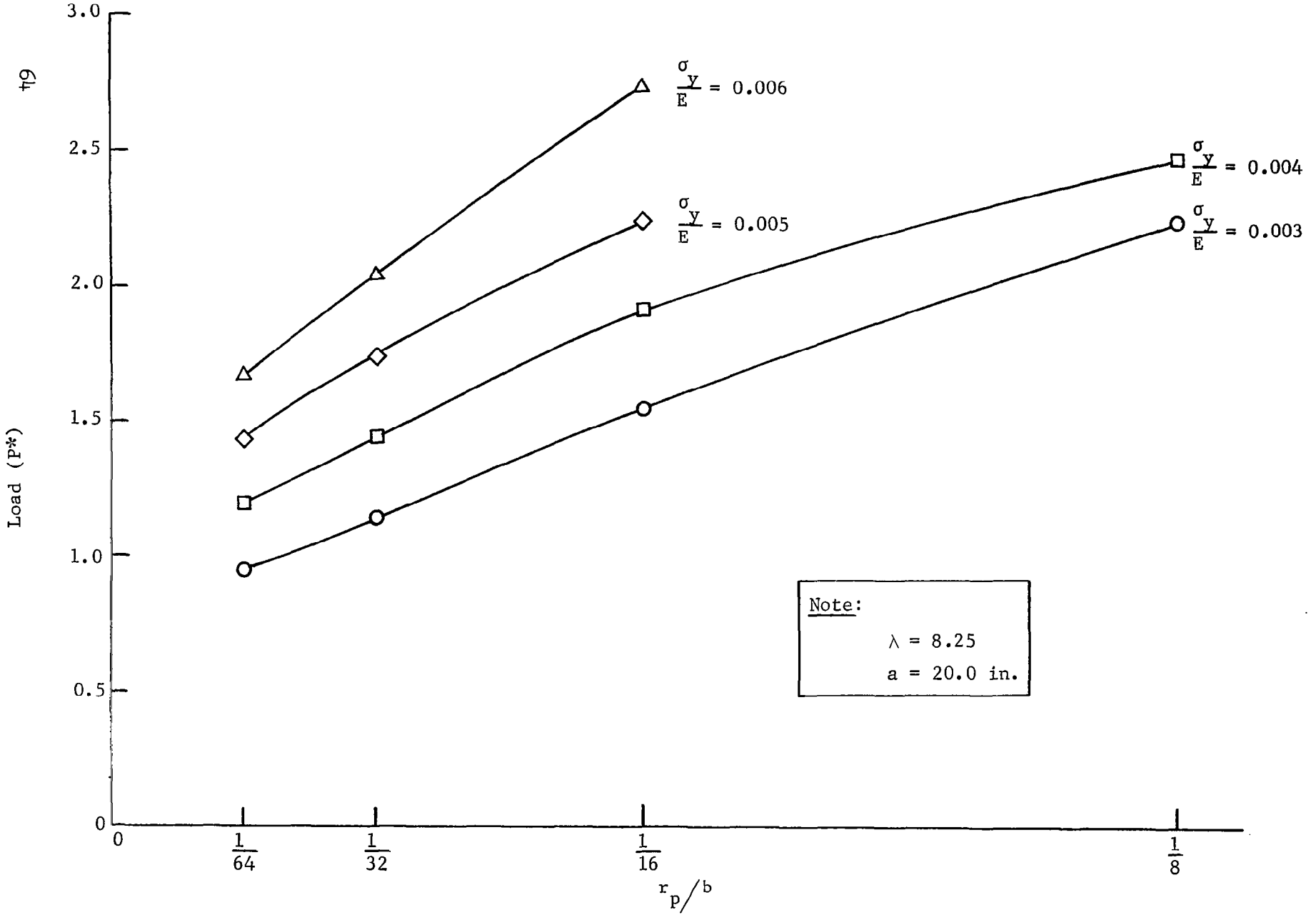


Fig. 16 Load At Which Surface Stress Reaches Yield Stress

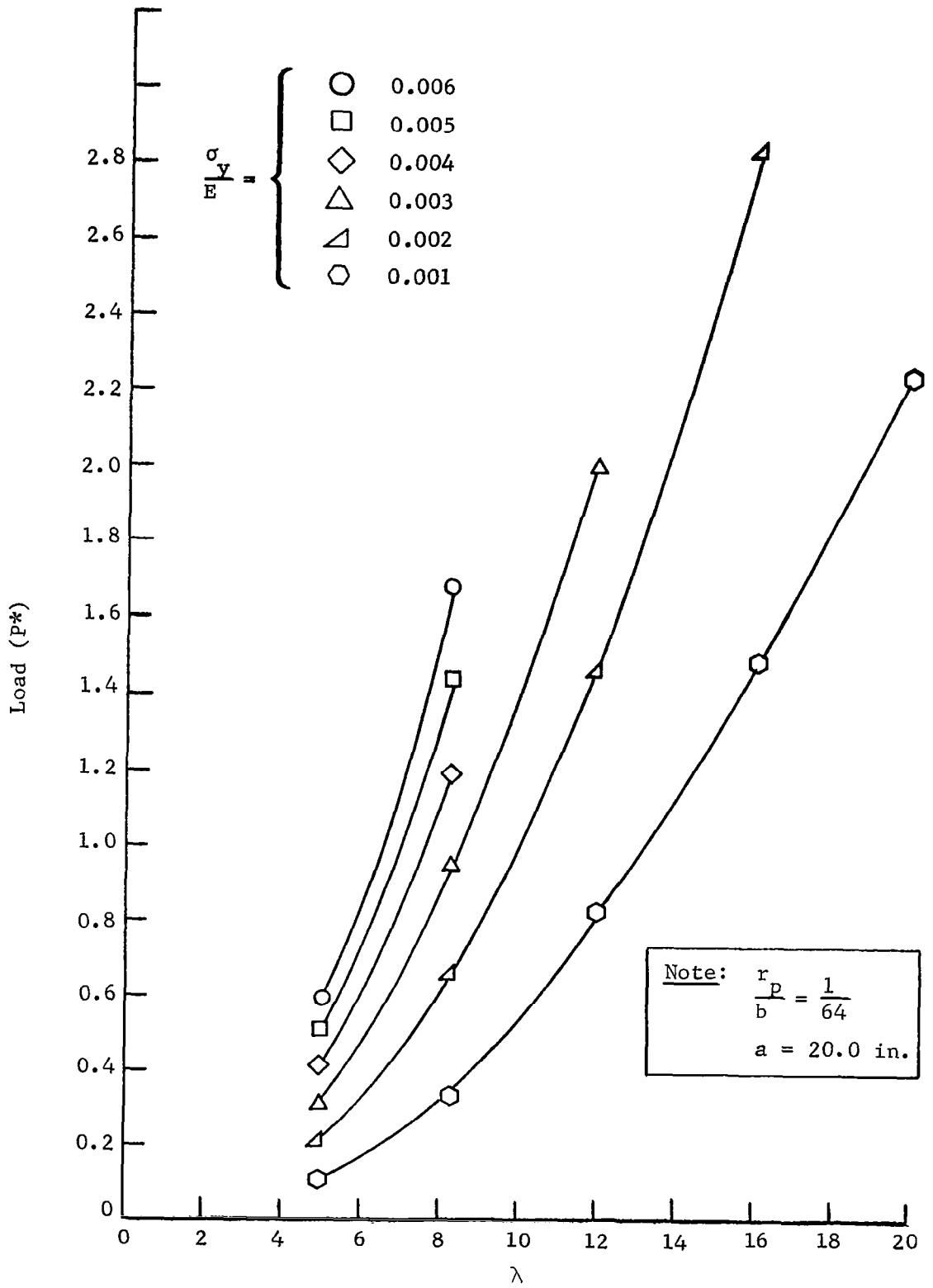


Fig. 17 Effect of Load Area on Yield Stress

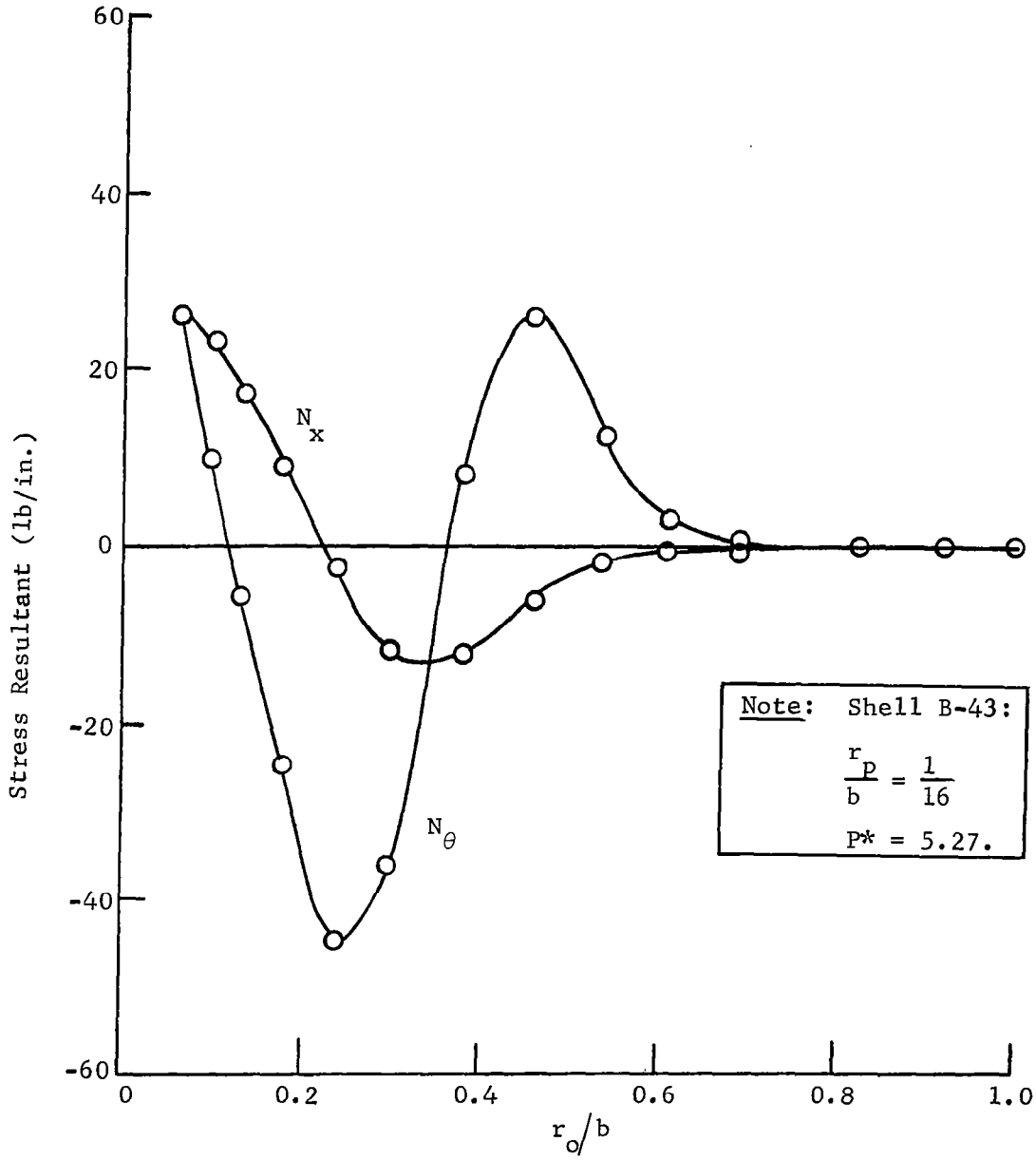


Fig. 18 Computed Mid-Surface Stress Resultants at a Load that Provided Asymmetric Buckling in Experimental Shell

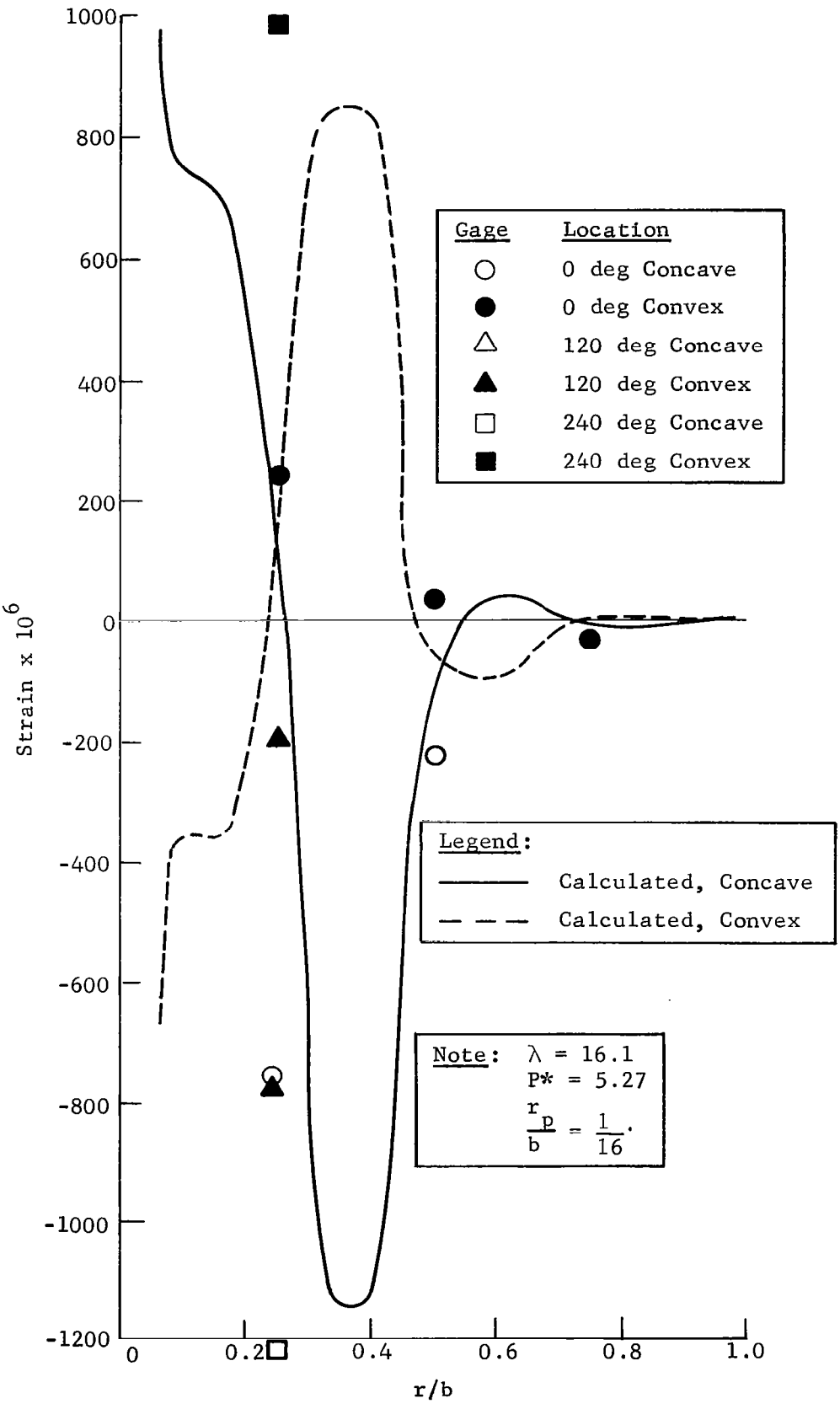


Fig. 19 Meridional Surface Strains Compared to Experiment

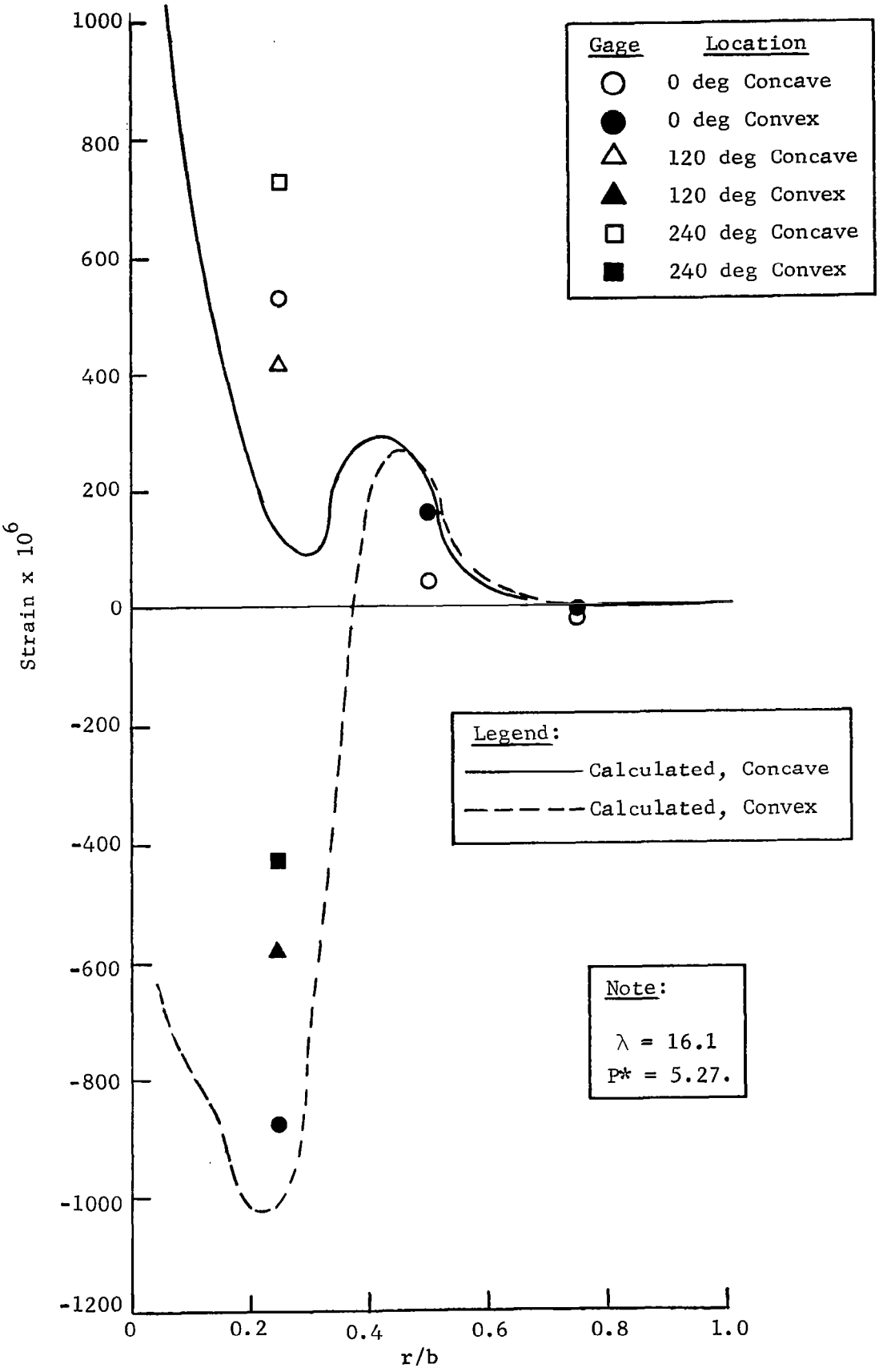


Fig. 20 Circumferential Surface Strains Compared to Experiment

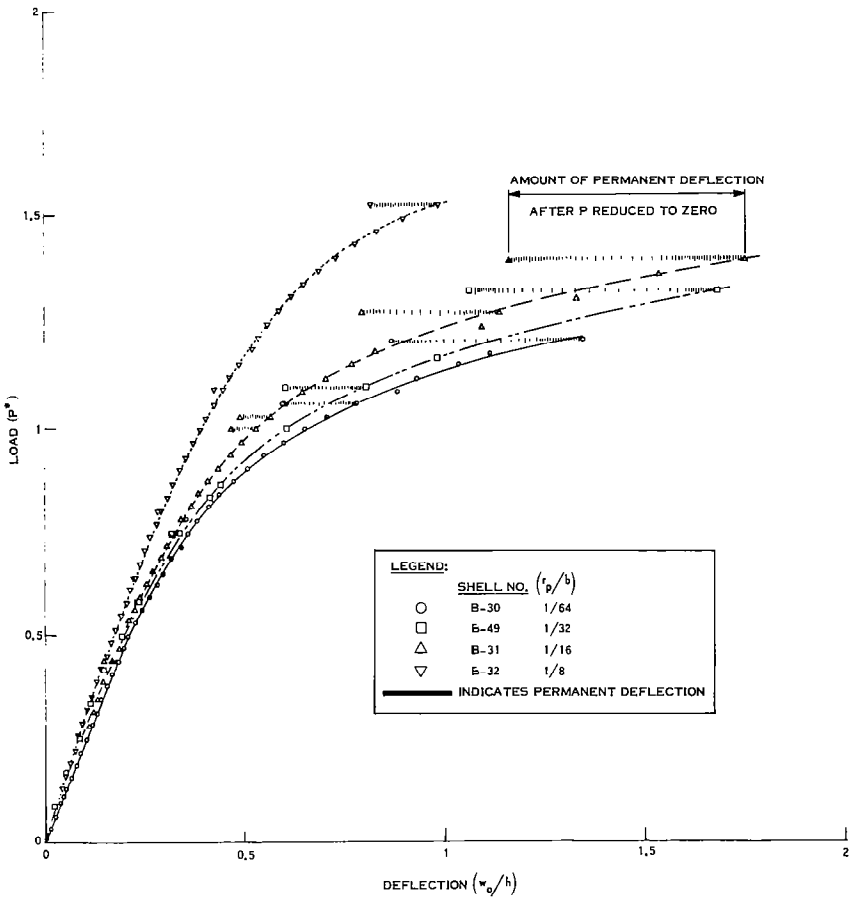


FIG. 21 EXPERIMENTAL LOAD-CENTER DEFLECTION, FOUR LOAD AREAS, $\lambda = 4.9$, $a = 20.0$ IN.

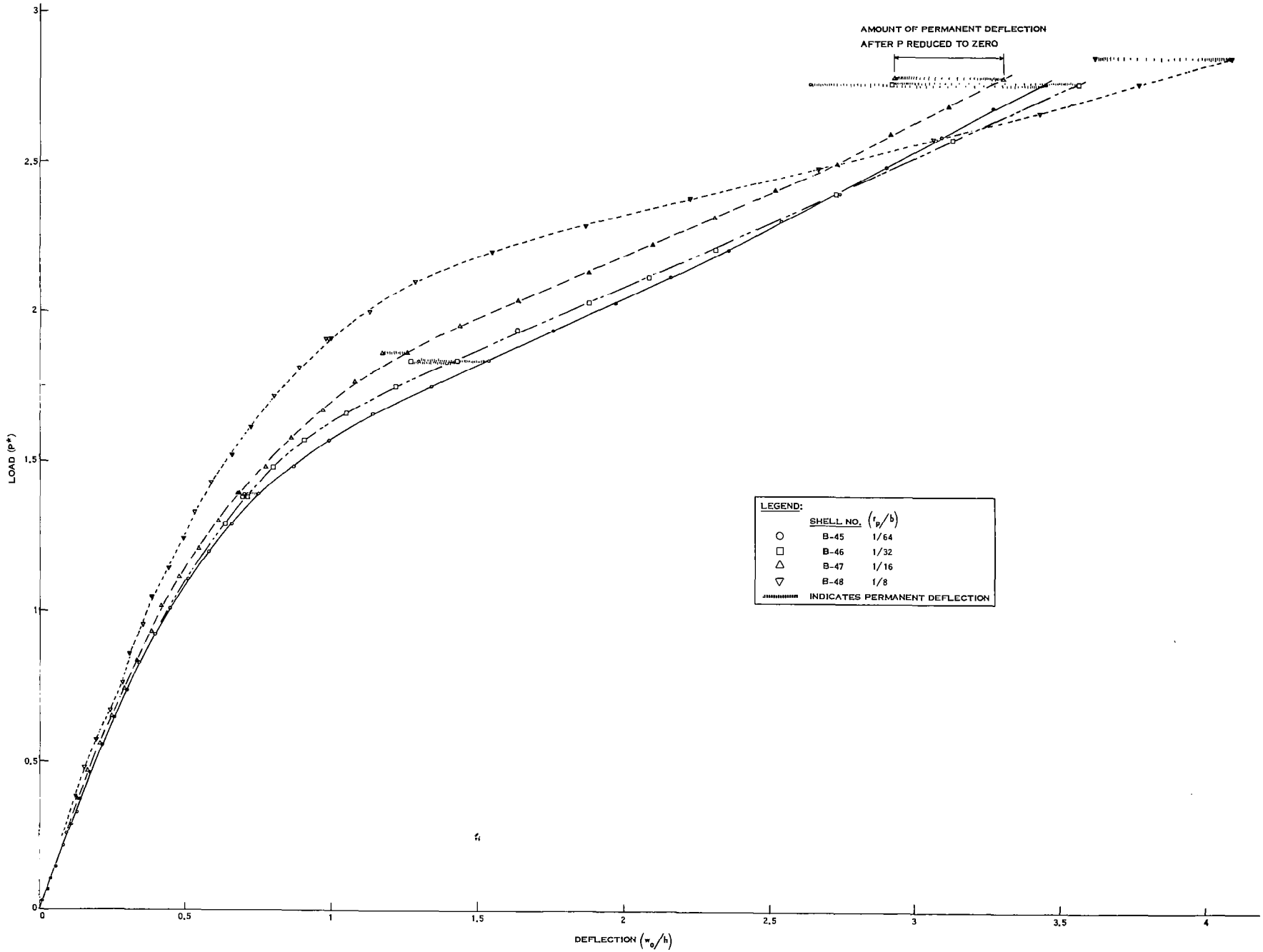


FIG. 22 EXPERIMENTAL LOAD-CENTER DEFLECTION, FOUR LOAD AREAS, $\lambda \cong 5$, $a \cong 30$ IN.

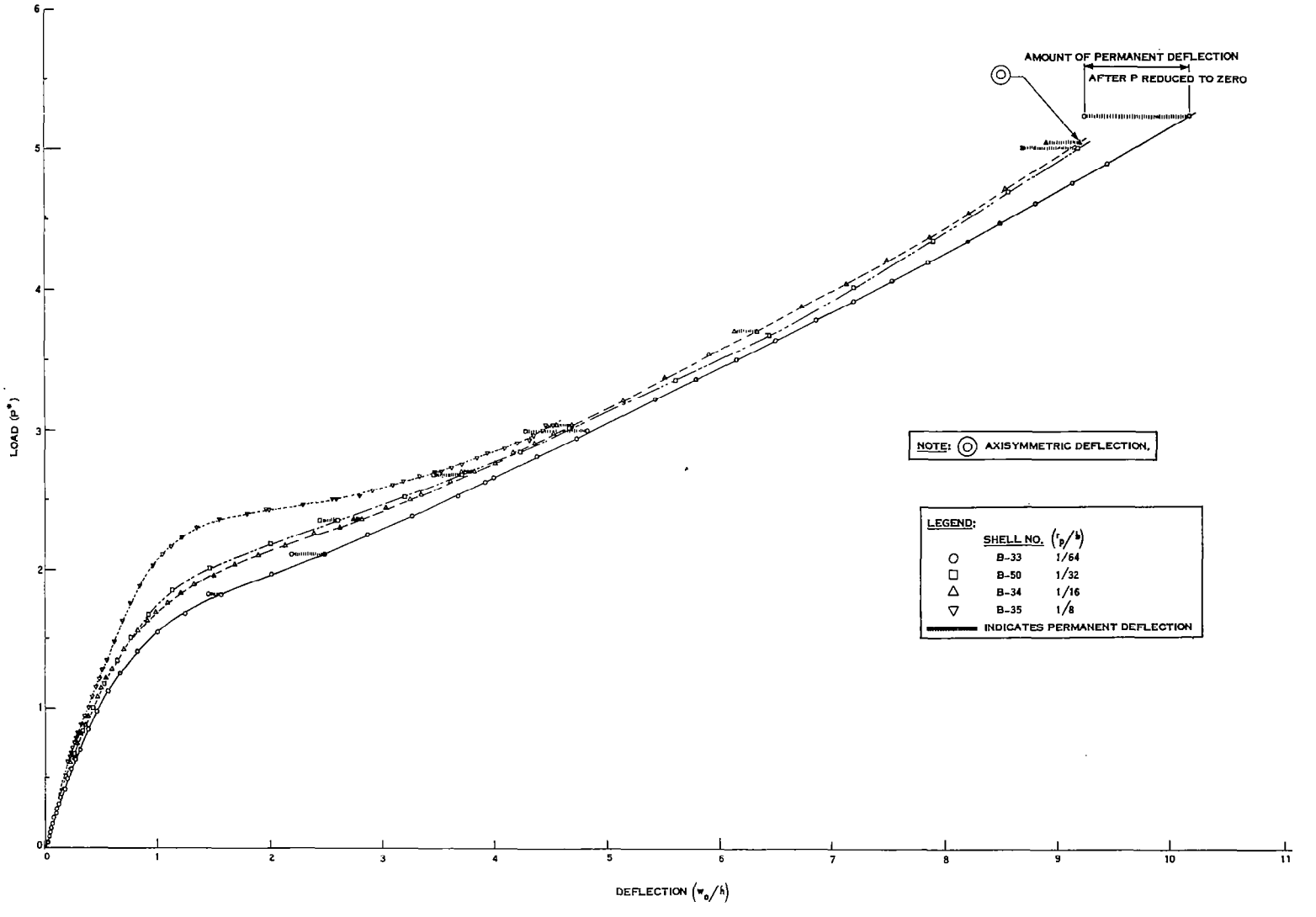
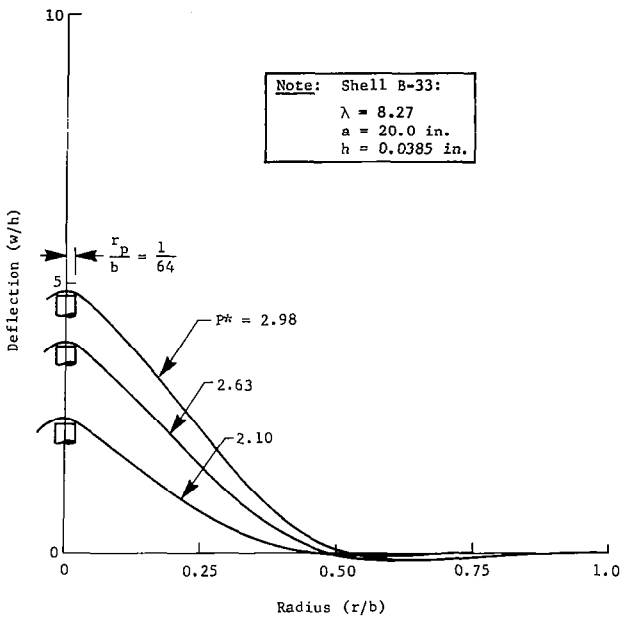
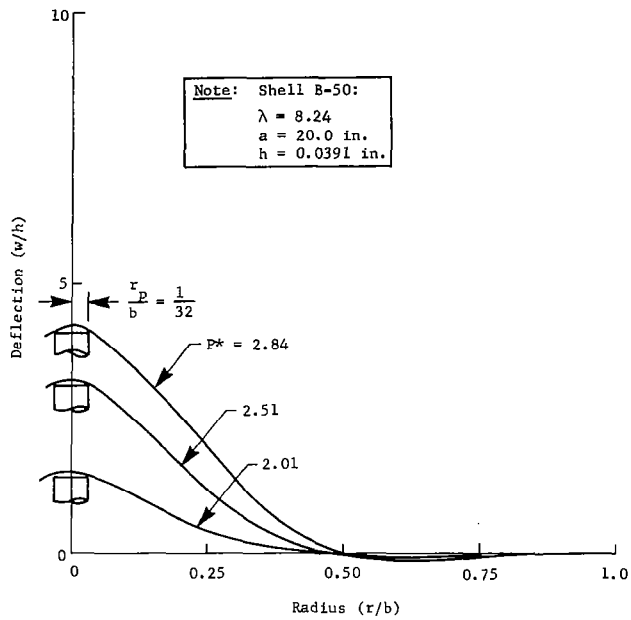
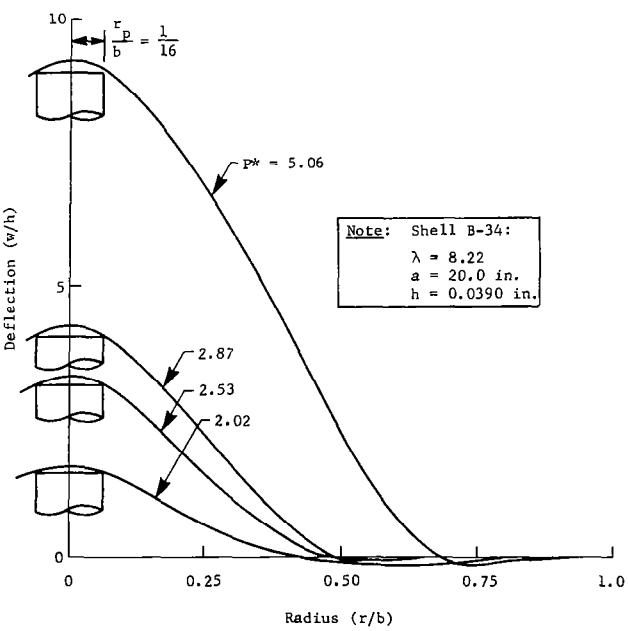


FIG. 23 EXPERIMENTAL LOAD-CENTER DEFLECTION, FOUR LOAD AREAS, $\lambda \cong 8.2$, $a = 20.0$ IN.







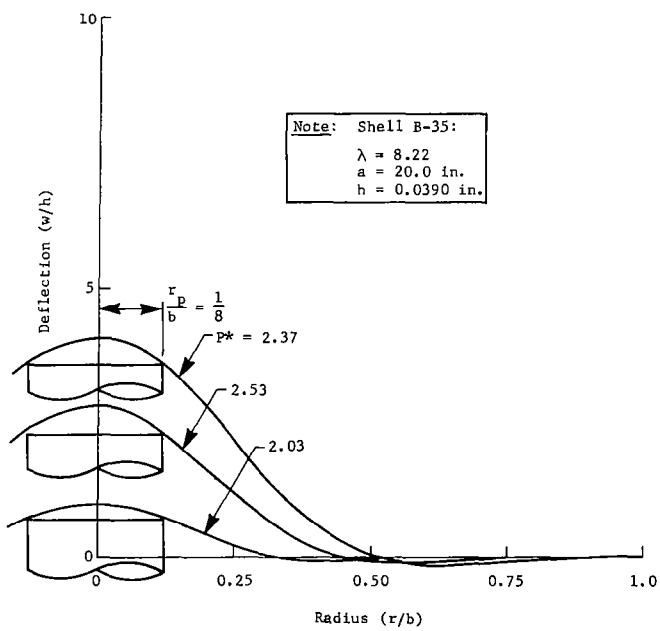


Fig. 24 Experimental Deflections on a Radial Line, $\lambda \cong 8.2$, $a = 20.0$ in.

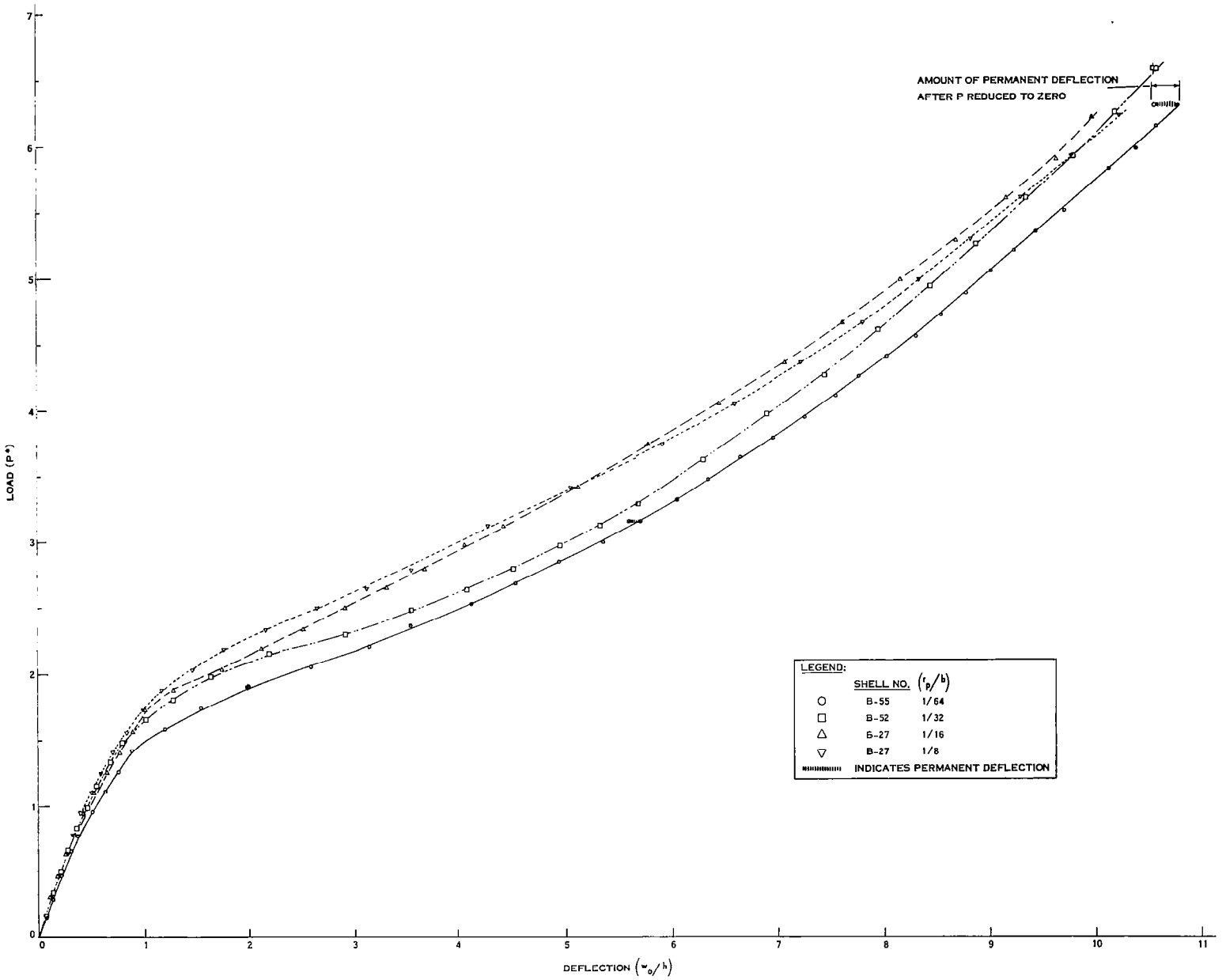


FIG. 25 EXPERIMENTAL LOAD-CENTER DEFLECTION, FOUR LOAD AREAS, $\lambda \cong 8$, $a = 31.0$ IN.

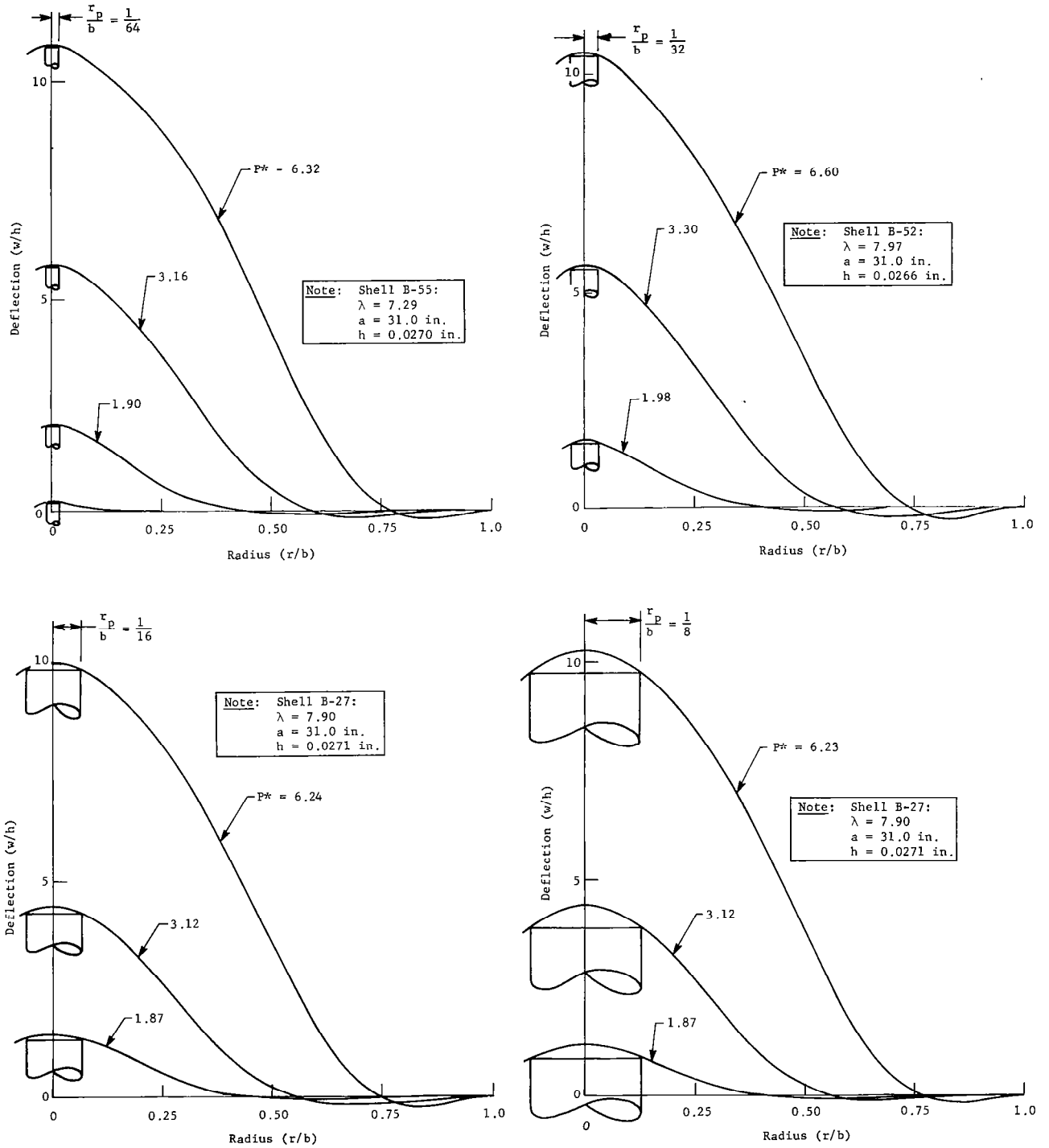
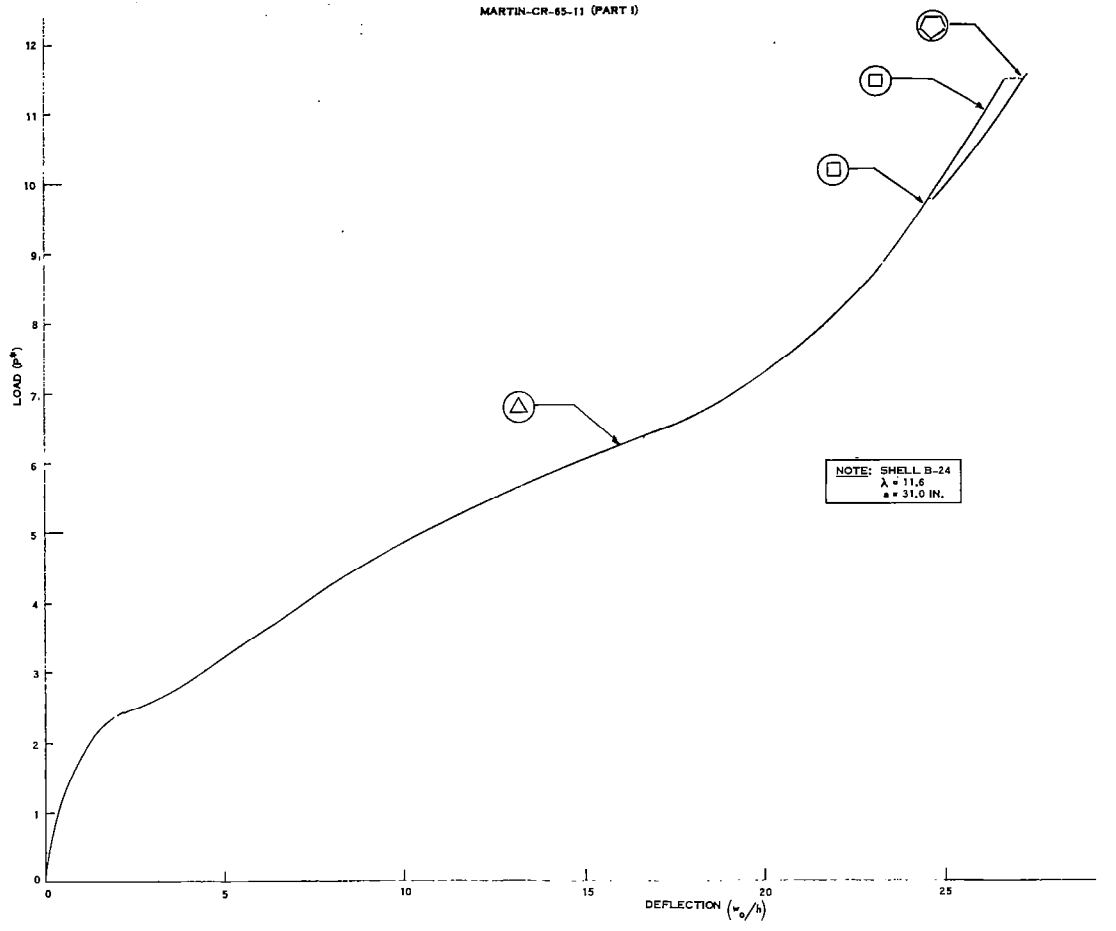


Fig. 26 Experimental Deflections on a Radial Line, $\lambda \cong 8$, a = 31.0 in.



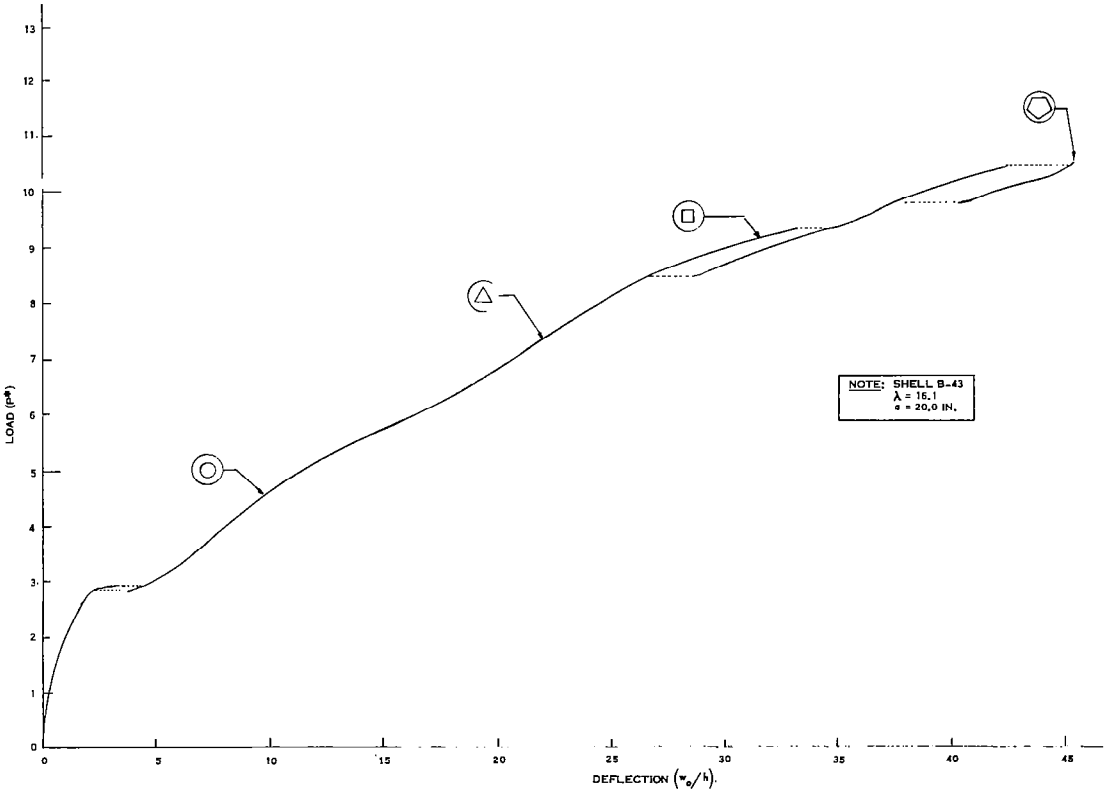
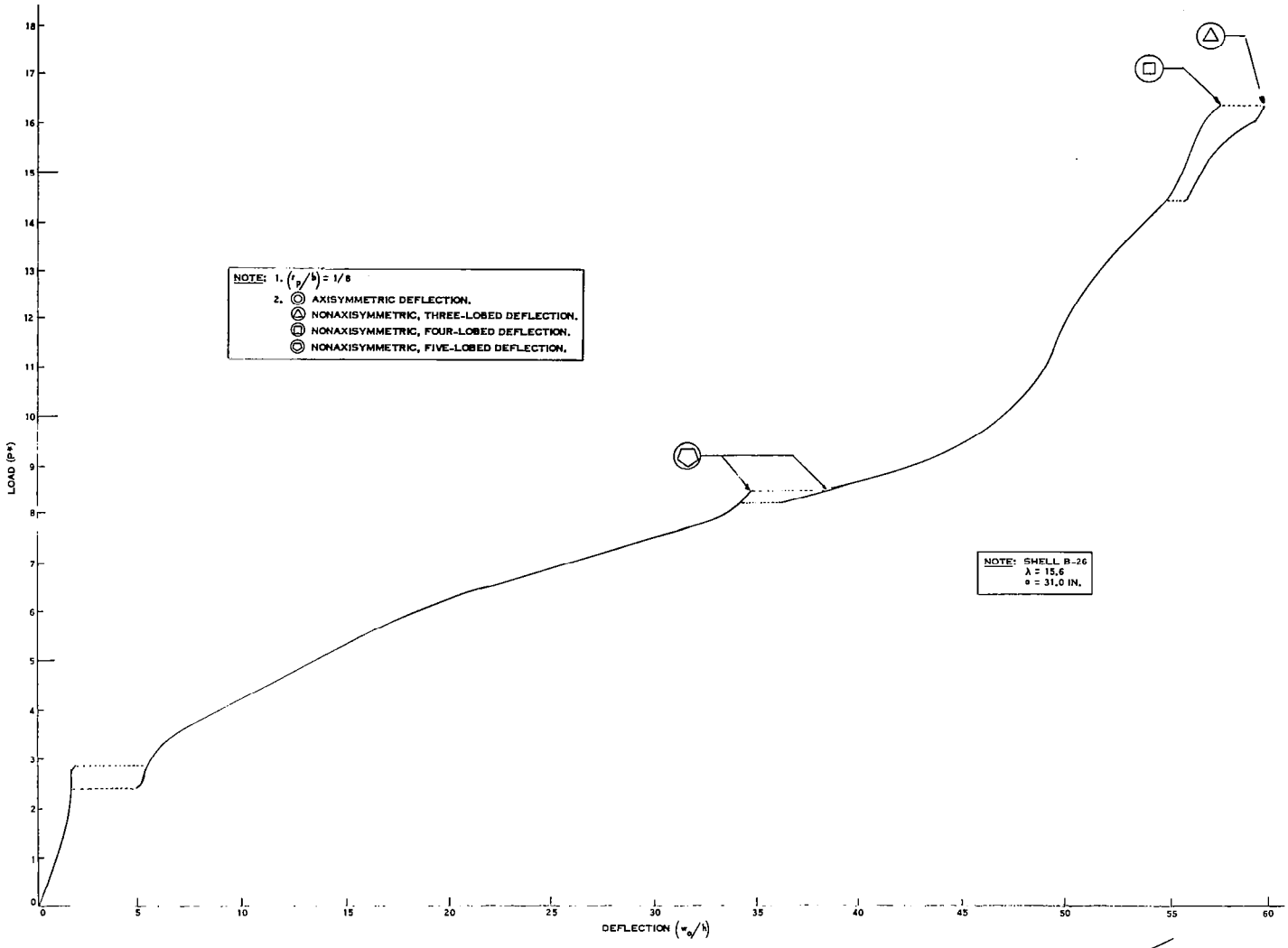


FIG. 27 EXPERIMENTAL LOAD-CENTER DEFLECTION CURVES FOR FOUR SHELLS, λ = 11.6 TO 20.0


NOTE: 1. $(f_p/h) = 1/8$
2. AXISYMMETRIC DEFLECTION.
NONAXISYMMETRIC, THREE-LOBED DEFLECTION.
NONAXISYMMETRIC, FOUR-LOBED DEFLECTION.
NONAXISYMMETRIC, FIVE-LOBED DEFLECTION.
NOTE: SHELL B-26
λ = 15.6
a = 31.0 IN.
LOAD (P*)
DEFLECTION (w_o/h)

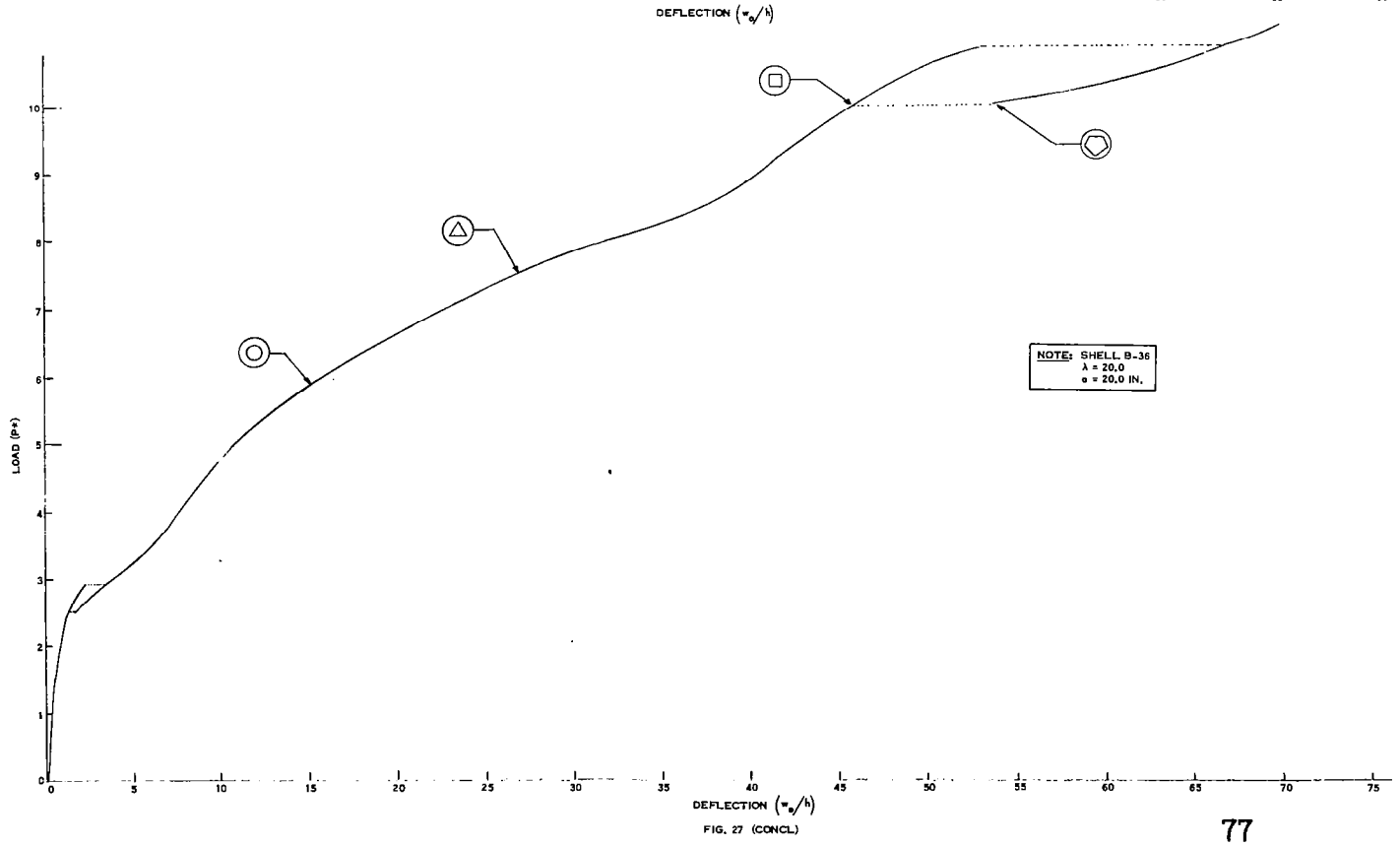

NOTE: SHELL B-36
λ = 20.0
a = 20.0 IN.
LOAD (P*)
DEFLECTION (w_o/h)

FIG. 27 (CONCL)

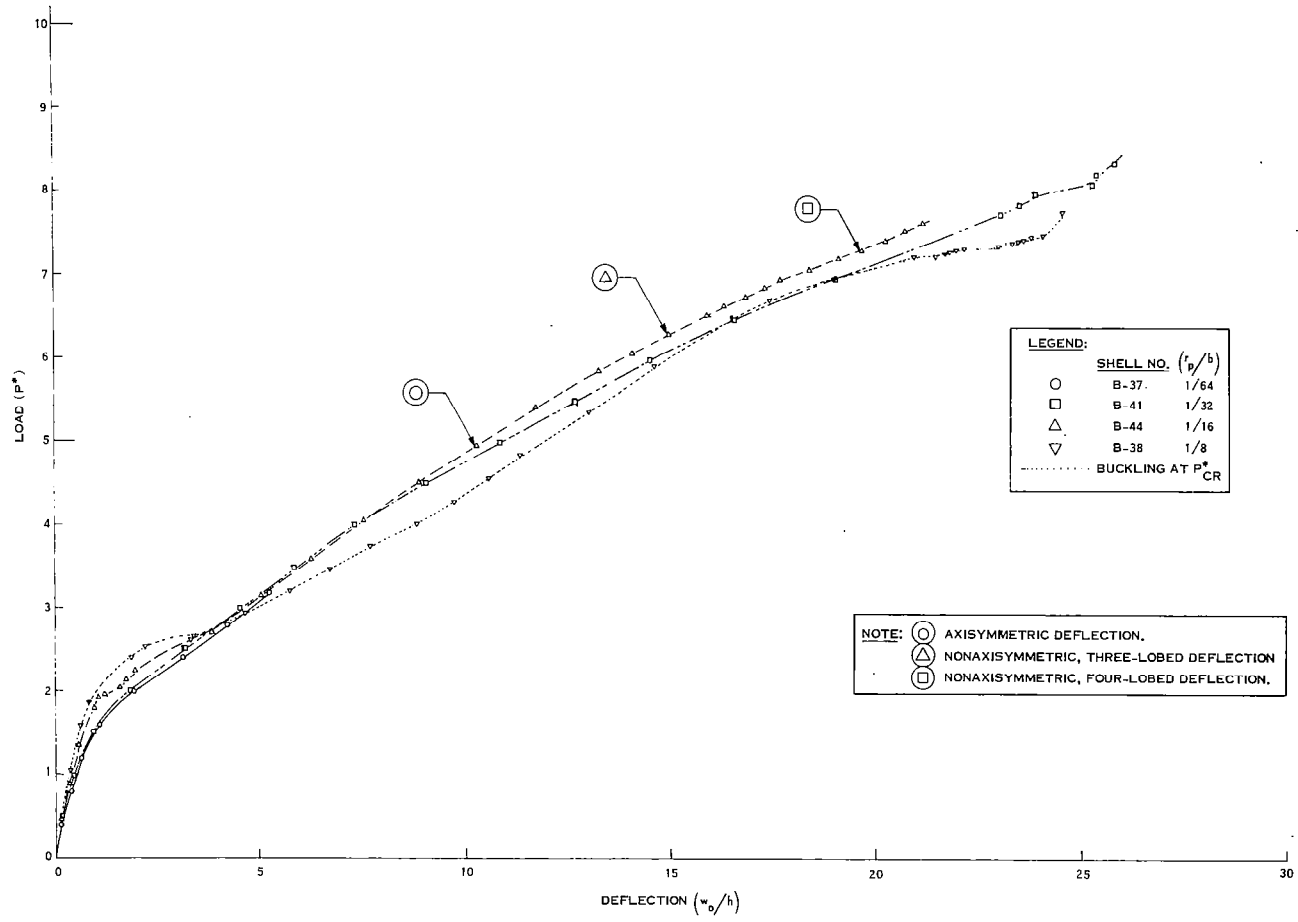


FIG. 28 EXPERIMENTAL LOAD-CENTER DEFLECTION FOUR LOAD AREAS, $\lambda \cong 12$, $a = 20.0$ IN.

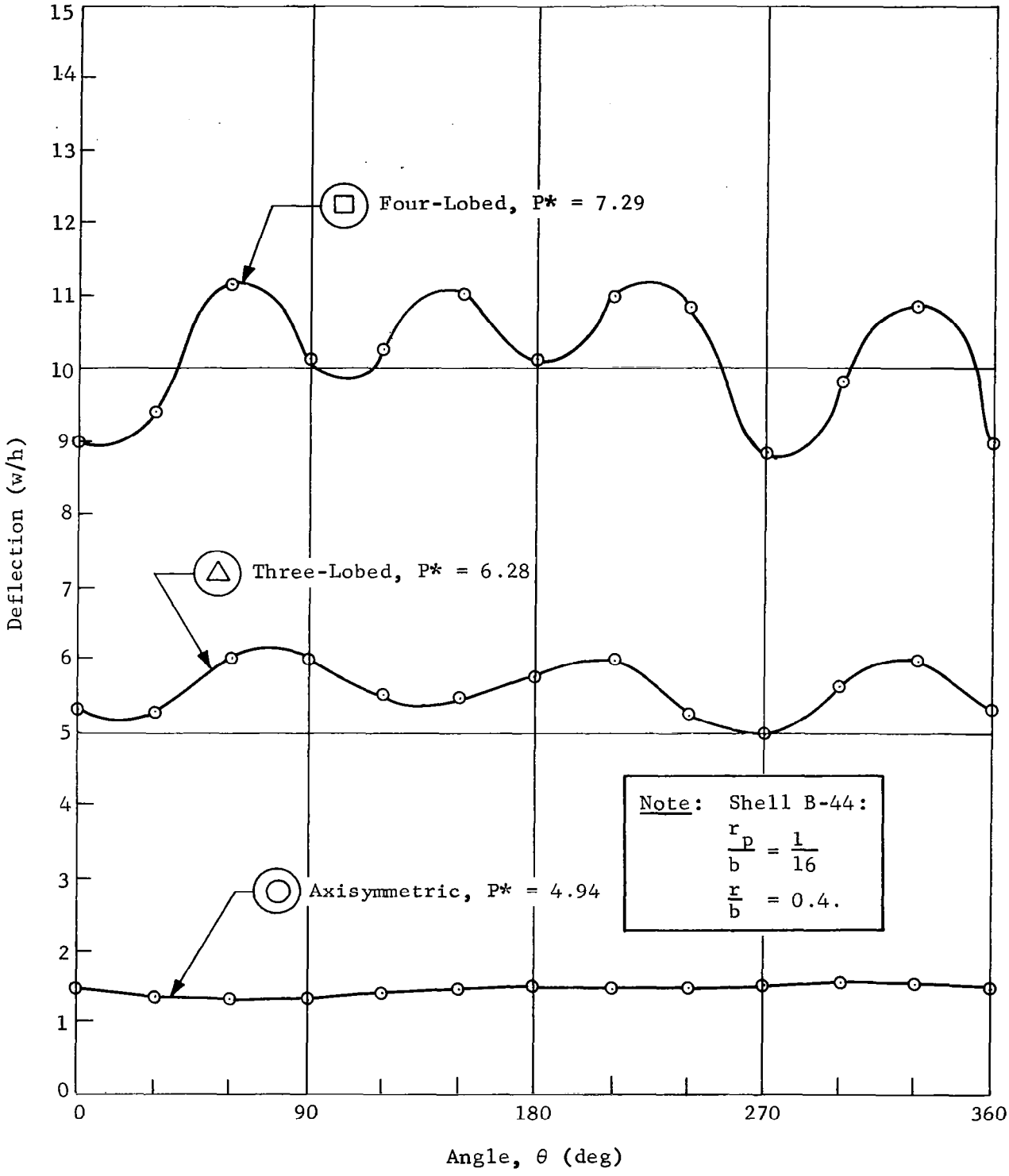


Fig. 29 Experimental Nonaxisymmetric Deflections, $\lambda = 12.3$, $a = 20.0$ in.

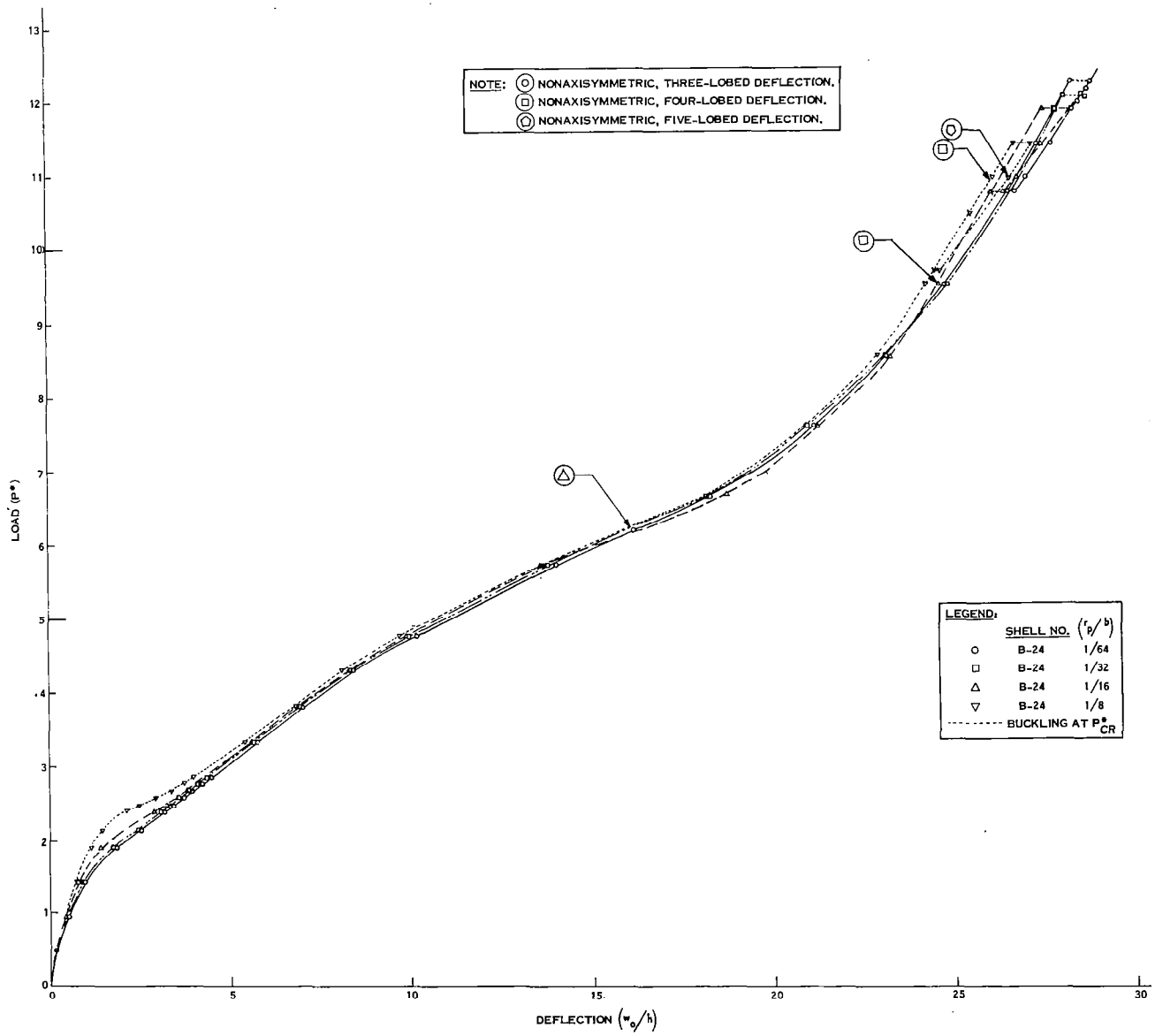


FIG. 30 EXPERIMENTAL LOAD-CENTER DEFLECTION, FOUR LOAD AREAS, $\lambda = 11.6$, $a = 31.0$ IN.

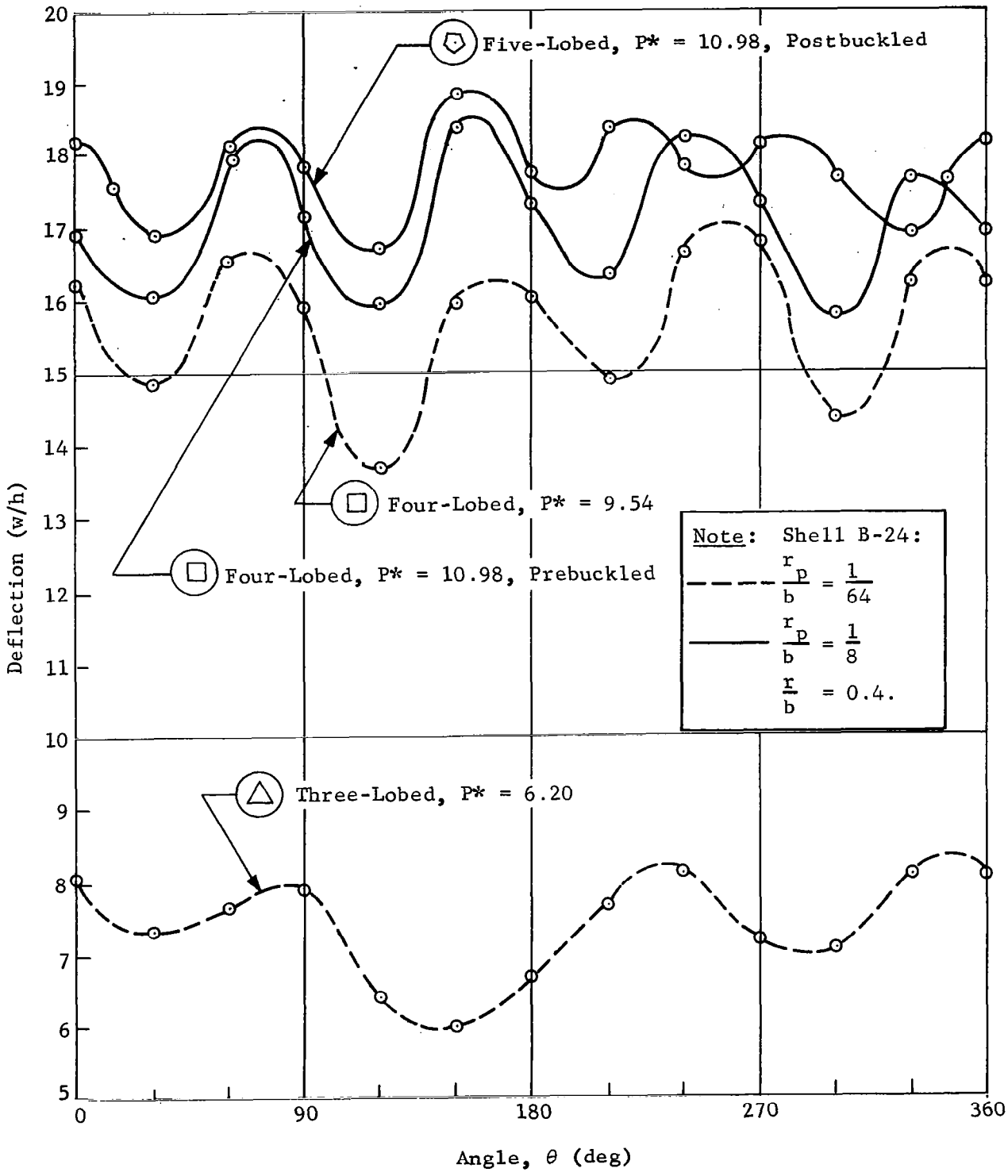


Fig. 31 Experimental Nonaxisymmetric Deflections, $\lambda = 11.6$, a = 31.0 in.

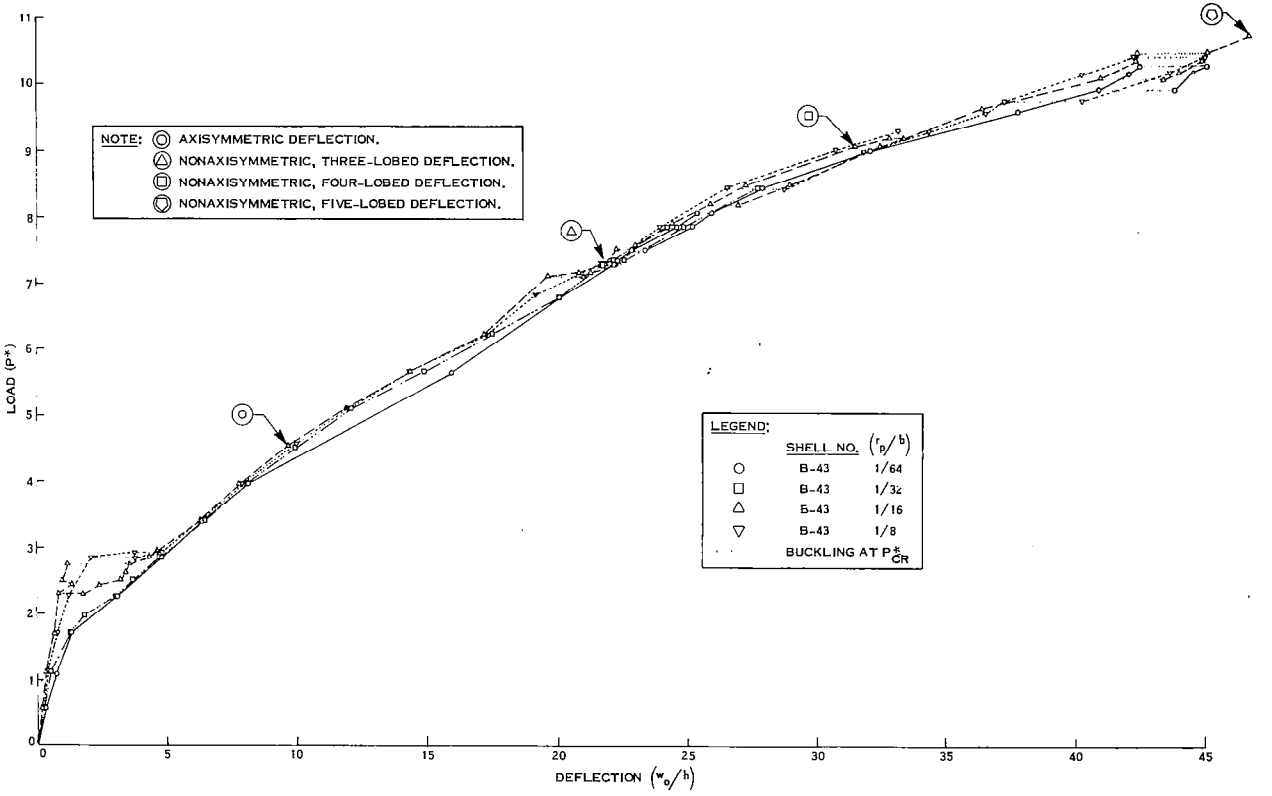


FIG. 32 EXPERIMENTAL LOAD-CENTER DEFLECTION, FOUR LOAD AREAS, λ = 16.1, e = 20.0 IN.

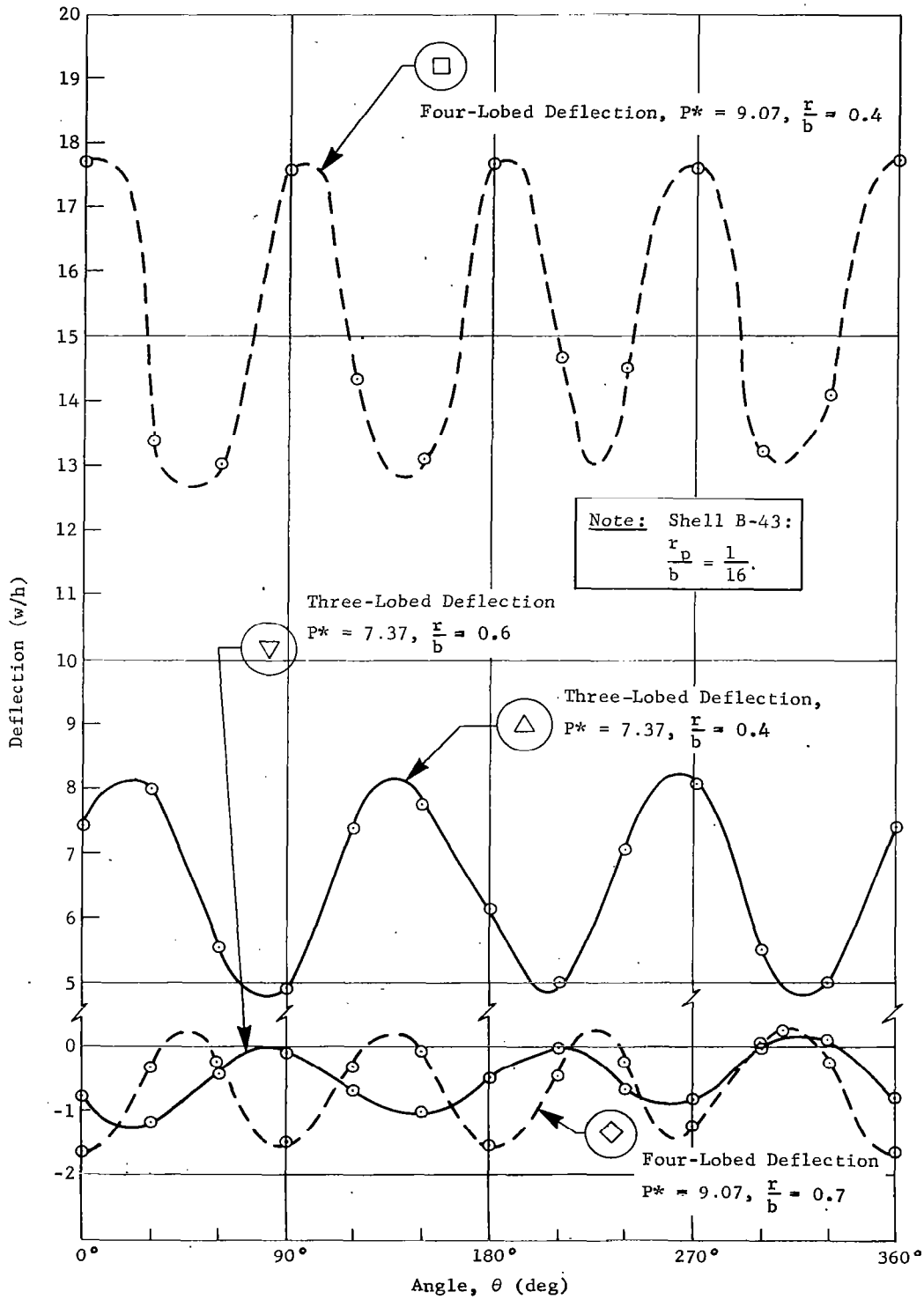


Fig. 33 Experimental Nonaxisymmetric Deflections, $\lambda = 16.1$, $a = 20.0$ in., Part 1

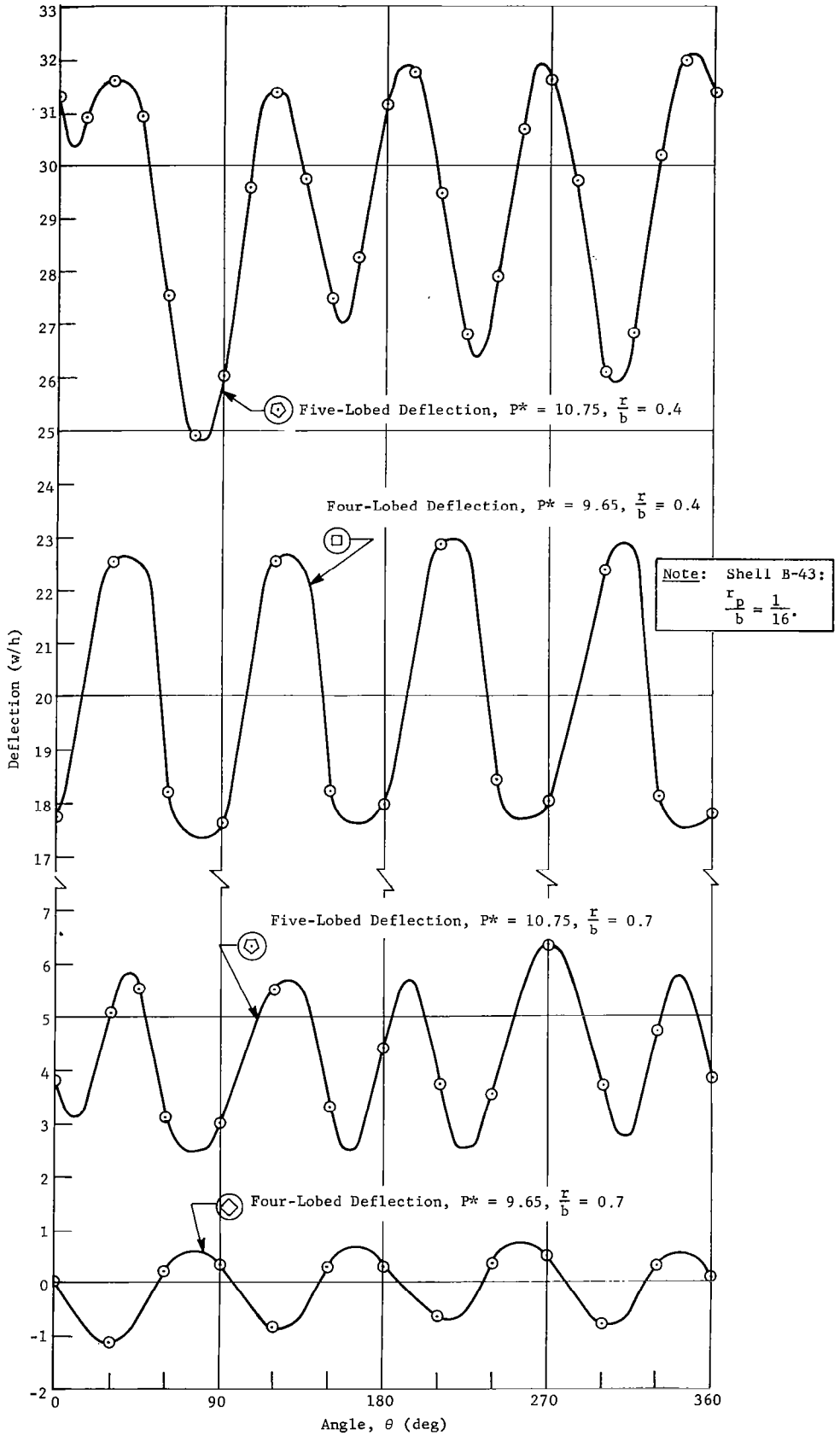


Fig. 34 Experimental Nonaxisymmetric Deflections, λ = 16.1, a = 20.0 in., Part 2

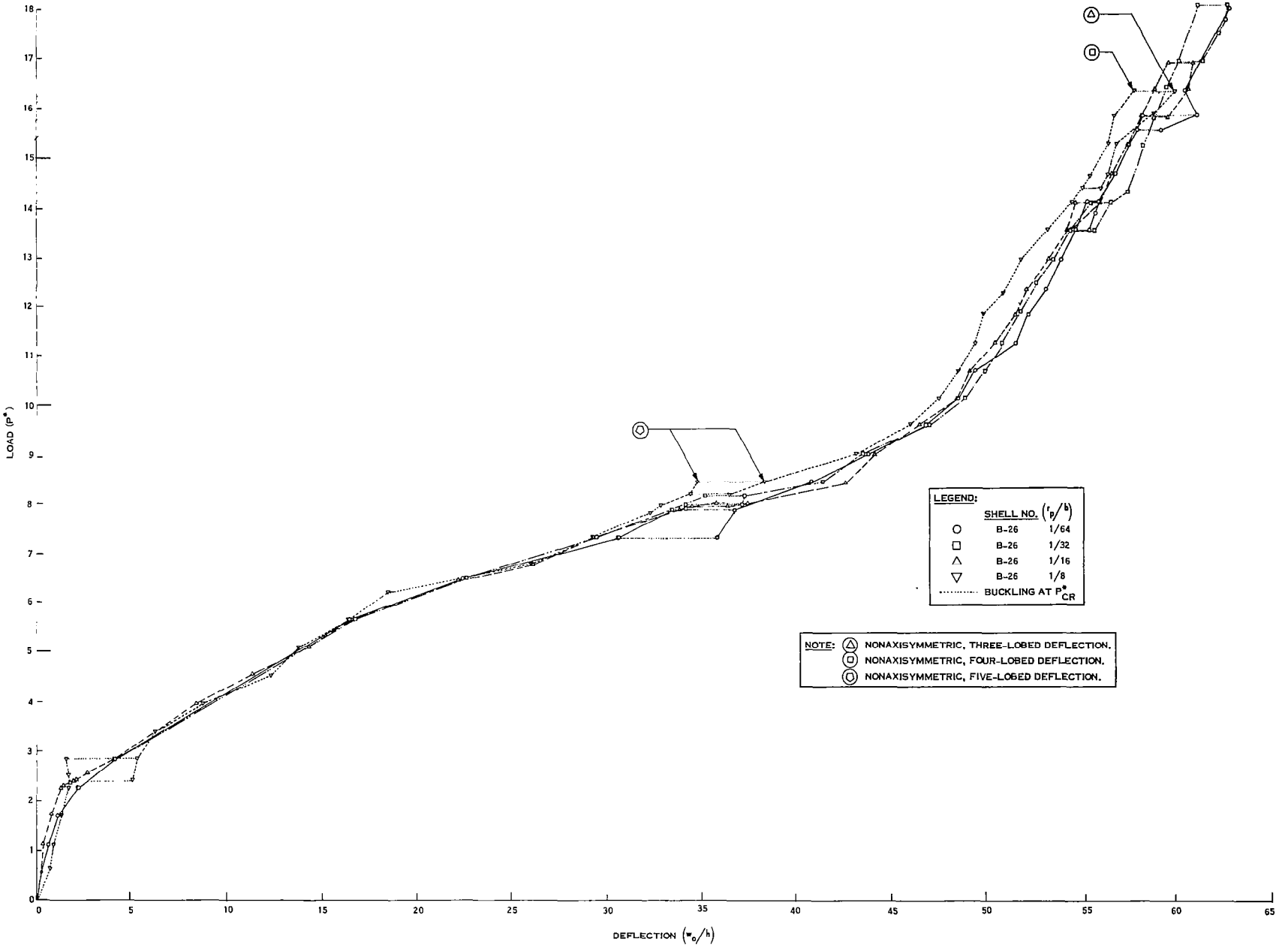


FIG. 35 EXPERIMENTAL LOAD-CENTER DEFLECTION, FOUR LOAD AREAS, λ = 15.6, a = 31.0 IN.

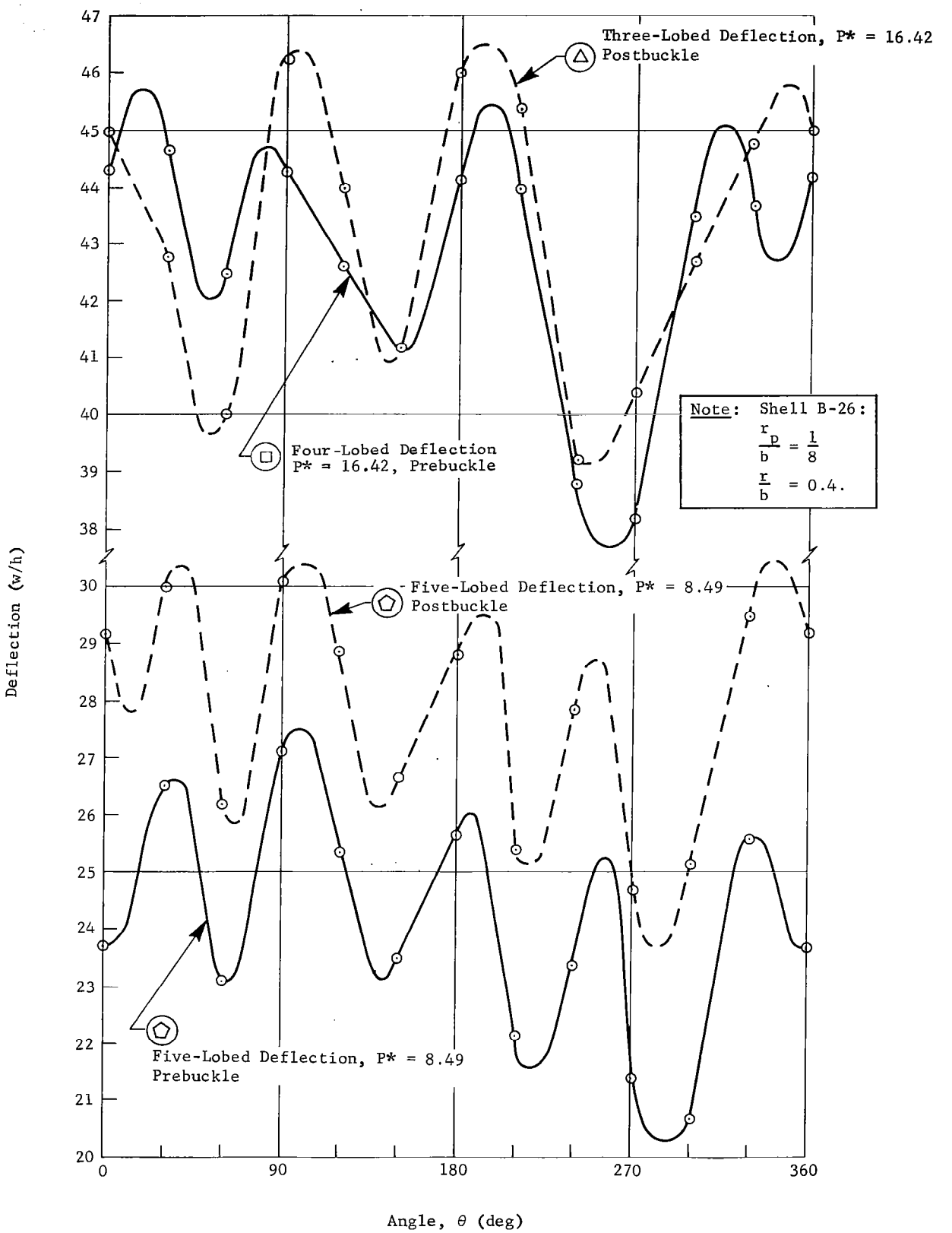


Fig. 36 Experimental Nonaxisymmetric Deflections, $\lambda = 15.6$, a = 31.0 in.

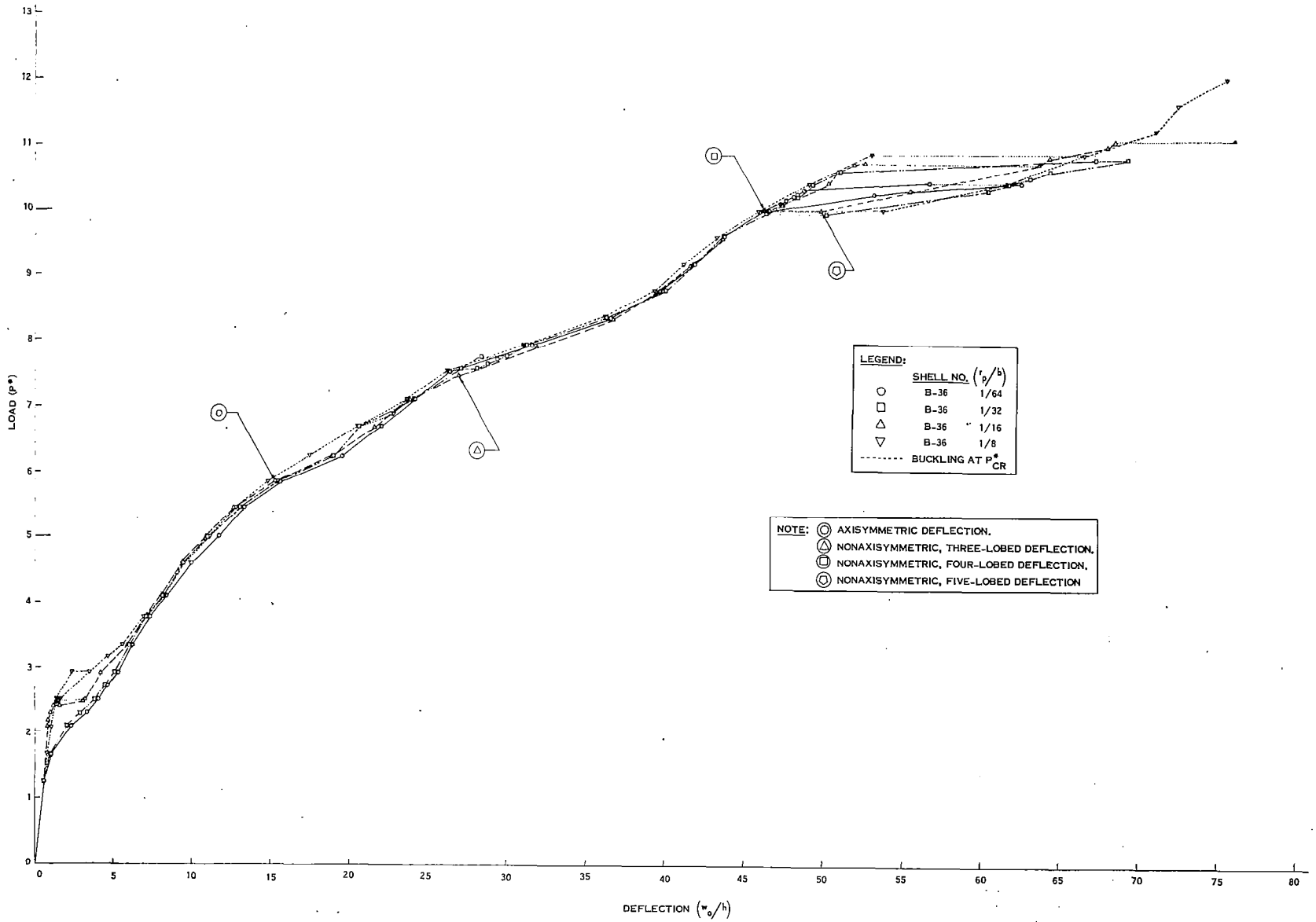


FIG. 37 EXPERIMENTAL LOAD-CENTER DEFLECTION, FOUR LOAD AREAS, $\lambda = 20.0$, $a = 20.0$ IN.

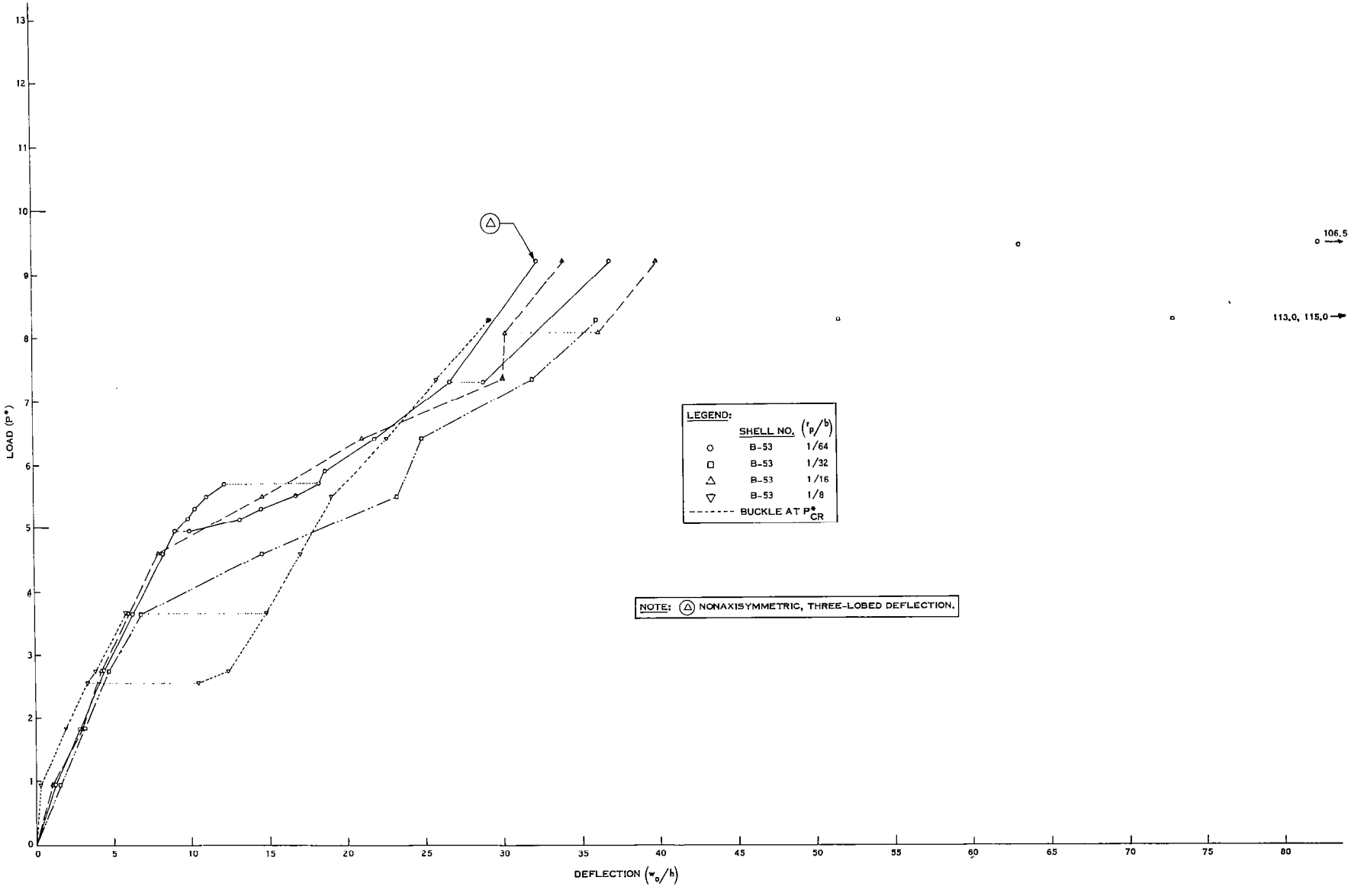


FIG. 38 EXPERIMENTAL LOAD-CENTER DEFLECTION, FOUR LOAD AREAS, $\lambda = 21.4$, $a = 31.0$ IN.

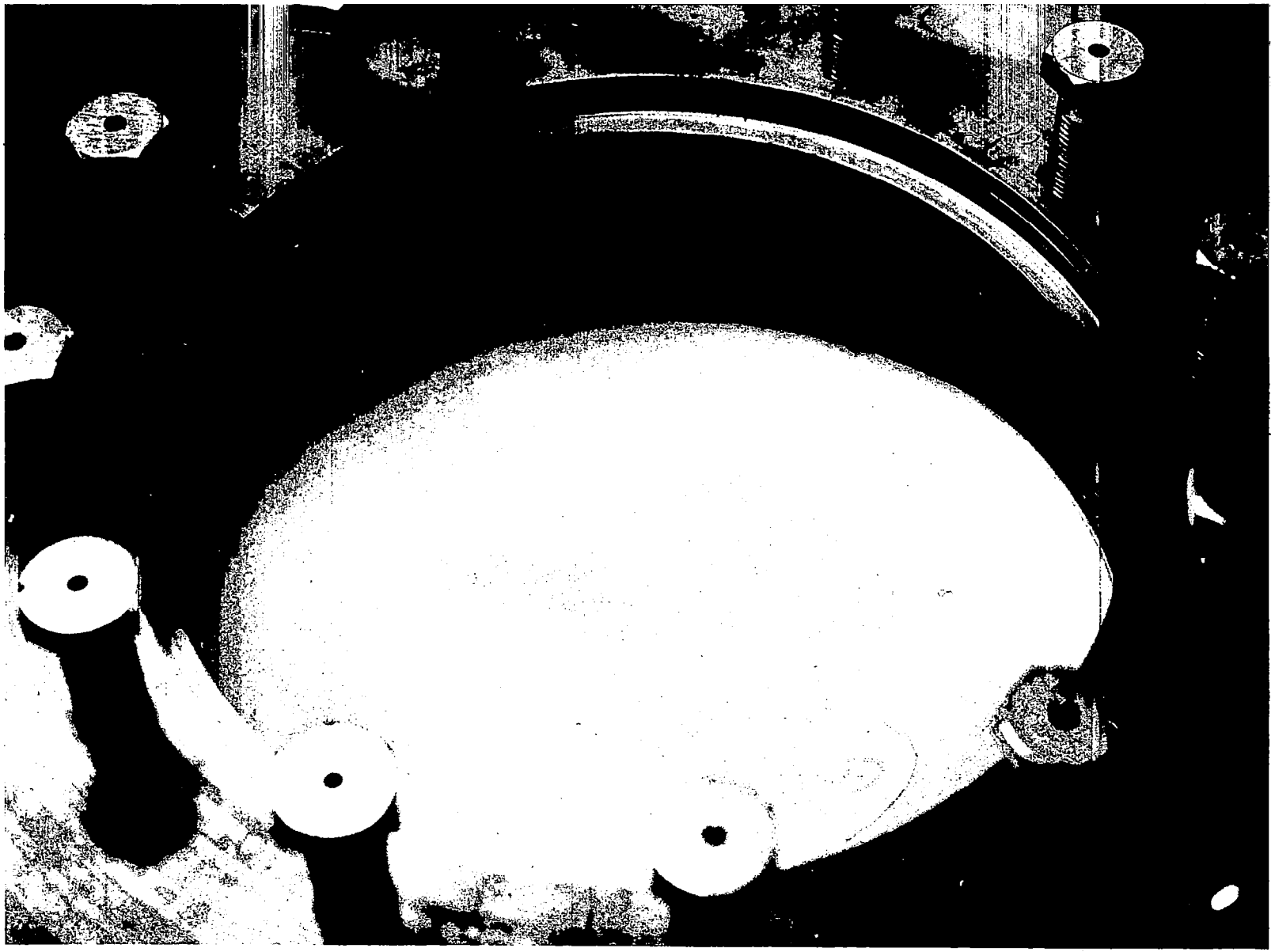


Fig. 39 Shell B-36 with Three-Lobed Deformation

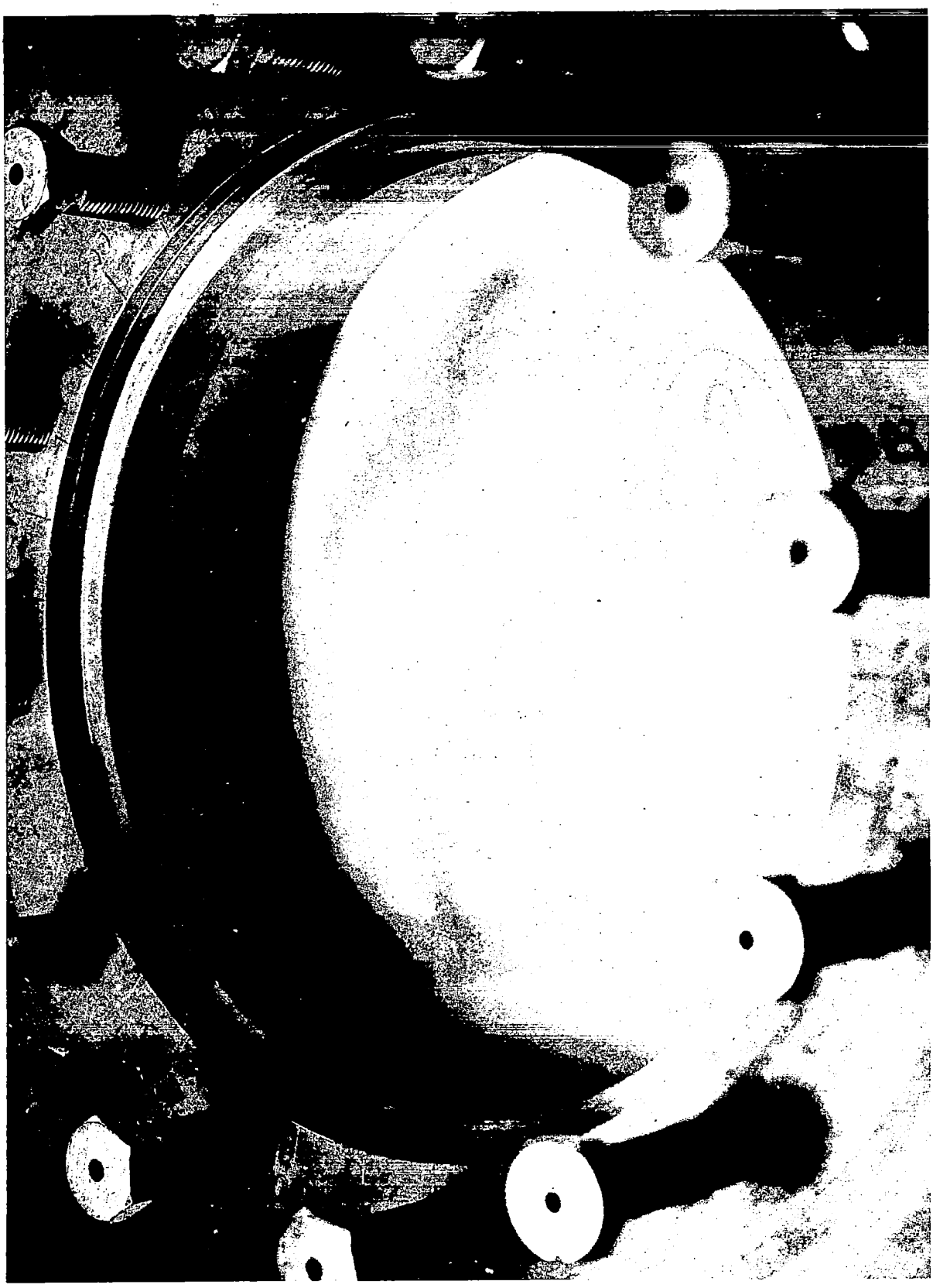


Fig. 40 Shell B-36 with Five-Lobed Deformation